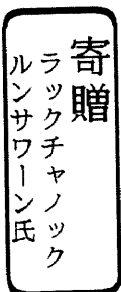


**Real-Time Imaging Using
Intense Half-Cycle Terahertz Pulses**

Rakchanok Rungsawang

Submitted to the Graduate School of
Pure and Applied Sciences
in Partial Fulfillment of the Requirements
for the Degree of Doctor of Philosophy in
Engineering

at the
University of Tsukuba



05009487

Contents

1	Introduction	1
1.1	Background	1
1.2	Motivation of this study	1
1.3	Outline of the thesis	2
2	Basics of Terahertz Pulses	3
2.1	Introduction	3
2.1.1	Terahertz pulse generation	3
2.2	Half-cycle terahertz pulses from a large-aperture photoconductive antenna	6
2.3	Propagation and focusing	8
2.4	Spatial distribution of focused THz beam	10
2.4.1	Imaging system	11
2.4.2	Experimentally observed the ring formation of focused THz beam	12
2.4.3	Numerical simulation of focused THz beam	13
2.5	Frequency dependence of diffraction	21
2.6	Time-domain terahertz spectroscopy	22
2.7	TPX lens performances	30
2.7.1	Aberration	30
2.7.2	Diffraction effects	30
2.8	Conclusions	31
3	Terahertz Electric Field Detection	34
3.1	Introduction	34
3.2	Electro-optic balance detection	37
3.2.1	Electro-optic crystal	37
3.2.2	Polarization state of probe pulses	40
3.3	Two-dimensional electric field detection	41
3.3.1	Electro-optic crystal	41
3.3.2	Polarization state of probe pulses	43
3.4	Conclusions	45
4	Electric Field Imaging	46
4.1	Introduction	46
4.2	Imaging system	46
4.3	Time-resolved images	47
4.4	Frequency-resolved images	52
4.5	Spatial resolution improvement	55

4.5.1	LT-GaAs antenna	55
4.5.2	High-pass filtering	58
4.6	Conclusions	68
5	Real-Time High-Speed Terahertz Imaging	69
5.1	Introduction	69
5.1.1	1-kHz imaging	69
5.1.2	Single-shot imaging	70
5.2	Imaging system	70
5.3	Snapshots of moving samples	71
5.4	Image enhancement	73
5.4.1	Normalization	73
5.4.2	Noises from a CCD camera	74
5.4.3	Filtering	75
5.5	Conclusions	81
6	Conclusions	82
A	Gaussian filtering	84

List of Figures

2.1	Typical THz waveform generated from a large-aperture photoconductive antenna	7
2.2	Fourier spectrum of the THz pulse in figure 2.1.	7
2.3	Schematic of optical setup for waveform measurement.	8
2.4	Experimentally obtained temporal waveform change due to propagation	9
2.5	Numerically obtained temporal waveform change due to propagation	10
2.6	Experimental setup for detecting two-dimensional intensity distribution	11
2.7	Intensity distribution of focused THz beam on the focal plane at various time delays	12
2.8	Temporal intensity profiles of the THz pulses reconstructed from the set of time-resolved images in figure 2.7	13
2.9	Experimentally obtained images of THz intensity distribution along the propagation direction at a fixed delay time	14
2.10	Temporal intensity profiles of the THz pulse at the focus obtained from the experiment and simulation	15
2.11	Time dependence of the spatial distribution of the THz intensity obtained by the simulations	16
2.12	Position dependence of the spatial distribution of the THz intensity obtained by the simulations	17
2.13	Propagation lines calculated using the Gaussian beam model	17
2.14	The second derivative of the THz intensity with respect to the radial parameter as a function of time	19
2.15	Normalized second derivative of the intensity of focused light pulses with respect to the radial parameter as a function of time	20
2.16	Schematic of knife-edge experiment for measuring the THz beam size in front of the emitter	21
2.17	Knife-edge position dependence of THz waveforms	22
2.18	Fourier amplitudes of the waveforms in figure 2.17	22
2.19	Beam diameter of some frequency components	23
2.20	THz pulses propagated through free space and TPX slabs of different thicknesses	24
2.21	Comparison of the reference and the sample waveforms	24
2.22	Fourier spectra of THz pulses in figure 2.20	25
2.23	Phase of THz pulses in figure 2.20; reference (solid line), l_1 (dotted line) and (l_2) dashed line.. . . .	25
2.24	Frequency dependence of absorption coefficients based on different calculation methods.	27
2.25	Finite-thickness slab	28
2.26	Absorption coefficient based on the slab theory	29
2.27	Symmetric-convex TPX lens (not to scale).	29
2.28	Propagation distance dependence of Airy disc at frequency 0.75 THz	32
2.29	Airy disc surrounded by rings of some frequencies at $z = 10$ mm	32
3.1	Orientation of the ZnTe crystal used for waveform detection.	37
3.2	Optical components of electro-optic balance detection	39

3.3	Orientation of the ZnTe crystal used for two-dimensional electric field detection.	41
3.4	Optical components of two-dimensional electric field detection	43
4.1	Schematic of experimental setup for two-dimensional electric field detection	47
4.2	Axial waveforms on the focal plane and on the image plane	48
4.3	Time-dependent electric field images presenting the shadow of the metal rod	49
4.4	Temporal waveforms extracted from the central pixels of images in figure 4.3	50
4.5	Images of the metal rod obtained by subtracting and dividing with the reference image	51
4.6	Fourier amplitude images and division images	52
4.7	Amplitude and phase images of aluminum slab	53
4.8	Fourier amplitude images of different sample shapes	54
4.9	Pump fluent-dependent waveforms of GaAs and LT-GaAs photoconductive emitters	56
4.10	Fourier amplitudes of the waveforms in figure. 4.9	56
4.11	Waveforms of GaAs and LT-GaAs photoconductive emitters of different bias voltages	57
4.12	Schematic of optical setup for the pump-probe experiment	57
4.13	Respond of photoexcited carriers on GaAs surface with optical pump and optical probe	58
4.14	Respond of photoexcited carriers on LT-GaAs surface with optical pump and optical probe	59
4.15	Responds of photoexcited carriers on GaAs and LT-GaAs surface at rising period in fine scale of figures 4.13 and 4.14	59
4.16	Schematic of hexagonally close packed filter	60
4.17	Circular hole arrays for filtering low-frequency components	62
4.18	Temporal waveforms and their Fourier amplitudes of the reference pulse and the filtered pulse by the grill filter and by the speaker filter at the focal point	63
4.19	Temporal waveforms and their Fourier amplitudes of the reference pulse and the filtered pulse by the grill filter and by the speaker filter at the center of the image plane	63
4.20	Power transmittance of the grill filter and the speaker filter	64
4.21	Spectral images of the reference THz beam	65
4.22	Spectral images of the THz beam passed through the grill filter	66
4.23	Time-dependent reference images and sample images.	67
4.24	Time-dependent images of the filtered THz beam and that of the sample using the filtered THz field	67
4.25	Spectral images at 288 GHz of the reference THz beam, the metal rod, the filtered THz beam, and the metal rod using filtered THz field	68
5.1	Schematic of the experimental setup for single-shot imaging	70
5.2	Time chart of the imaging operation in the CCD camera	71
5.3	Normalized THz waveforms at the focus and image plane	72
5.4	Digital processed images	73
5.5	Snap shots of the movie showing the translation of the metal rod	74
5.6	Single-shot field image and division image of the metal rod	74
5.7	Intensity of a single probe pulse	75
5.8	Noisy images	76
5.9	Images of the metal rod operated by various filters	76
5.10	Division image with zero padding	78
5.11	The default organization of the quadrants from FFT	79
5.12	Fourier transformed image of figure 5.10	79

5.13 Reorganized quadrants of the Fourier transformed image of figure 5.12(b)	80
5.14 Magnitude of Gaussian filter	80
5.15 Re-transformed image and filtered image	80

Chapter 1

Introduction

1.1 Background

The terahertz (THz) region is defined as the frequency between 0.1 THz to 10 THz, namely wavelength of 30 μm -3 mm. It occupies a large portion of the electromagnetic spectrum between the infrared and microwave bands. The THz waves can be considered as far-infrared radiation and treated in quasi-optic system because of their long wavelengths. The waves in this region have low photon energies (for example, about 4 meV at 1THz) and therefore do not subject a biological tissue to harmful radiation. Furthermore, the THz region forms an interesting region of the spectrum as molecular resonances are in this band. However, the THz radiation is highly absorbed by water. This limits the sensing and imaging in water-rich samples for most biomedical applications. Namely, this strong absorption prohibits wave transmission through a thick tissue.

Recent advances in the generation, detection, and manipulation of electromagnetic waves in the THz region are rapidly increasing. The major applications revolve around two factors. The first factor is spectral specificity. Many materials have distinct absorptive property or fingerprint in this spectral range so that THz waves can reveal interesting features. This fact is relevant to an application in spectroscopy, particularly time-domain spectroscopy. The THz waves can determine various properties of materials, such as semiconductors, dielectrics, proteins, and liquids, in low-frequency range [1-3]. The second factor is transmission properties. Because of their long wavelengths, THz waves are transparent through non-metallic materials such as paper, wood, ceramic, semiconductor, etc. This allows the possibility of inspecting an object through these materials. According to this factor, THz radiation is interesting for applying to imaging. In addition, the use of THz waves is much safer than that of X-ray. Consequently, THz waves have been used for non-invasive monitoring of biological tissues [4]. Furthermore, the combination of two factors allows an application known as two-dimensional time-domain spectroscopy. For instance, it would be possible to image the distribution of specific proteins or water in tissue. The technique could also be used to seek out structural defects in materials or to detect skin cancer.

1.2 Motivation of this study

Terahertz research has become one of most promising research areas for advances in imaging since 1995. However, THz wave imaging is still at an undeveloped stage because of limitations in generating, propagating and detecting the waves. In the same way that visible light can create a photograph and X-ray can view within envelopes, THz waves can create images and transmit information that is generally absent using another optical waves or X-ray waves.

Conventional terahertz imaging systems rely on scanning the sample in two dimensions to reconstruct a

whole image. Even though it provides clear images, one drawback of the scanning method is the requirement to scan the target. This results in prohibitive acquisition times. Wu *et al.* first proposed the two-dimensional imaging method by applying an electro-optic sampling technique to a charge-coupled device (CCD) camera so that the spatial distribution of the THz radiation can be detected in real time [5]. The significant difference between the scanning mode and the two-dimensional imaging mode is the size of the THz beam on a sample of interest. In the scanning mode, the THz wave has to be focused on small area of the sample. Smaller spot size is used and a higher spatial resolution is obtained. On the other hand, the beam size illuminating on the sample in the second mode is collimated. The larger beam size you use, the larger sample you can observe. This means that the power of THz radiation is a critical parameter for the two-dimensional imaging, particularly in a transmission mode. In addition, as the THz field intensity increases, a thicker sample or a higher density of moisture can be penetrated.

High power coherent THz radiation is available from several sources such as biased photoconductive antennas [6, 7], phase-matched difference frequency mixing in a GaSe crystal [8], and relativistic electrons [9]. Out of sources, a biased photoconductive antenna is the most compact source. It gives a half-cycle to nearly monocycle electric field pulse that has been used in time-domain spectroscopies and studies of Rydberg atom ionization [10]. The half-cycle THz pulse would have a well-defined field distribution in the spatial and time domains. This might be an advantage for the real-time imaging. Therefore, tremendous potential in using intense half-cycle THz electromagnetic pulses from a large-aperture biased photoconductive antenna to image objects should be studied.

1.3 Outline of the thesis

Spatial and temporal distributions of the focused half-cycle terahertz pulse were studied. Their unique characteristics were explained using the Gaussian beam theory. Measurement of two-dimensional electric field based on an electro-optic sampling technique was introduced. It permits the extraction of information on the phase of the field and opens up new possibilities for characterizing spatial dependent material composition. THz field images of an object were taken and analyzed the time dependence of image quality. With the results, it allows to develop a high-speed imaging for real-time detection in the THz region. Also, single-shot imaging was performed. This could enable monitoring single-time high-speed events occurring in the order of sub-picosecond.

This thesis is organized as follows. Chapter 2 provides basic information on THz electromagnetic pulses. The various generation methods of the pulse will be reviewed. Then it focuses on a broadband THz pulse generated by a large-aperture photoconductive antenna, which produces a half-cycle electric pulse under a number of different conditions. Chapter 2 also covers the numerical simulations of the generating and propagating of the THz pulse. THz Time-domain spectroscopy is described. It was used to observe the frequency-dependent absorption of a typical focusing material for THz radiation called TPX (polymethylpentene; Mitsui Chemicals, Inc.). The performance of a symmetric-convex TPX lens is demonstrated. Chapter 3 explains how to detect THz electric field in one dimension (at the center of a focused THz beam) and two dimensions (entire beam) based on electro-optic sampling detection. Chapter 4 shows the imaging of an object using the THz field and analyzing the results in time and frequency domains. It also introduces how to improve the spatial resolution of the THz image. Chapter 5 describes the high-speed imaging system, and how to improve image quality obtained from the system. Chapter 6 concludes the thesis and discusses the perspective to future researches and applications of the imaging which uses the THz radiation from a large-aperture photoconductive emitter.

Appendix contains the computer program based on C for digital image processing, particularly spatial Fourier transformation and Gaussian filtering.

Chapter 2

Basics of Terahertz Pulses

This chapter introduces various generation methods of THz pulses, namely, photoconductive switching, optical rectification and relativistic electron in section 2.1.1. Among them, the photoconductive switching method was chosen to produce strong THz electric field that is one of the requirements for high-speed THz imaging. Characteristics of the THz pulse radiated from a large-aperture biased photoconductive antenna at the center and on the plane that is normal to the propagation axis are described in sections 2.3 and 2.4, respectively. Section 2.5 explains how to measure frequency-dependent beam size of THz waves in front of the THz emitter. Section 2.6 illustrates THz time-domain spectroscopy experiment and the analysis. The object of the interest is a TPX (Terahertz transparent copolymer Polymethylpentene with low index of refraction) substrate. The experiment was done before designing a TPX lens to obtain the absorption coefficient. The last section presents the performance of the symmetric-convex TPX lens used in most of experiments.

2.1 Introduction

2.1.1 Terahertz pulse generation

THz radiation can be classified into narrowband and broadband types. Narrowband THz waves or continuous waves are usually generated from free-electron lasers [11], fast-diodes [12], and parametric sources [13]. The parametric generator is a wavelength tunable source. This section reviews the generation mechanism of the second type of THz radiation. One application of a femtosecond laser is to generate THz electromagnetic pulses. An ultrashort pulse is used in generating a fast polarization transient on a surface of semiconductor wafer or in a nonlinear medium. To date, there are various techniques available for the generating a THz pulse. Their main mechanisms will be explained and their characteristics will be compared in terms of an imaging application.

Several techniques for the terahertz pulse generation have been developed since solid state lasers were invented. These can be divided into 2 main mechanisms, i.e., photoconductive switching and optical rectification. In short, the photoconductive approach employs high-speed photoconductors as transient current sources to radiate the waves after excitation with ultra-short laser pulses while the rectification approach uses electro-optic crystals as rectification media and the inverse process of the electro-optic (EO) effect in generating the waves. In general, photoconductive antennas provide a higher terahertz field than that used for optical rectification. This owes to the fact that optical pulses (pump pulses) are used for triggering the switch to release the energy that is pre-stored in the antenna structure as dc coupled electrostatic energy. Theoretically, the total power of terahertz wave can be higher than the pumping pulse energy. In contrast, the optical rectification process converts part of incident optical energy into terahertz radiation.

Photoconductive switching

The generation of a THz pulse through photoconductive switching consists of an ultrashort light pulse, a photoconductive media and DC-bias voltage. When the device is switched from “off” to “on” state by the rising period of light pulse, a transient current at its surface is produced. Photocarriers are then accelerated by the bias voltage. This emits THz radiation from both sides of the media wafer. The temporal shape of the surface field is a step-like function, by which the steepness of the step is determined by the rise time of the optical excitation and the rise time of the mobility in the device [14]. The shorter the optical pulse is, the faster the creation of electron-hole pair will be. The steepness of the surface field determines the THz pulse width in the far field. Because the carrier lifetime of a standard semiconductor is typically much longer than the time scale of interest, only the rising period of time-dependent mobility affects on the emitted temporal waveform. In the case of a point source or dipole antenna, of size of the order of a micron or much smaller than the generated wavelength, the far field is proportional to the second time-derivative of the surface field. It, therefore, provides a single THz pulse. In the case of a large source, of size much larger than the center wavelength of emitted THz radiation, all the point sources of the emitter interfere so that the field is proportional to the first time-derivative of the surface field. The temporal shape at far field is now a half-cycle electric pulse [15]. THz electric field is generated in a high-resistance semiconductor by applying a dc voltage or a magnetic field. These generation mechanisms are described as follows.

1. Biased photoconductive antenna

An ultrafast laser pulse illuminates the semiconductor between the electrodes, creating a large density of mobile charge carriers. All accelerated charges emit electromagnetic radiation. These charge carriers, reaching their maximum velocity in less than picosecond emit a single electric pulse shorter than picosecond that contains a broad range of frequencies, up to a few THz. We can illuminate the optical pulses on the gap side or the other side to produce photo carriers. If the wafer is thin enough, for instance 500 μm , there is no significant difference in peak power and waveform when generating photocarriers at different sides. The mechanism of subpicosecond electromagnetic pulse generation by a semiconductor and femtosecond laser pulses was first demonstrated by Auston [16]. This method was considerably improved and led the generation of the pulse with frequencies extending up to a few terahertz [17]. There are two kinds of photoconductive emitter depending on the gap size, i.e., a large-aperture antenna [18] and a dipole antenna [19]. A number of semiconductor substrates were used for the photoconductive antenna, such as GaAs, low-temperature-grown GaAs, and InP. Theoretically, the magnitude of the field is proportional to the magnitude of bias field. The time-dependent electric field at the surface of emitter (near field) was calculated using Maxwell’s equations and Ohm’s law [6, 20]. From the boundary condition, the surface field of the THz radiation is given by

$$E_{\text{surf}}(t) = -E_{\text{bias}} \frac{\sigma_s(t)\eta_0}{\sigma_s(t)\eta_0 + (1 + \sqrt{\epsilon_r})}, \quad (2.1)$$

where E_{bias} is the applied electric field, η_0 is the free space impedance, ϵ_r is the relative dielectric constant of the semiconductor, and $\sigma_s(t)$ is the time-dependent surface photoconductivity. This equation shows that if the antenna is irradiated with sufficiently high fluent optical light, i.e., $\sigma_s(t)\eta_0 \sim 1$, the radiation would be saturated at $E_{\text{surf}}(t) = -E_{\text{bias}}/(1 + \sqrt{\epsilon_r})$. In other words, the value of E_{surf} shows salutation for a large value of σ_s on account of cancellation of the local bias field by the surface field as shown in the relation

$$J_s(t) = \sigma_s(t)[E_{\text{bias}} + E_{\text{surf}}(t)], \quad (2.2)$$

where $J_s(t)$ is the surface current density of the photoconductive emitter. According to theory, if high power THz radiation is required, we should use low fluent pulses against saturation process and bias with high voltage [21].

Another way to enhance the power is by using LT-GaAs layer grown on a SI-GaAs as a photoconductive emitter with multiple-pulse excitation [6].

2. Photoconductive antenna in a magnetic field

Without applying bias voltage, an ultrashort optical pulse can generate THz radiation from accelerated carriers driven by the surface depletion field [22, 23] and optical rectification [24]. Zhang *et al.* reported THz optical rectification radiation emitted in the forward direction from a (111) GaAs with normal incident [25, 26]. This method gives low THz power but it can be enhanced by applying an external magnetic field to the semiconductor wafer so that the magnetic field is perpendicular to the static electric field which point into the surface of the wafer [27]. THz radiation develops in the forward direction due to the Lorentz force, instead of bias electric force as previous mechanism, on the moving photocarriers. Besides driving the optically induced carriers, a magnetic field can change the polarization of emitted THz radiation. A non-doped InAs wafer is used as a photoconductor to radiate THz field in reflective configuration among a magnetic field. This provides a high average-power THz radiation and controllable elliptical polarization [28]. However, Zhang *et al.* reported the saturation at high magnetic field around 3 T [29].

3. Diamond photoconductive switch array

As shown in eq.(2.1), the power of THz radiation is proportional to the bias electric field. However, we cannot increase the bias voltage over the breakdown strength of the semiconductor media. In our experiment, the maximum bias voltage applied to 30 mm gap is about 20 kV with very low optical excitation. A photoconductive switch-arrayed antenna with a chemical vapor-deposited diamond film overcomes this obstacle [7]. It is because of the high breakdown threshold of diamond and the overcoated gap structure for prevention of surface flashover. The carriers on the diamond surface were excited with ultrashort Kr*F laser light ($\lambda = 248$ nm) and biased with field up to 2×10^3 kV/cm. This gave the maximum electric field of 10^3 kV/cm, 10 times larger than that generated from the large-aperture biased photoconductive antenna in our experiment.

Optical rectification and phase-matched difference frequency mixing

The generation of THz radiation through optical rectification is possible because of the noncentrosymmetric nature of the medium. The process involves illuminating the medium with ultrashort laser pulses, causing a time-dependent polarization to be created in the material. This induced polarization is proportional to the intensity of the excitation pulse, and results in the radiation of electromagnetic wave of terahertz bandwidth. The induced polarization $P^{(2)}(t)$ can be expressed in term of optical pump intensity $I(t)$ as [15]

$$P^{(2)}(t) = \frac{\chi^{(2)}I(t)}{2}. \quad (2.3)$$

Here $\chi^{(2)}$ is second order non-linear susceptibility. The equation shows that the efficiency of this technique depends on the material used and the intensity of the incident optical pulse. A variety of materials used in this method have been demonstrated such as LiTaO₃, LiNbO₃, ZnTe, GaAs, GaSe and DAST(organic salt 4-*N*, *N*-4-dimethylamino -4'-*N*'-methylstilbazolium tosylate) [25, 26, 30–32]. The bandwidth of the radiation is inversely proportional to the pulse width of the incident radiation.

The spectrum and the pulse duration from non-phase matched optical rectification were not fully characterized and the low power prevented widespread application. Broadband ultrashort pulses are used for difference-frequency mixing in a GaSe crystal in which different components of the input spectrum contribute to the phase-matched parametric process. The average power is about 100 times greater than that obtained for non-phase-matched optical rectification with the same material [33]. Using the phase-matched method,

Reimann *et al.* reported the regeneration of a few cycle THz pulse with amplitude of megavolt per centimeter [8]. It covers a broadband of frequencies up to 35 THz. The number of cycle varies as the thickness of the GaSe crystal and the central wavelength can be selected from the angle of the crystal.

Relativistic electron

Recent method to produce broadband THz radiation with a high peak and an average power is relativistic electron. The average power is nearly 20 W, several orders of magnitude higher than the previous sources, i.e., on order of μW . The method produces coherent THz radiation by accelerated electrons is described as follows. The process begins with the ultrashort pulsed laser excitation in GaAs, as in photoconductive switching to produce bunches of free electron in space, instead of photocarriers on the surface of the semiconductor. Using the electron-recovered linac, very short electron bunches (~ 500 fs) are brought to relative energies (40 MeV) in linac [9]. They are then transversely accelerated by a magnetic field to produce the THz radiation. The bunch length determines the spectral range over which the coherent enhancement occurs. The literature reports the spectral content extends up to about 1 THz for the 500-fs width electron bunch.

When coherent THz wave signals are detected in time domain, they can map information in amplitude and phase of an object in question. This gives access to absorption and dispersion spectroscopy. We can select THz source to match with the spectrum of interest. For instance, if we want to study something in low frequency mode, the THz radiation from photoconductive switching source is appropriate. In the case of high frequency, the THz waves from rectification are requested. The spectrum of the photoconductive antenna is limited to a few THz while that from the rectification extends up to 50 THz. The THz waves radiation relative electrons are appropriate for studying the nonlinear properties of a matter because of their extreme power. Another mode of imaging using THz radiation is for inspection work. THz waves can penetrate and image inside most dielectric materials, which may be opaque to visible light and low contrast to X-rays. In addition, THz imaging, due to their low energy, can provide a less damaging inspection. To apply the later mode for real-world application, two-dimensional detection is necessary for a fast detection. Therefore high-peak power and large THz beam size are required. The dipole antenna gives a low-power electric field because the efficiency from the optical rectification relies on existing nonlinear coefficients. However, the central wavelength is typically shorter than that obtained by the photoconductive switching. It, therefore, allows a better spatial resolution of THz images. The THz pulse from phase-matched difference-frequency mixing is a new tool for imaging because of its high electric strength. Conventionally, a large-aperture antenna is used to achieve imaging of an object in two-dimensional mode [34].

2.2 Half-cycle terahertz pulses from a large-aperture photoconductive antenna

In this research, a photoconductive switching antenna was used to produce the required THz power for imaging. A large-aperture photoconductive antenna, a semiconductor attached with electrodes with the gap width larger than the emitting wavelength gives a large THz beam and high field strength depending on bias voltage. A GaAs wafer was used as the photoconductor. It emits approximately half-cycle THz pulse at the far field as shown in figure 2.1. This section describes the characteristics of the half-cycle pulse on the propagation axis and two-dimensional profile of the focused THz beam. A good understanding of the characteristics of the THz pulse leads to the implementation of the real-time imaging system.

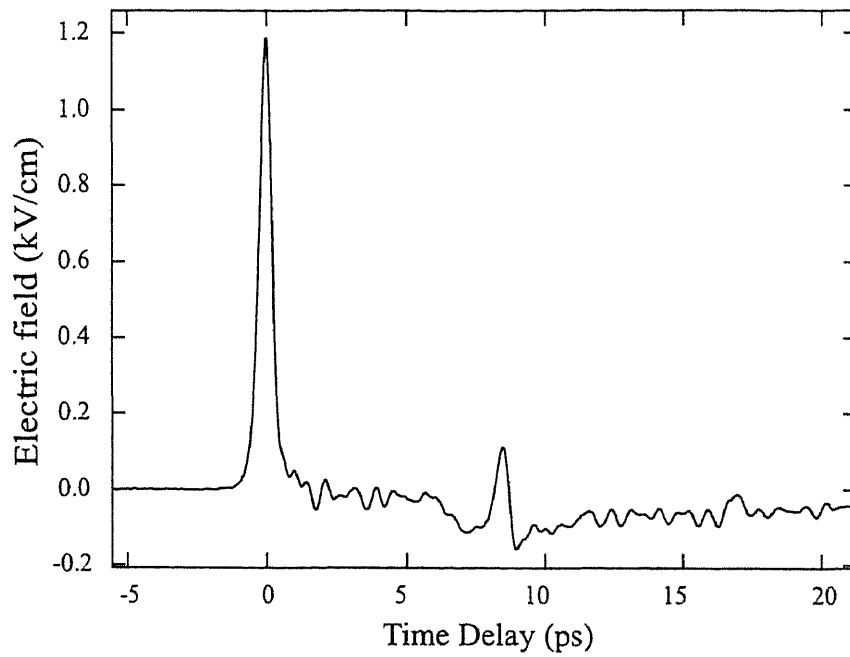


Figure 2.1: Typical THz waveform generated from a large-aperture photoconductive antenna.

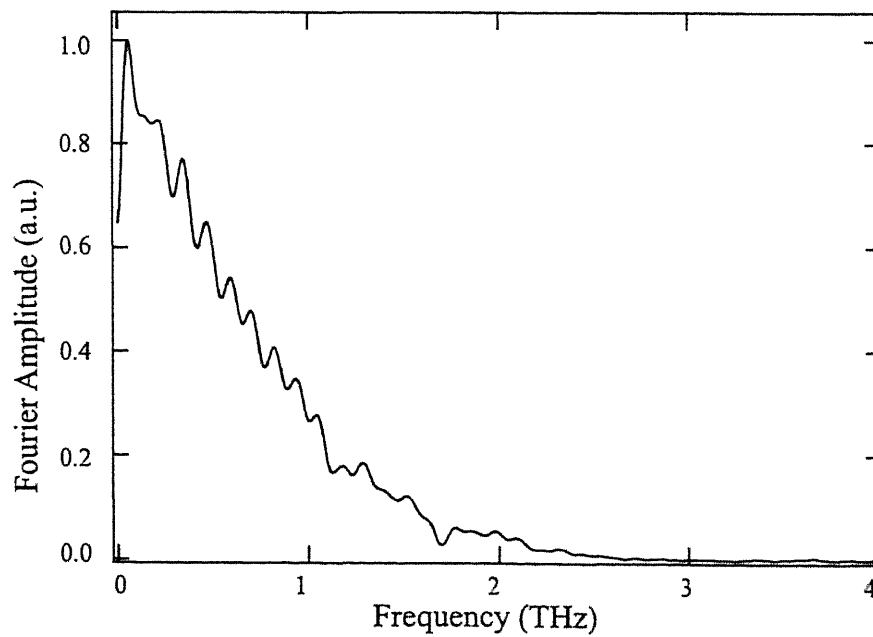


Figure 2.2: Fourier spectrum of the THz pulse in figure 2.1.

2.3 Propagation and focusing

THz pulses generated using ultrashort optical pulses have a spectrum extending from dc to a few THz as can be seen in figure 2.2. The wavelength of a significant spectral portion is long compared to the source and other optical elements. For these reasons, the temporal waveform of THz pulse is dependent on the position, and changes significantly via propagation and focusing processes. Since almost applications of THz pulses use a focusing optic to collimate or collect the beam, understanding of propagation characteristics of the pulse is important. In this section, we illustrate the studies of THz pulse propagation around the focus. Theoretical approach based on Gaussian beam theory was used to explain the spatial profile of each frequency component and reproduce the experimental results.

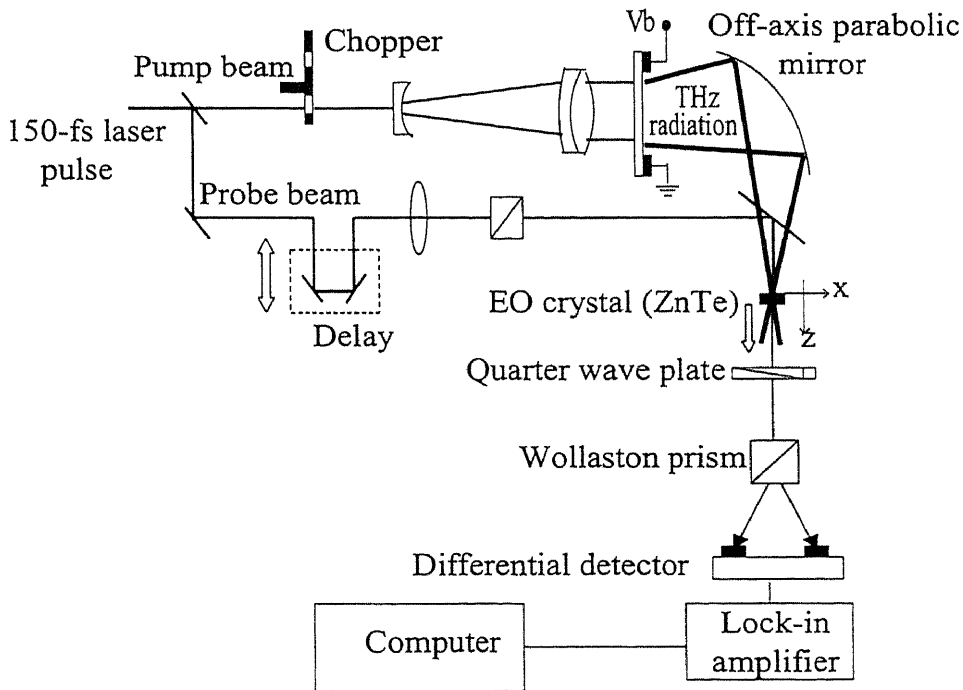


Figure 2.3: Schematic of optical setup for waveform measurement.

Figure 2.3 shows the optical setup. A femtosecond laser beam was split into pump and probe beams at a wedge beam splitter. The pump beam was the main portion. It was brought to a filter, an optical chopper, an expander, and then illuminated at a photoconductive antenna. The spatial distribution of the pump beam on the emitter was measured using a knife-edge experiment, and it was found to be nearly Gaussian which the $1/e$ radius was 9.2 mm. The pump fluence is calculated to be $3.6 \mu\text{J}/\text{cm}^2$. The emitted THz radiation was focused by an off-axis parabolic gold mirror which has a focal length of 152.4 mm. The detecting crystal (ZnTe) was placed at the optical axis. It was translated along the axis for observing the THz waveform at different propagation distance. The other beam that was reflected from the beam splitter was guided to an optical delay line, a linear polarizer, and reflected at a pellicle beam splitter to be collinear with the THz beam. The emitter of THz radiation was a non-doped semi-insulating GaAs wafer with a $\langle 110 \rangle$ surface. The diameter and thickness of the wafer were 50 mm and $350 \mu\text{m}$, respectively. The electrodes were attached to the wafer with a gap width of 30 mm. A pulsed electric voltage of 12 kV was applied to the electrodes. The EO crystal

was translated along the axis for observing the THz waveform at different propagation distances. The THz field was measured every 5 mm from the focal point of the parabolic mirror ($z = 0$).

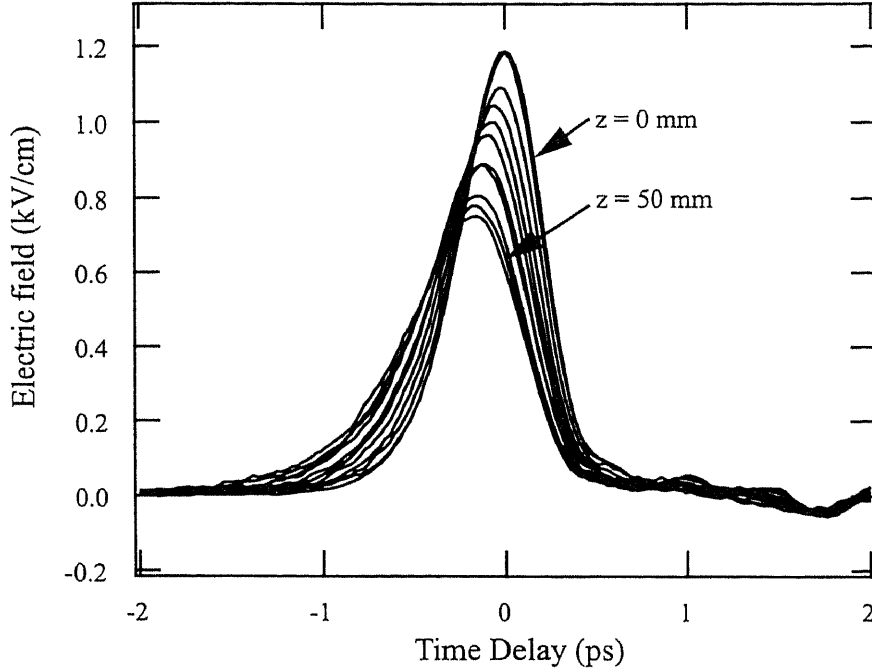


Figure 2.4: Experimentally obtained temporal waveforms of THz pulses at position $z=0$ (the focal point) to $z=50$ mm in steps of 5 mm.

The change of temporal waveforms was depicted in figure 2.4. Apparently, by increasing z , the peak was lowered, the pulse was broadened, and the peak position was shifted in the negative direction. The broadening and decreasing of the peak field can be understood using Gaussian beam theory [35]. Each frequency component of THz radiation can be approximately regarded as propagating like a Gaussian beam. The beam waist size, w_0 , at the focus of an ideal lens, which has a focal length of f is inversely proportional to the frequency ν as [36]

$$w_0 = \frac{cf}{A\pi\nu}, \quad (2.4)$$

where c is the velocity of light in vacuum and A is the size of the input beam. Higher frequency components are, therefore, focused more tightly and expand faster than lower frequency components. When the THz pulse propagates away from the focus, the spectrum becomes narrower due to the faster reduction of higher frequency components. As a result, the pulse was broadened. Far away from the focus, beams of all frequency components expand, which results in the reduction of magnitude of the axial wave form. The shift of pulse peak toward negative time indicates that the THz pulse has a superluminal velocity (higher than the speed of light). In other words, we can detect THz radiation at the position far from the emitter earlier than near the emitter. This interesting phenomenon is explained by considering the optical length of on- and off-axis rays. Both rays have the same optical path length at the focus. Away from the focus, the off-axis ray is shorter than the other. This results the off-axis contribution of the pulse arriving faster than that of the on-axis ray. In contrast, a pulse which contains many cycles of field oscillations, such as optical pulses, off-axis contributions are canceled out because of the destructive interference among them, and only the on- and near-axis rays contribute to the axial waveform. The simulation of pulse propagation on the axis was performed based on Gaussian beam theory. The simulation started from the calculation of surface field at the THz emitter using the current surge

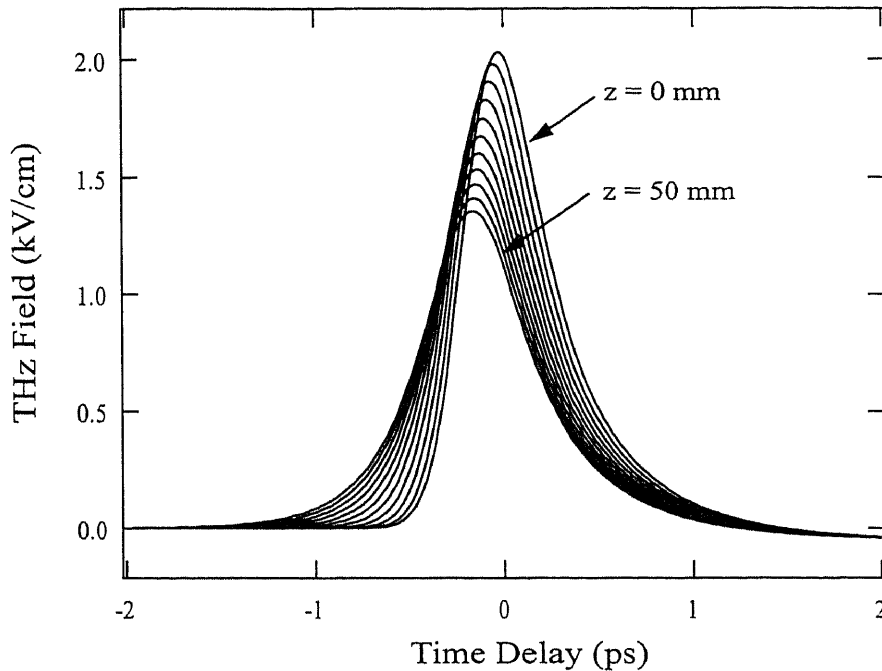


Figure 2.5: Simulation results based on the Gaussian beam theory of THz propagation along the propagation axis z .

model [20]. The change of simulation waveforms agrees well with the experimental waveforms as shown in figure 2.5.

In summary, the large-aperture antenna with GaAs as a semiconductor substrate produces a nearly half-cycle electric field. The pulse has broad spectrum extending from dc to a few THz. Since the half-cycle THz pulse contains a significant portion of low-frequency components, it undergoes a number of changes in shape while propagating. The waveform at the focus is almost symmetric. In actual experiments, this is the clue to indicate that where the focal point is. The superluminal velocity of THz pulse was observed. The Gaussian beam theory can explain the propagation of the THz pulse.

2.4 Spatial distribution of focused THz beam

In a widely used mode of THz image measurements, an object is placed on the focal plane of a relatively weak THz beam, and the object is translated for image acquisition [37]. Since the image, in this mode, is constructed pixel by pixel, acquiring a two-dimensional image by this method consumes a lot of time. To achieve real-time detection, an expanded beam of relatively intense THz pulses is used in that an object is placed in beam path. In this method, large-area electro-optic crystals and a CCD camera are used for the detection of the THz intensity distributions of collected beam.

To achieve real-time acquisition of THz images of objects, the spatial distribution of the observed electric field should be known first. In this section, we present the time-resolved measurements of the spatial profile of focused THz field near and on the focal plane. The observed features were reproduced by diffraction integral calculations. We also showed that the paraxial Gaussian beam model is valid for the description and prediction of the tendency of the ring formation.

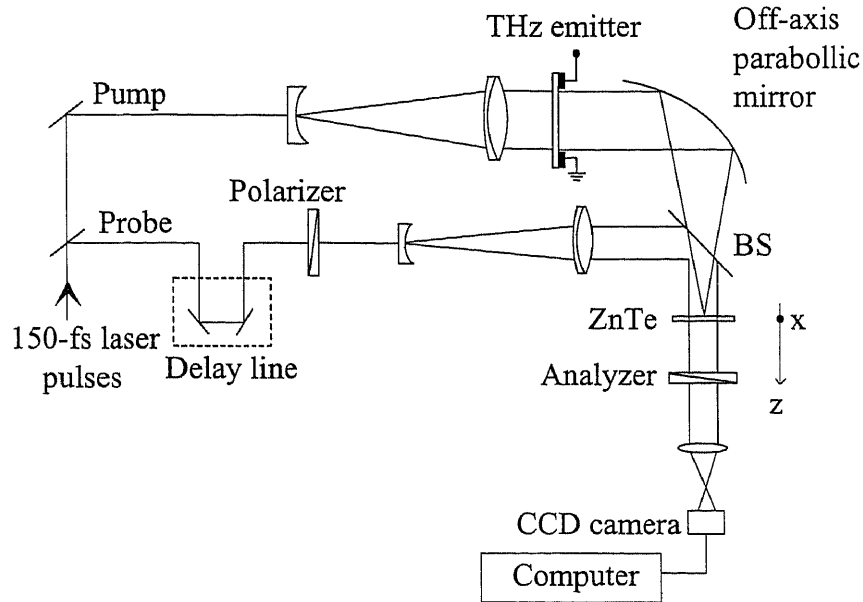


Figure 2.6: Experimental setup for detecting two-dimensional intensity distribution with an expanded probe beam.

2.4.1 Imaging system

Figure 2.6 shows a schematic of the setup used to perform the THz imaging experiment. The large-aperture photoconductive antenna is consisted of a non-doped semi-insulating GaAs wafer with a $\langle 100 \rangle$ surface and two aluminum electrodes mechanically attached to it with a spacing of 30 mm. The diameter and the thickness of the wafer were 50 mm and 350 μm , respectively. Pulsed electrical voltage of 8 kV with pulse duration of 1 μs and repetition rate of 1 kHz was applied to the electrodes synchronously with the pump laser pulse.

Regeneratively amplified Ti:sapphire laser pulses (Spitfire, Spectra Physics) with duration of 150 fs were used as the light source in the experiment. The wavelength and repetition rate of the output of the amplifier were 800 nm and 1 kHz, respectively. The amplified laser beam was first split into two limbs by a beam splitter. The main portion of the beam was passed through the beam splitter and used to pump the GaAs emitter. The remainder was reflected by the beam splitter and used as the probe pulses of the electro-optic sampling measurements. The reflected beam was guided to a delay line before passing through a polarizer. The probe beam was then expanded and collimated by a combination of a convex lens and an achromatic lens to ensure the full area of the ZnTe crystal being used. The pump beam was also expanded and collimated before incident at the emitter. The energy of the pump pulse was 150 μJ . The fluence of the pump pulse at the center of the emitter was 56.4 $\mu\text{J}/\text{cm}^2$. In order to focus and form an image, the THz beam was brought to an off-axis parabolic reflecting mirror with a focal length of 152.4 mm that was placed at 65 mm from the emitter. The diameter of the mirror was 50.8 mm. A 1-mm-thick $\langle 110 \rangle$ ZnTe crystal was used as an EO crystal for the EO sampling measurements of the THz field. The active area on the detection plane was $18 \times 20 \text{ mm}^2$. The EO crystal was located normal to the propagation direction (z). The crystal was oriented so that the (001) direction was parallel to the THz polarization (horizontal) direction. An polarization analyzer was placed so that the probe light is blocked when no electric field is applied to the EO crystal. The polarization direction of the analyzer was at 45° from the horizontal. In this configuration, the intensity of the light transmitted

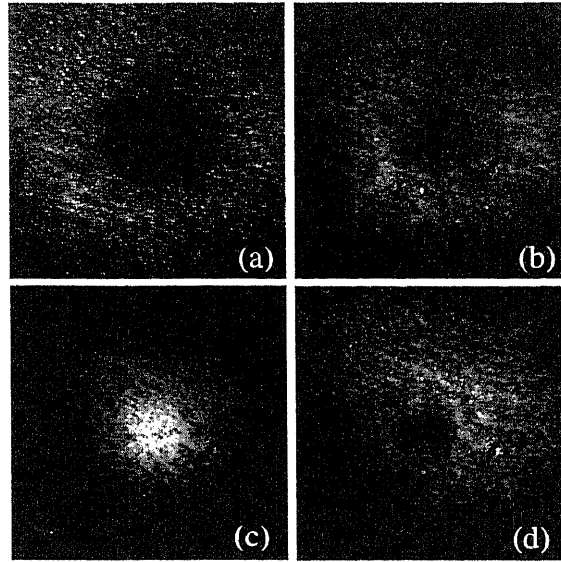


Figure 2.7: Experimentally obtained images of the THz intensity distribution on the focal plane at (a) $t = -0.72$ ps, (b) $t = -0.48$ ps, (c) $t = 0$ ps and (d) $t = 0.4$ ps. Each image corresponds to an area of $12 \times 12 \text{ mm}^2$ at the EO crystal.

through the analyzer is proportional to the square of the electric field at the EO crystal. The transmitted light was passed through a convex lens with a focal length of 26.5 mm and incident on a CCD camera so that a 1/5 image of the THz intensity distribution at the EO crystal was obtained by the CCD camera. The chip of the CCD camera (Electrim EDC-2000N) contains 652×494 pixels, which the pixel size of $7.4 \times 7.4 \mu\text{m}^2$. The background light intensity arisen from the scattering light within the EO crystal [38] was subtracted from the acquired image data.

2.4.2 Experimentally observed the ring formation of focused THz beam

In the present studies, we performed two series of experiments to clarify the spatio-temporal characteristics of the ring formation. In the first one, we placed the ZnTe crystal at the focal point ($z = 0$), and observed the time-dependent spatial distribution of the THz field on the focal plane by scanning the delay time. In the other series of experiments, we observed the dependence of the THz field distribution on the propagation distance. In this case, the whole setup of the EO measurements, i.e., the EO crystal, the analyzer, lens and the CCD camera, was translated along the propagation axis from $z = 0$ to 50 mm. Images at positions with negative values of z could not be obtained because of contact between optical elements. The delay time of the probe pulse with respect to the pump pulse was fixed at the time when the THz field at the focus was maximum. Figure 2.7 shows the measured THz images on the focal plane with the size of $12 \times 12 \text{ mm}^2$ (or $2.4 \times 2.4 \text{ mm}^2$ on the surface of the CCD camera). Figure 2.7(a)-(d) show the spatial distribution of the intensity of focused THz pulses at various delay times. It is seen from figure 2.7(a) that at the beginning, the field distribution forms a ring shape. Figure 2.7(b) shows that the inner rim of the ring gradually expands to the center as time proceeds. Then, the hole of the ring is filled and THz field comes to have the highest intensity at the center as shown in figure 2.7(c). One dimensional intensity profile on the horizontal line that passes through the center of this image has a $1/e$ radius of 3.4 mm. Here, we let the delay time of this image to be the origin. After this time, the tendency of the distribution changes reversely to the direction mentioned above, as seen in figure 2.7(d). Asymmetry seen in the images is attributed to the following two reasons. One is the misalignment of the parabolic mirror that is difficult to steer. The other is fundamental asymmetry of the off-axis parabolic mirror [39]. Figure 2.8 shows on- and off-axis temporal intensity profiles of the THz pulses obtained from the

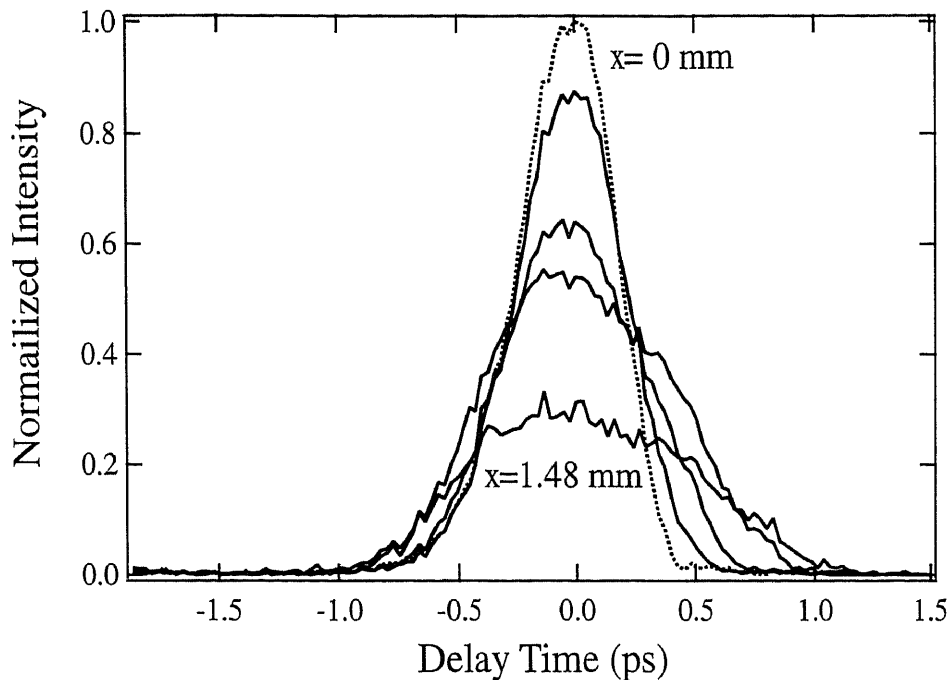


Figure 2.8: Temporal intensity profiles of the THz pulses reconstructed from the set of time-resolved images as shown in figure 2.7. The data for each waveform are extracted from a fixed position of 100 frames of images. The dotted line represents the data at the center ($x = 0$ mm) of the image. The other four waveforms (solid lines) are taken from points shifted upward by a step of 0.37 mm.

time-dependent imaging data corresponding to figure 2.7. The data for each pulse are extracted from a fixed position of 100 frames of images. The on-axis ($x = 0$ mm) waveform has the smallest pulse width. The pulses taken at the positions farther from the axis ($x \neq 0$ mm) are longer. By going away from the center, the peak intensity becomes smaller and the pulses broaden. It is seen from the figure that at delay times larger than about 0.5 ps, the off-axis intensity is larger than the on-axis one. It is also the case with negative delay time smaller than about -0.5 ps. This means that the spatial distribution of the intensity exhibits a ring-like profile at these delay times as seen in the images of figure 2.7.

As the result of changing the image position in the other experiment, the spatial intensity distribution on the planes at $z = 0, 20, 40$ and 50 mm has been shown in figure 2.9. Here, $z = 0$ mm corresponds to the focal plane. The images correspond to an area of 12×12 mm² at the EO crystal. The delay time of the probe pulse of the EO measurement with respect to the pump pulse was fixed at the time ($t = 0$ ps) of the peak of the temporal waveform at the focus. Interestingly, we obtained ring-like intensity distribution again.

2.4.3 Numerical simulation of focused THz beam

In order to confirm the ring formation phenomena observed in the experimental images, we performed numerical simulations of two-dimensional images based on the diffraction integral formula. The merit of this model is that we need no assumption about the characteristic of wave propagation. Moreover, it can include various details of the experimental setup such as the shapes of the emitter or the other optical elements and the spatial distribution of the bias field on the emitter surface. A computer code of the vector-field diffraction integral to simulate the focusing by an off-axis parabolic mirror using the geometrical shape of the mirror surface was newly developed. On the other hand, one can also model using the requisite assumption that each frequency component contained in a THz pulse conducts oneself like a Gaussian beam. This model is simple compared with the preceding one and includes only some details of the experiment setup but can visualize characteristics

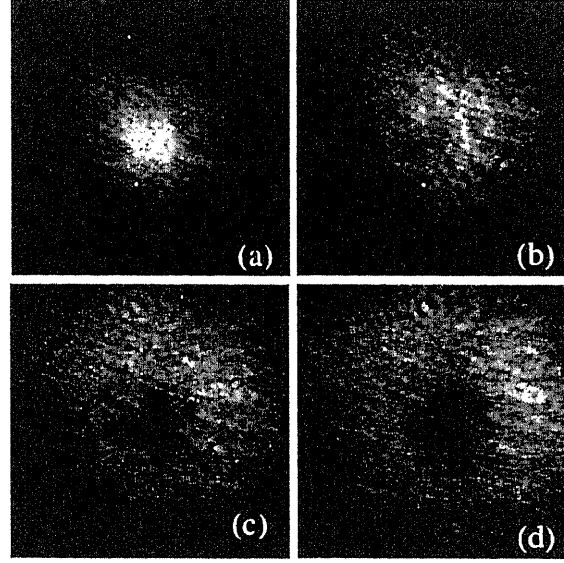


Figure 2.9: Experimentally obtained images of THz intensity distribution at a fixed delay time, $t = 0$ ps, on the plane at (a) $z = 0$ mm, (b) $z = 20$ mm, (c) $z = 40$ mm and (d) $z = 50$ mm.

of THz pulse focusing.

Current Surge Model

The simulation starts from the calculation of the THz field at the antenna surface, which we call the surface field. We adopted the current surge model, which is widely applied to describes the THz radiation generation process [14, 20]. In this model, the time-dependent surface field is given by

$$E_{\text{surf}}(t) = -E_{\text{bias}} \frac{\sigma_s(t)\eta_0}{\sigma_s(t)\eta_0 + (1 + \sqrt{\epsilon})}, \quad (2.5)$$

where E_{bias} is the bias field, $\sigma_s(t)$ is the time-dependent surface conductivity, ϵ is the dielectric constant of the emitter medium, and η_0 is the impedance of vacuum. We adopted the phenomenological distribution of the bias field on the emitter surface as [14]

$$E_{\text{bias}}(x) = E_c + (E_e - E_c)(2x/a)^n. \quad (2.6)$$

Here, the x -axis is set in the direction of the biased field with its origin located at the center of the emitter, $a = 30$ mm is the emitter width and $n = 6$. The surface conductivity is given by [14]

$$\sigma_s(t) = \frac{e(1-R)}{h\nu} \int_{-\infty}^t \mu(t-t') I_{\text{opt}}(t') \exp[-(t-t')/\tau_{\text{car}}] dt', \quad (2.7)$$

where e is the elemental charge, R is the reflectance of the optical pump beam that has the intensity of $I_{\text{opt}}(t)$, τ_{car} is the carrier lifetime. The time-dependent electron mobility, $\mu(t)$, is expressed as,

$$\mu(t) = \mu_{\text{dc}} - (\mu_{\text{dc}} - \mu_i) \exp(-\Gamma t). \quad (2.8)$$

Here, the initially mobility, μ_i , of hot carriers photoexcited to state above the bottom of the conduction band increases to the steady-state mobility, μ_{dc} , of the carriers at the bottom of the conduction band with the carrier relaxation time of Γ^{-1} .

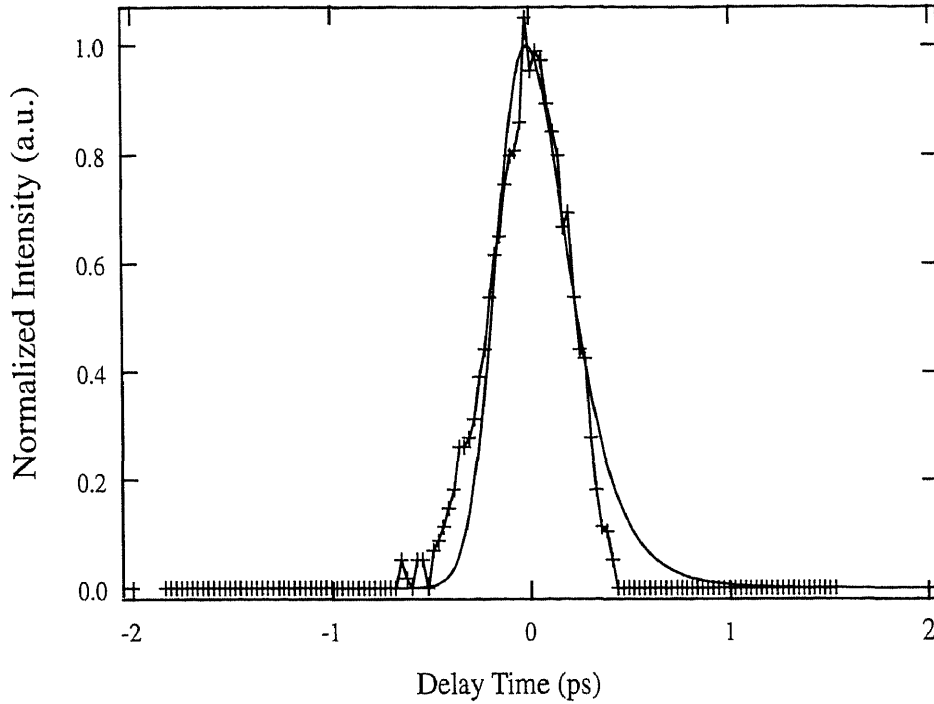


Figure 2.10: Temporal intensity profiles of the THz pulse at the focus obtained from the experimental data (line and crosses) and a simulation with an effective pump pulse width of 550 fs (solid line).

Diffraction integral

The diffraction integral formula for the full electric field vector is known as the Smythe-Kirchoff diffraction integral [40]. The time-domain version of the electric field at position \mathbf{x} and time t is given by [14]

$$\mathbf{E}(\mathbf{x}, t) = \nabla \times \int_S \frac{1}{2\pi r'} [\mathbf{n} \times \mathbf{E}(\mathbf{x}', t - r'/c)] d\mathbf{x}'. \quad (2.9)$$

Here, S is the surface from which the THz radiation is emitted, \mathbf{n} is the inward normal of the emitter surface and \mathbf{x}' is the integration vector on the emitter. Vector \mathbf{r}' is defined by $\mathbf{r}' = \mathbf{x}' - \mathbf{x}$ and $r' = |\mathbf{r}'|$.

In the simulation, the time-dependent electric field $\mathbf{E}(\mathbf{x}', t)$ on the emitter surface was obtained using equation (2.5). The Gaussian spatial distribution of the pump pulse fluence with a $1/e$ radius of 9.2 mm was incorporated in the calculation. THz field waveforms on the surface of the parabolic mirror were, then, calculated using the diffraction integral. Finally, the waveforms at the observation points and the electric fields on the observation plane were calculated using the integral again. The source field of this step was the field reflected from the parabolic mirror surface, which has a tangential component equal to -1 times that of the incoming field. The surfaces of the emitter and the parabolic mirror was divided into 128×128 sections in the numerical integration. The pulse shape of the pumping light was assumed to be Gaussian as

$$I_{\text{opt}}(t) \propto \exp(-t^2/\tau_{\text{las}}^2). \quad (2.10)$$

To simulate the THz images, we used the following value [14]: $R = 0.3$, $\epsilon = 12.25$, $\eta_0 = 377 \Omega$, $\Gamma = 2$ THz, $\mu_i = 500 \text{ cm}^2/\text{V}\cdot\text{s}$, $\mu_{\text{dc}} = 8000 \text{ cm}^2/\text{V}\cdot\text{s}$ and $\tau_{\text{car}} = 600$ ps. The parameter describing the pump laser pulse width, τ_{las} , should be equal to the pump pulse duration divided by $2\sqrt{\ln 2}$. In the simulation, this value was modified from the experimental pulse width of 150 fs to an effective pulse width, as described below, in order to make the simulated THz pulse width consistent with the experimental one.

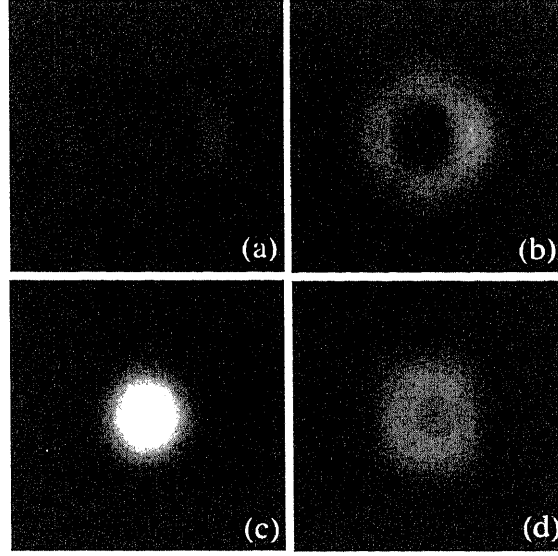


Figure 2.11: Time dependence of the spatial distribution of the THz intensity obtained by the simulations based on the vectorial field diffraction integral. Images (a)-(d) correspond to the experimental images of figure 2.7(a)-(d). The gray scale images indicate the calculated THz intensity distributions on the focal plane at (a) $t = -0.72$ ps, (b) $t = -0.48$ ps, (c) $t = 0$ ps and (d) $t = 0.4$ ps.

When the value of τ_{las} same as the experimental one is used in the simulation, the calculated pulse durations of the temporal waveforms are much shorter than those observed in the experiments. Therefore we adopted an effective pump laser pulse width of 550 fs, which resulted in the simulated THz pulse width equal to the experimental one at the focus. The experimental and simulated temporal waveforms of the THz field at the focus are plotted in figure 2.10. It is seen from the figure that the pulse widths agree with each other but the pulse shapes are slightly different. The simulated waveform rises faster in the rising stage but decreases slower in the decay state. It may be attributed to the screening of the bias field by carriers and the scattering of carriers to the intra-band states, which are not included in the model of the THz generation described above. We leave the work of elaboration of the dynamic model for later studies, and use this model of the generation process of the THz field. In the simulations, no variable parameters were used except for the pump pulse width. The results of the simulations using the diffraction integral formula for the time dependence and the position dependence of the spatial distribution of the THz intensity are shown in figures 2.11 and 2.12, respectively. The simulated images are in a qualitative agreement with those of the corresponding experimental images of figures 2.7 and 2.9. It is apparent that the ring shapes before and after $t = 0$ are different, as seen in figure 2.11. This can be attributed to the asymmetry of the simulated temporal pulse shape as shown in figure 2.10.

Gaussian beam model

Focusing characteristics, such as focused spot size ($1/e$ of radius) and confocal length, generally depends on the frequency. Here, for the sake of simplicity, we assume that each frequency component of the THz pulses emitted from the large-aperture photoconductive antenna behaves as a Gaussian beam [35]. We use a simple model for the optical configuration, where an ideal lens with a focal length of f is placed at z_L from the emitter. The Gaussian beam of each frequency is assumed to have a frequency-independent initial beam size A at the surface of the emitter. Then the beam size of the component with frequency ν at the lens is expressed as

$$w_{z_L}(\nu) = A \left(1 + \frac{z_L^2}{z_0^2(\nu)} \right)^{1/2}, \quad (2.11)$$

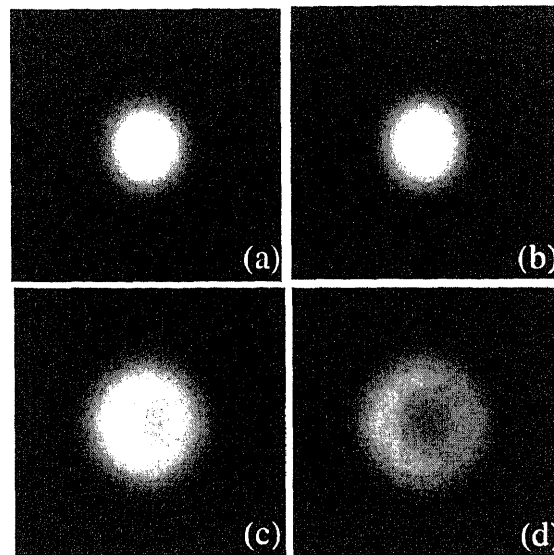


Figure 2.12: Position dependence of the spatial distribution of the THz intensity obtained by the simulations. Images (a)-(d) correspond to the experimental images of figure 2.9(a)-(d). The gray scale images indicate the calculated THz intensity distributions on the plane at (a) $z = 0$ mm, (b) $z = 20$ mm, (c) $z = 40$ mm and (d) $z = 50$ mm.

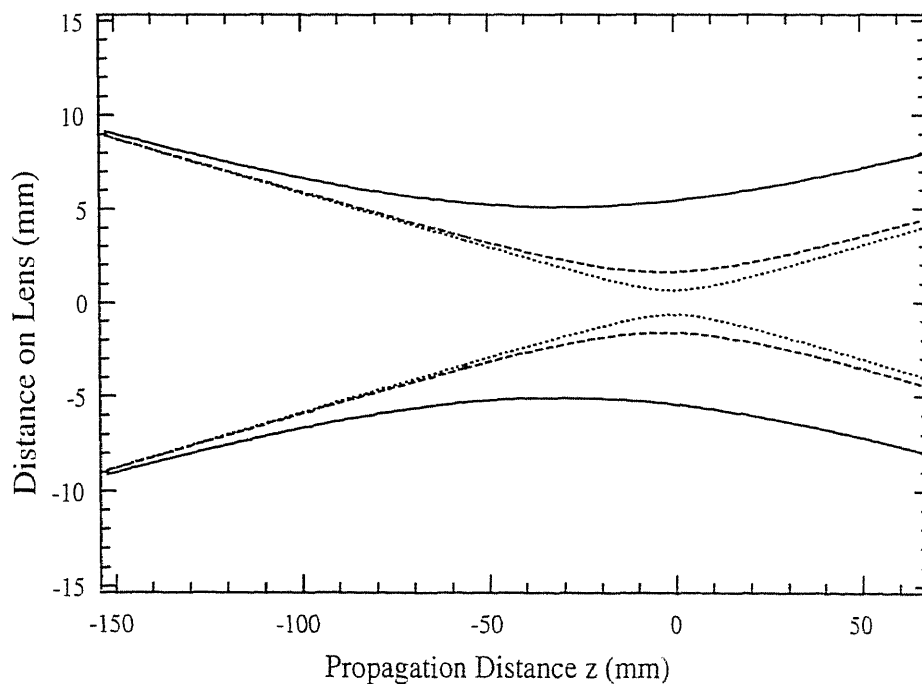


Figure 2.13: Propagation lines (positions where the electric field has $1/e$ peak value) calculated using the Gaussian beam model. The three pair lines starting from the position of the ideal lens represent three different frequency components: 0.3 THz (solid lines), 1.0 THz (dashed lines) and 2.5 THz (dotted lines).

where $z_0(\nu)$ is defined as

$$z_0(\nu) \equiv \frac{\pi A^2 \nu}{c}. \quad (2.12)$$

The radius of curvature of the wave front at the lens is

$$R_{z_L}(\nu) = z_L \left(1 + \frac{z_0^2(\nu)}{z_L^2} \right). \quad (2.13)$$

The radius of curvature is changed from R to R' by passing through an ideal lens as

$$\frac{1}{R'(\nu)} = \frac{1}{R_{z_L}(\nu)} + \frac{1}{f}. \quad (2.14)$$

The effect of the finite size of the lens is taken into account by assuming that the beam size is changed from w to w' by passing through a lens with a diameter D as [36]

$$\frac{1}{w'^2(\nu)} = \frac{1}{w_{z_L}^2(\nu)} + \frac{2}{D^2}. \quad (2.15)$$

The beam waist and its location of the beam focused by the lens can be written as

$$w'_0(\nu) = w'(\nu) \left[1 + \left(\frac{\pi \nu w'^2(\nu)}{c R'(\nu)} \right)^2 \right]^{-1/2}, \quad (2.16)$$

$$z'_f(\nu) = z_L - R'(\nu) \left[1 + \left(\frac{c R'(\nu)}{\pi \nu w'^2(\nu)} \right)^2 \right]. \quad (2.17)$$

For the calculations, we use the parameters same as those of the experimental setup, i.e., $A = 9.2$ mm, $z_L = 65$ mm, $f = 152.4$ mm and $D = 50.8$ mm. The focusing characteristics of Fourier components with several frequencies are visualized in figure 2.13 by plotting the propagation distance dependence of the beam size. The figure shows the propagation lines of beam frequency of 0.3, 1.0 and 2.5 THz. In this figure, we locate the focal point of the lens at $z = 0$, that is, the lens is positioned at $z = -152.4$ mm. The positions of the beam waists of these beams are at $z = -30.80$, -3.15 and -0.51 mm, respectively. It is clearly seen that the confocal length of the low frequency component (solid lines) is quite longer than the others, and the corresponding beam waist is larger.

In the following, we explain the ring formation phenomena qualitatively using a Gaussian beam model. When we focus our attention on the focal plane ($z = 0$), and consider the spatial distributions, it is seen that the high frequency components are tightly compressed near the z -axis while beams of low frequency distribute in a larger area as shown in figure 2.13. This frequency dependent spatial distribution results in the position dependence of the THz pulse width in the time domain as evidenced by the experimental result shown in figure 2.8. Briefly, the on-axis pulse width is shortest because it is composed of a broad spectrum including significant contribution of high frequency components, whereas pulse widths at off-axis positions are larger due to the loss of high frequency components.

A qualitative explanation of the z -dependent ring formation phenomenon in the second experiment is as follows. On the focal plane ($z = 0$ mm), the intensity distribution forms a single peak at $t = 0$ ps, and exhibits a ring-like profile at times larger than about 0.5 ps and less than about -0.5 ps as shown above. On the other hand, the position dependence of the temporal waveforms of the THz pulse on the z axis has been reported in our previous paper [36]. The pulse peak time was found to be shifted in the negative direction for larger positive values of z , which has been attributed to the difference in the optical path length for the on-axis and off-axis rays. Because of this peak shift at positions of large z , the delay time region when the ring profile

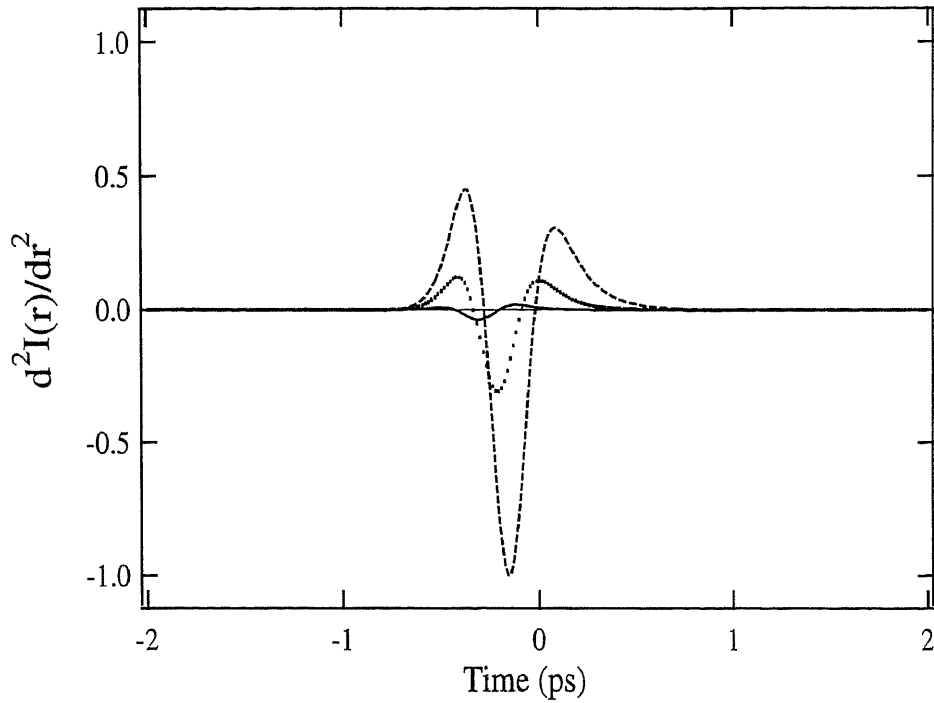


Figure 2.14: The second derivative of the THz intensity with respect to the radial parameter, r , as a function of time. They were obtained by the calculations using the Gaussian beam model. Each line is for the optical pump beam radius of 3 mm (solid line), 6 mm (dotted line) and 9 mm (dashed line), respectively.

appears is also shifted in the negative direction. This has been confirmed by simulation calculations using the diffraction integral method as described in the following section. Thus, a ring-like distribution is observed even at $t = 0$ ps at positions sufficiently away from the focus.

We also used a more analytic approach to study the condition for the ring formation. A ring-like intensity distribution occurs when the following inequality is satisfied:

$$\left. \frac{d^2 I(t, r)}{dr^2} \right|_{r=0} > 0. \quad (2.18)$$

Here, $I(t, r)$ represents the THz intensity at time t and radial position r . We used the Gaussian beam model for the calculation of $I(t, r)$ at the focus with the surface field parameters described in section 2.4.3. The left-hand side of equation (2.18) was calculated as a function of time for different values of pump beam radius. The results are shown in figure 2.14. The plots indicate that a ring-like spatial distribution is formed in the time region when the plotted value is positive. The result with a pump radius of 9 mm shows good agreement with the experimentally obtained time dependence. It is of importance that the ring formation is reproduced not only by the diffraction integral but by the Gaussian beam model. It shows that the ring formation is a very fundamental phenomenon.

It is seen from the figure that a smaller size of the optical pump beam yields a shorter duration of ring formation. Under the Gaussian beam approximation, the contribution of a single frequency component to the left-hand side of equation (2.18) is simplified to

$$\left. \frac{d^2 I(t, r)}{dr^2} \right|_{r=0} \propto \frac{1}{w_0^2}, \quad (2.19)$$

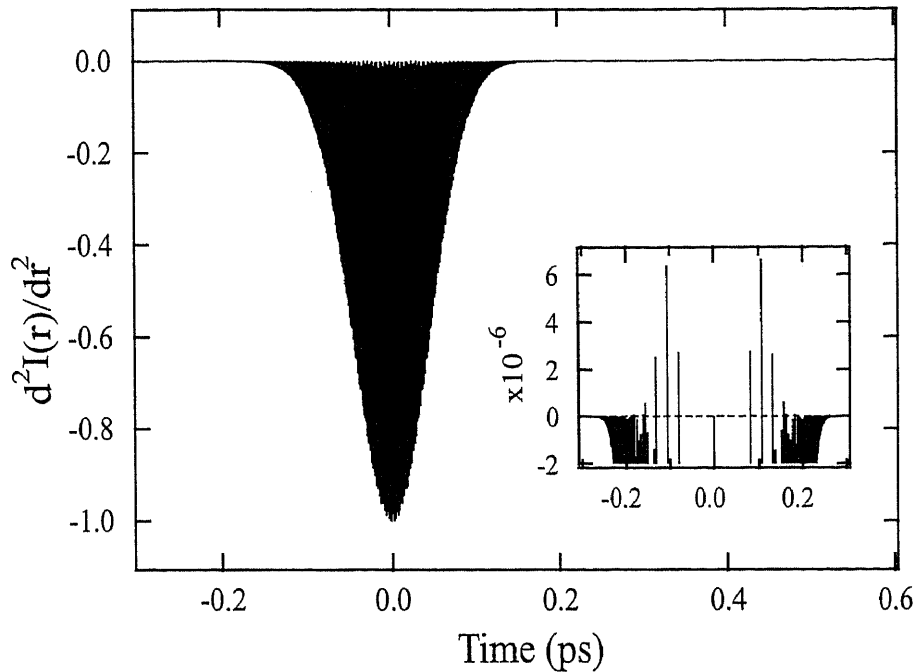


Figure 2.15: Normalized second derivative of the intensity of focused light pulses with respect to the radial parameter, r , as a function of time. It was obtained by the calculations using the Gaussian beam model. The inset picture shows the expanded vertical scale around the zero line (dashed line).

where the beam waist at the focal point is approximately expressed as [36]

$$w'_0 = \frac{cf}{A\pi\nu}. \quad (2.20)$$

Here, it is assumed that the beam radius does not change when the beam propagates from the emitter to the focusing element and that $\lambda \ll (\pi A^2)/f$. From equation (2.20), we can obtain the conclusion that smaller optical pump beam sizes and/or larger focal lengths, f , give larger beam waists and result in smaller changes in the THz pulse width at off-axis positions. This leads to shorter time duration for the ring formation or no ring formation at all.

With ultrashort optical pulses of many-cycle duration, for example, the ring formation phenomenon has been rarely observed. We again used the Gaussian beam model to calculate electric field at the focus of the ideal lens and checked it with the condition in equation (2.18). The time-dependent second derivative of intensity with respect to r of 150-fs pulse at 800 nm is plotted in figure 2.15. The inset picture shows the time region when the on-axis intensity is less than the off-axis one (positive values). It indicates that the ring formation effect is negligible with optical many-cycle pulses on account of very little contribution from low-frequency components.

In conclusion, with a THz imaging system, it has been observed that the two-dimensional spatial intensity distribution of focused half-cycle THz pulses forms a ring-like profile at a certain region of space and time. This has been confirmed by the numerical simulations based on the vectorial diffraction integral formula and the Gaussian beam approximation. This observed phenomenon is attributed to the broad spectrum of half-cycle THz pulses which include a significant contribution of low-frequency components and the corresponding large central wavelength compared with optical elements. It was shown that the time duration of the ring can be controlled by changing the beam size of the optical pump pulses and the focal length of focusing elements.

2.5 Frequency dependence of diffraction

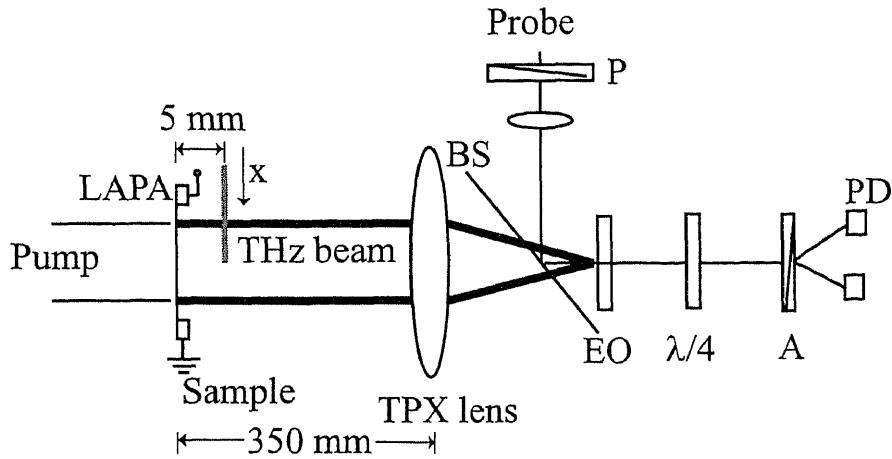


Figure 2.16: Schematic of knife-edge experiment for measuring the THz beam size in front of the emitter.

The spatial profile THz beam emitted from the large-aperture photoconductive antenna ($3 \times 3 \text{ cm}^2$) is too large to be detected by two-dimensional EO method directly because it is not easy to find an EO crystal as large as the THz beam. Typically, a focusing component is used to resize the THz beam. The THz beam is, then, measured at the focal plane or nearby but before being focused [41]. Fortunately, we can apply a well known optical measurement called knife-edge scanning detection to observe the frequency-dependent spatial distribution in front of the emitter. For waves in the optical region, what we can measure is the intensity profile of a light beam using a metal plate, such as a cutter knife or a razor blade, to cut the beam perpendicular to its propagation direction gradually. The transmitted portion is focused to a photo detector. In the case of THz radiation, the electric field can be detected. The frequency-dependent spatial profile is able to be visualized.

In the experiment, as shown in figure 2.16, an aluminum plate, which has a thickness of 0.3 mm, was used as a cutting plate. It was placed at 5 mm from the THz emitter, the same position where a sample is inserted in the imaging experiment. The edge of plate was moving along x direction, in which $x = 0 \text{ mm}$ is defined at the center of the emitter. THz waveforms were recorded each step from $x = -40 \text{ mm}$ to $x = 20 \text{ mm}$. The scanning step was equal to 5 mm. The temporal waveforms of different edge positions were depicted in figure 2.17. At $x > 20 \text{ mm}$, the signal could not be detected. As seen from the graph, the electric field strength decreases as well as the change of waveform where $x > -30 \text{ mm}$. The FFT of this set, shown in figure 2.18, yields information on how the amplitude of each frequency component changes with the position of the aluminum edge. When the edge had not passed the center ($z = 0$), the peak frequencies were at 0.1 THz. The peak frequencies of remained waveforms were shifted to lower because the high frequency portions were almost cut off. If the emitter and lens were placed more closely, frequency components that are lower than 0.1 GHz would have been detected. Amplitude values at frequencies 0.1, 0.3, 1.0 and 1.5 THz (along dashed lines) were plotted versus scanning distances, shown in figure 2.19. The plots were interpolated using a cubic spline method. The sizes of beams, D , were measured at $1/e$ of differentiated position-dependent values. Theoretically, the beam size of each frequency component is the same when emitted from the antenna. From the experiment, after the pulse propagated for a distance of 5 mm, the beam size became bigger. This can be explained as follows. Since the pump beam size was much smaller than the size of the aperture, the lower components were more diffracted out even near the emitter. The second reason is that the scanning step of the aluminum edge was not fine enough. Moreover, the distance between the emitter and lens was too large which was enough for the diffraction of low frequency components.

In conclusion, the distribution of each frequency component can be measured by a knife-edge scanning detection. The beam size depends on frequency when the pulse propagates away from the emitter. The emitter and the lens should be closer to avoid the diffraction of low frequency components that may affect to the desired waveform.

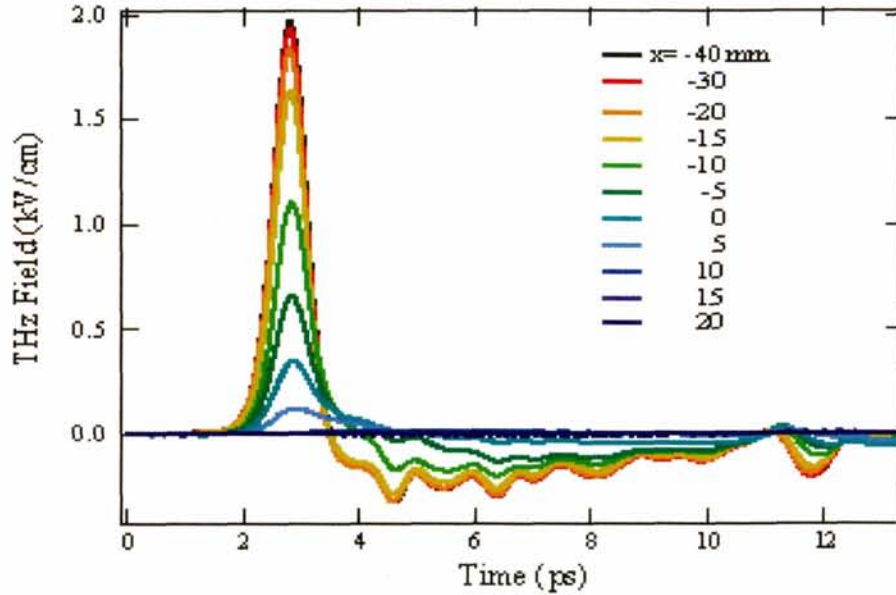


Figure 2.17: Knife-edge position-dependent THz waveforms.

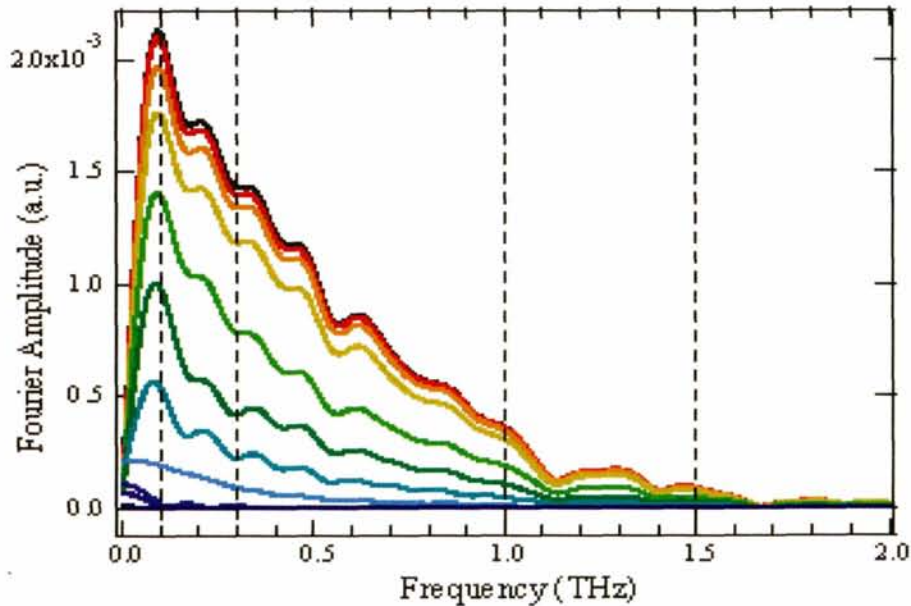


Figure 2.18: Fourier amplitudes of figure 2.17.

2.6 Time-domain terahertz spectroscopy

THz radiation from the large-aperture photoconductive antenna was employed to conduct the time-domain spectroscopy experiment. The substrate was of a focusing substrate called TPX. It is known as an optimal

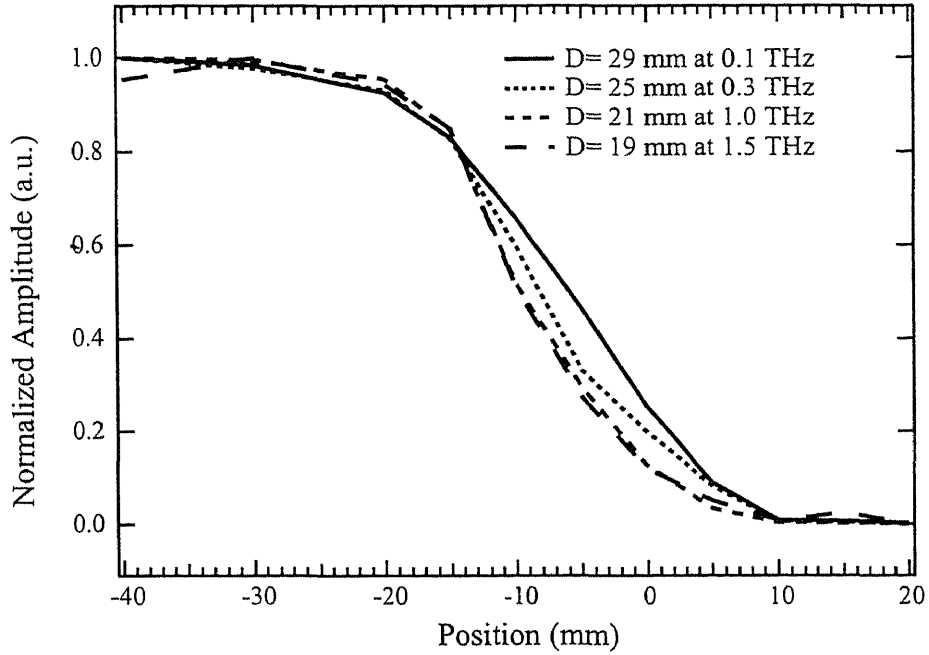


Figure 2.19: Beam diameter of some frequency components.

dielectric with regard to low-losses, hardness, power-handling capability, and optical transparency, which greatly facilitates optical alignment. The TPX was selected for lens construction based on literature reviews and discussions with other engineers experienced in millimeter-wave and submillimeter-wave design [42,43]. In order to handle a TPX lens with THz pulses, the optical properties of TPX material in the matter of broadband frequency range should be known.

The experimental setup for the spectroscopy was similar to that shown in figure 2.3 but the sample (a TPX plate) was inserted between the antenna and the off-axis parabolic mirror. The samples have 4.7-mm and 9.6-mm thick and 80 cm in diameter. The bulk properties of the sample were then observed by the THz beam. The temporal waveforms in the absence (reference) and presence (sample) of the TPX were measured by the electro-optic sampling.

The observed waveforms were shown in figure 2.20. The sample pulses were delayed by the TPX substrate. This happens because the refractive index of the sample is larger than the refractive index of air. This is a very basic fact, but it illustrates one of the special features of THz-TDS, that one can detect the absolute phase of the THz pulses. Figure 2.21 shows the comparison of pulse shapes by neglecting the effect of propagation time delay in the samples. There is no significant difference in waveforms, except for the decreasing of peak and small broadening of pulses of the order of ten femtoseconds. It shows that TPX material is proper for a THz experiment because of its low absorption and dispersion. The optical properties of the material were described as follows.

The amplitude and phase of each pulse are shown in figures 2.22 and 2.23, respectively. Obviously, the amplitude of sample pulses is weaker than that of the reference pulse. This is caused by two reasons. The main reason is absorption in the samples. The other is a loss at the sample interfaces. For simplicity, the absorption coefficient will be calculated by considering only absorption.

Supposing that the measured electric field is $E(t)$ and its spectrum is $\tilde{E}(\omega)$. The reference wave propagation through free space with a distance of l is given by

$$\tilde{E}_{\text{ref}}(\omega) = \tilde{E}_0 e^{ikl}, \quad (2.21)$$

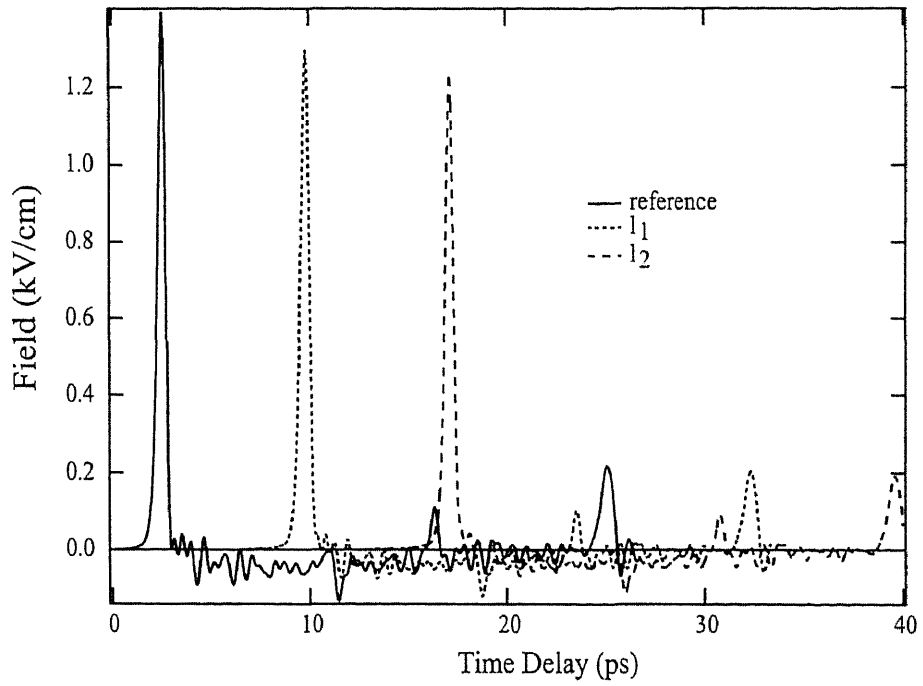


Figure 2.20: The pulse propagated through free space (reference) and through TPX plates of different thicknesses ($l_1 = 4.7$ mm, $l_2 = 9.6$ mm).

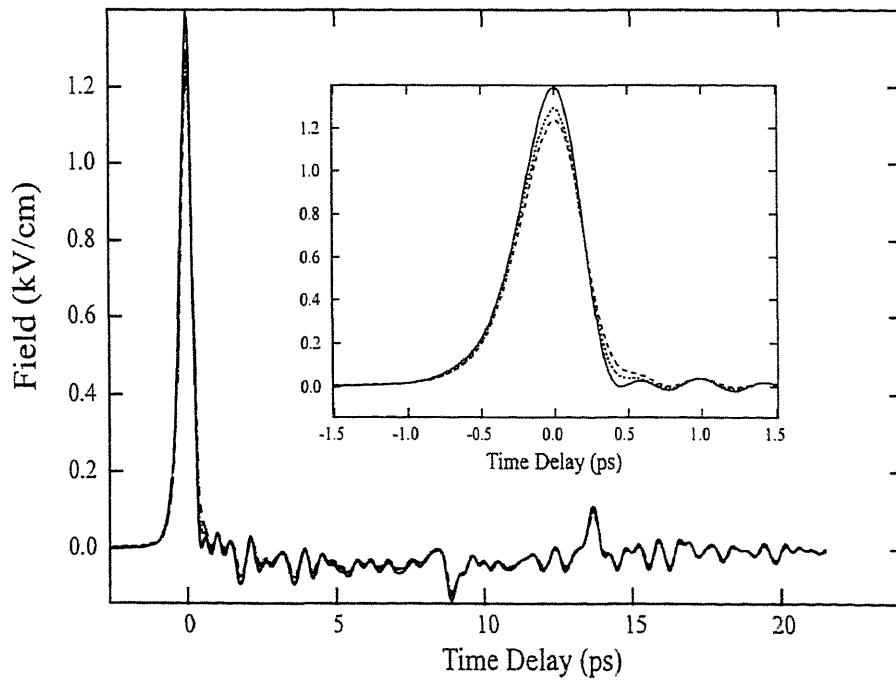


Figure 2.21: Comparison of reference (solid line) and sample waveforms (l_1 : dotted line, l_2 :dashed line) where the time delay was shifted such that each pulse peak coincides.

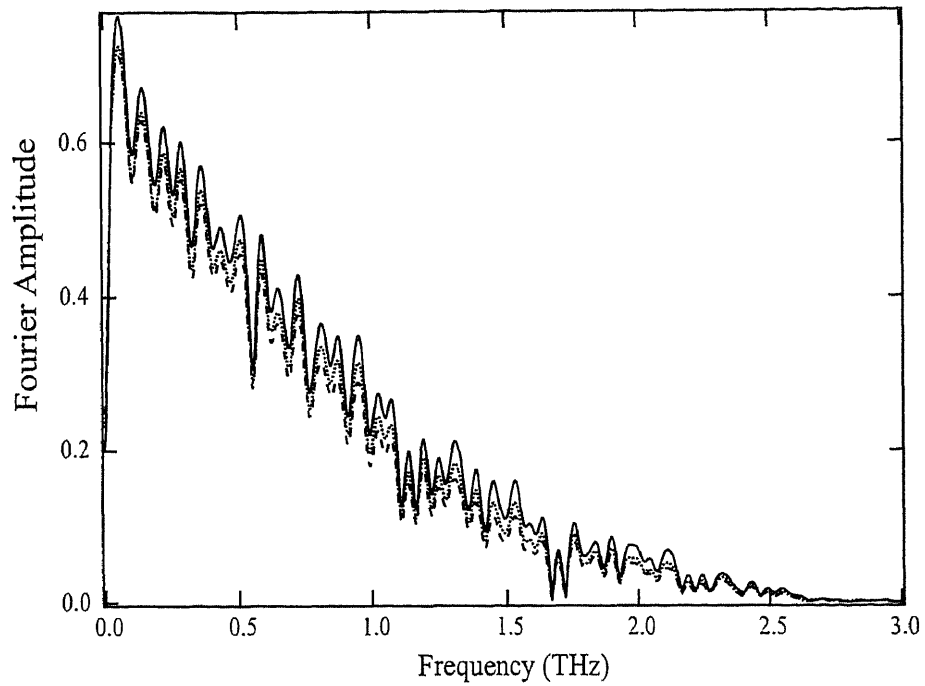


Figure 2.22: Fourier spectra of THz pulses in figure 2.20; reference (solid line), l_1 (dotted line) and (l_2) dashed line.

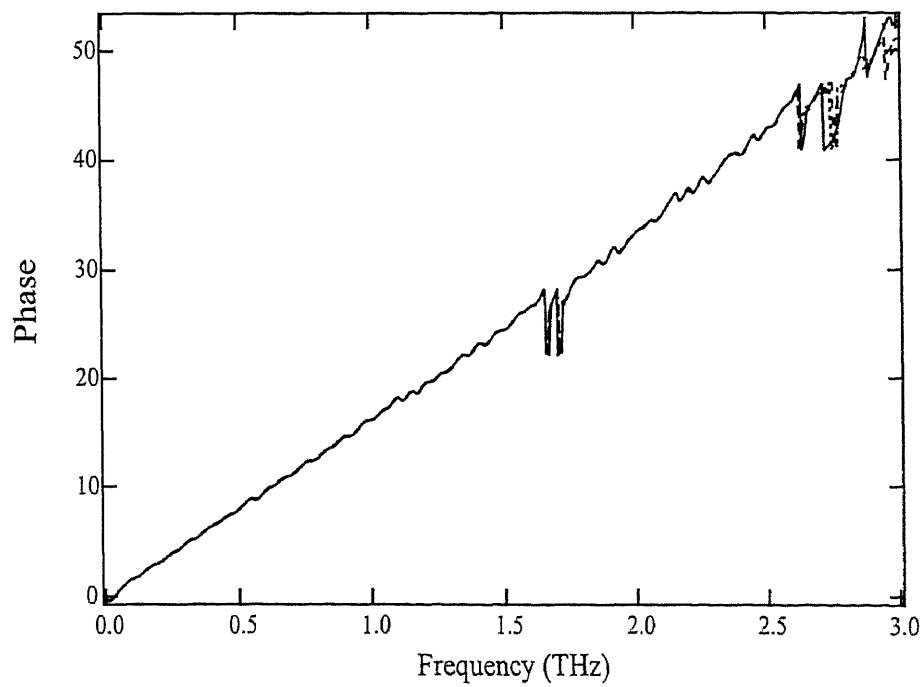


Figure 2.23: Phase of THz pulses in figure 2.20.

where $k = \frac{\omega}{c}$. When the wave passes through the l -thick sample,

$$\tilde{E}(\omega) = \tilde{E}_0 e^{\frac{i\omega l}{v} - i\omega\Delta t}. \quad (2.22)$$

We now consider that the refractive index is complex. It is given by [44]

$$\tilde{n} = n(1 + i\xi), \quad (2.23)$$

we therefore get

$$\begin{aligned} \tilde{E}(\omega) &= \tilde{E}_0 e^{\frac{i\omega n l}{c}(1+i\xi) - i\omega\Delta t} \\ &= \tilde{E}_0 e^{-kn\xi l} e^{i(knl - \omega\Delta t)}. \end{aligned} \quad (2.24)$$

By applying an absolute value to both side of eq. (2.24) the ratio of sample and reference field,

$$\left| \frac{\tilde{E}(\omega)}{\tilde{E}_{\text{ref}}} \right| = e^{-kn\xi l}. \quad (2.25)$$

Generally, absorption coefficient is defined by

$$\alpha = 2kn\xi. \quad (2.26)$$

The absorption is then given by the ratio of the sample and reference spectra as

$$\alpha(\omega) = -\frac{2}{l} \ln \left| \frac{\tilde{E}(\omega)}{\tilde{E}_{\text{ref}}} \right|. \quad (2.27)$$

In the experiment, we have an alternative way to find the absorption coefficient from the ratio of field passing through samples of different thickness. The absorption coefficient can be written as

$$\alpha(\omega) = \frac{2}{l_2 - l_1} \ln \left| \frac{\tilde{E}_1(\omega)}{\tilde{E}_2(\omega)} \right|. \quad (2.28)$$

Here the thickness $l_1 = 4.7$ mm and $l_2 = 9.6$ mm. The absorption coefficients versus frequency calculated from eq. (2.27) and eq. (2.28) are shown in figure 2.24. It is obvious that values of the coefficient calculated by using the reference spectrum are larger than the other one. The neglecting of Fresnel-loss at interfaces should be the cause of this inconsistency. Hence, the exact value of the absorption coefficient is the one that used the ratio of difference thickness amplitudes. From the graph, the wave is absorbed less in the low-frequency region. The dramatically high absorption around 1.7 THz is caused by water vapors absorption. We now calculate the frequency-dependent refractive index, n , from the THz spectra. It also follows from eq. (2.24) and that

$$e^{ikl(n-1) - i\omega\Delta t} = \frac{\tilde{E}(\omega)/\tilde{E}_{\text{ref}}(\omega)}{\left| \tilde{E}(\omega)/\tilde{E}_{\text{ref}}(\omega) \right|}. \quad (2.29)$$

With this equation, we can extract the refractive index

$$ikl(n-1) - \omega\Delta t = \ln \left(\frac{\tilde{E}(\omega)/\tilde{E}_{\text{ref}}(\omega)}{\left| \tilde{E}(\omega)/\tilde{E}_{\text{ref}}(\omega) \right|} \right)$$

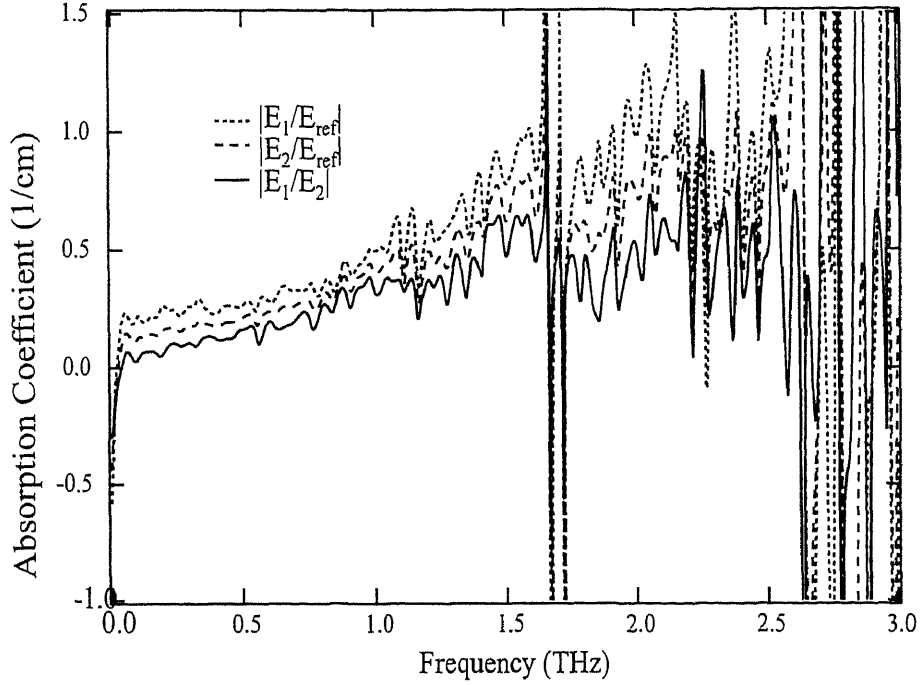


Figure 2.24: Frequency-dependent absorption coefficients for different calculation methods.

$$= i(\theta - \theta_{\text{ref}}).$$

As seen from figure 2.23, the phase difference $\theta - \theta_{\text{ref}}$ is almost zero in the frequency region of interest. Therefore the right-hand side of eq. (2.30) vanishes. This means that the refractive index of TPX is constant along the interesting broadband frequency range of interest. Hence, the refractive index is simply calculated as

$$\Delta t = \frac{(n-1)l}{c}, \quad (2.30)$$

where Δt is the different delay time between the peak of sample pulse and that of the reference pulse, c is the velocity of light in vacuum. By using the time delay of extracted from figure 2.20, i.e. 7.227 ps, and the sample with a thickness of l_1 , the refractive index is 1.46.

Slab Theory

The absorption coefficients of TPX are calculated without consideration of a loss at interface and a finite thickness of samples in previous section. We now apply the theory of wave incident upon a slab in one dimension to get more accuracy.

Now let's assume that the slab consists of isotropic material having a complex index n and its thickness is a . The slab lies between $x = 0$ and $x \geq a$ as shown in figure 2.25. The refractive indices outside the slab are chosen to be unity. The electric field of the incident plan wave is described as

$$E(x) = E_1^+ e^{ikx}. \quad (2.31)$$

Since part of the wave may be reflected by the slab, the total field in left region is

$$E_1(x) = E_1^+ e^{ikx} + E_1^- e^{-ikx}. \quad (2.32)$$

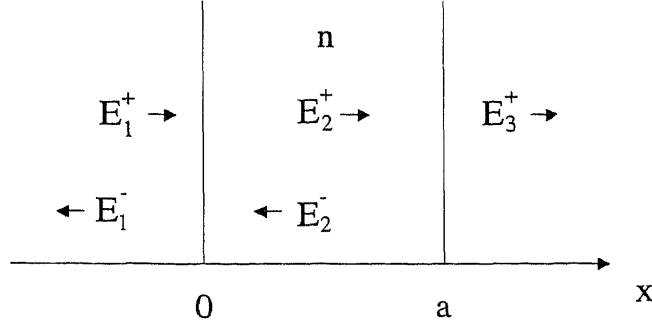


Figure 2.25: Finite-thickness slab.

In the slab ($0 < x \leq a$), $E(x) = E_m$, which is the sum of a left-moving and a right-moving wave, of the form

$$E_m = E_m^+ e^{inkx} + E_m^- e^{-inkx}. \quad (2.33)$$

In $x \geq 0$ region there is only the rightward-moving transmitted wave, $E_m^+ e^{ikx}$. Expression of the unknown E_1^- , E_2^+ , E_2^- , and E_3^+ are obtained by enforcing the boundary conditions at the interfaces, $x = 0$ and $x = a$ as [45]

$$E_1^- = E_1^+ \frac{(1 - e^{i2nka})(n^2 + 1)}{d}, \quad (2.34)$$

$$E_2^+ = \frac{-2(n+1)}{d}, \quad (2.35)$$

$$E_2^- = \frac{-2ne^{i2nka}(n-1)}{d}, \quad (2.36)$$

$$E_3^+ = \frac{-4me^{ika(n+1)}}{d}, \quad (2.37)$$

where d is defined as $d = e^{inka}(n-1)^2 - (n+1)^2$. The transmitted field E_3^+ was obtained from above experiment, the imaginary part of n can then be calculated using eq. (2.37). Although the incident field, E_1^+ , cannot be measured, we can use the reference field as

$$\begin{aligned} \frac{E_{11}}{E_{\text{ref}}} &= \frac{-4me^{ika(n+1)}}{de^{ika}} \\ &= \frac{-4me^{ika(n+2)}}{d}. \end{aligned} \quad (2.38)$$

Using eq. (2.38), the absorption coefficients, α , are numerical calculated as shown in figure 2.26. The values from different thicknesses agree with each other and less the previous calculation.

In summary, we observed the absorption coefficient of the TPX substrate using THz time-domain spectroscopy. The TPX substrate was tested for the purpose of using it as a focusing object for the imaging setup. The calculations of absorption coefficient with different theoretical approaches show that a TPX lens does not strongly absorb the THz waves in the range of 0 - 2 THz. The lens with thickness of 2 cm allows about 36 percent of the input intensity to pass through.

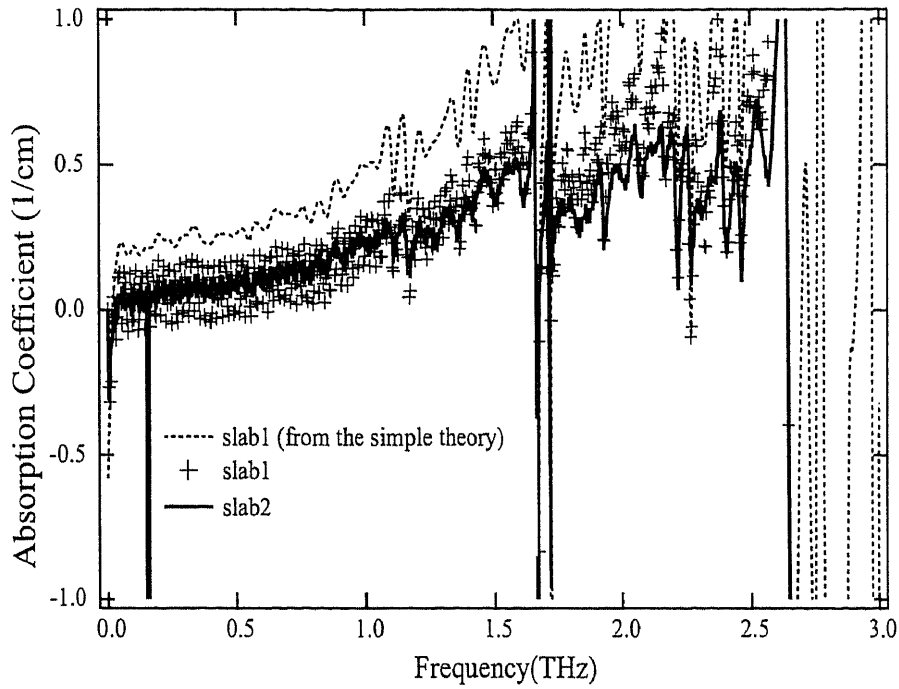


Figure 2.26: Absorption coefficient based on the slab theory.

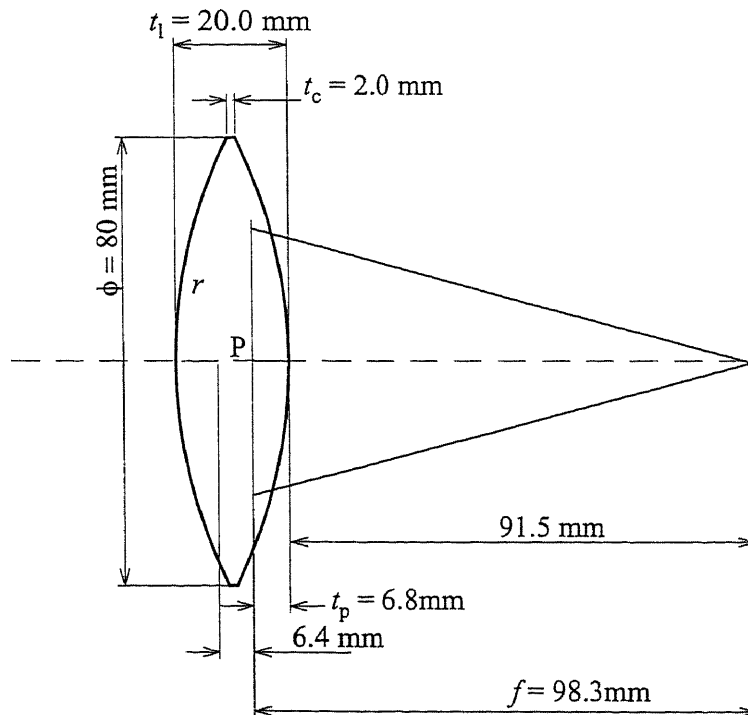


Figure 2.27: Symmetric-convex TPX lens (not to scale).

2.7 TPX lens performances

The TPX lens for the imaging system was designed to have a focal length $f = 100$ mm for focusing the THz beam having a $1/e$ radius of electric field of 9.2 mm. Because the absorption of the TPX material limits the output power of the THz radiation, the center thickness of the lens should be concerned. Theoretically, parameters of a thick lens (refractive index n , diameter ϕ , center thickness t_1) with symmetrical radii r have the relation as [46]

$$\frac{1}{f} = \frac{2(n-1)}{r} - \frac{(n-1)^2}{nr^2} \left[t_1 + 2r \left\{ 1 - \cos \left(\arcsin \frac{\phi}{2r} \right) \right\} \right]. \quad (2.39)$$

This equation is valid when the length between the principle planes (denoted t_c , in figure 2.27) is equal to zero. With edge thickness at the center, t_1 , constrained, the lens radius r can be approximated by using numerical methods to solve eq.(2.39). So far, the length between the primary point P to the center edge, t_p , is given by [46]

$$t_p = \frac{rt_1}{2nr + t_c(n-1)}. \quad (2.40)$$

Realistically, t_c is not negligible. It should be, therefore, designed as thin as possible for less absorption. From figure 2.26, the field of lower frequency components are absorbed less than that of higher frequency components. The dramatic absorption around 1.7 THz is due to water vapors absorption. For instance, at frequency 1.5 THz the absorption coefficient α is about 0.5 cm^{-1} . The ratio of the coming intensity to the transmitted intensity at the center of a 2-cm thick lens is

$$\begin{aligned} \frac{I}{I_0} &= e^{-\alpha l} \\ &= e^{-0.5 \times 2} \\ &= 0.37. \end{aligned}$$

2.7.1 Aberration

In monochromatic light there are spherical aberration, astigmatic, coma and distortion. In polychromatic light there is other aberration that arises when a lens is used to focus light containing multiple wavelengths, called chromatic aberration. Basically, the index of refractive of a material is a function of frequency, known as dispersion. From Snell's law $n_1 \sin \theta_1 = n_2 \sin \theta_2$, it can be seen that light rays of different wavelengths or color will be refracted at different angles since the index is not constant. Because the index of refraction is higher for lower frequency waves, these are focused closer to the lens than higher frequency waves. In THz pulses containing broadband frequency components, the fact that lower frequency components are focused closer to the lens, as shown in figure 2.12, does not arise from the chromatic aberration. This is because of the fact that the refractive index of the TPX lens is constant in the interesting THz frequency range as can be seen in figure 2.23. Not only the focal length, but the beam waist of the THz waves also depends on the frequency. Even the off-axis parabolic is used as a focusing element, it provides the same tendency as describe in section 2.3. This confirms that the lens does not have chromatic aberration. However the focal length of each frequency component can be aligned at the same position using a terahertz binary lens [47].

2.7.2 Diffraction effects

Diffraction effect traditionally classified into either Fresnel or Fraunhofer types. Fresnel diffraction is primarily concerned when the illumination source is close to a diffraction object or aperture. On the other hand, Fraunhofer diffraction happens when the object (or aperture) is illuminated with an infinite source (plane-wave illumination) and the light is sensed at an infinite distance (far field) from this object. A lens or lens system

of infinite positive focal plan with plane-wave input maps the far field diffraction pattern of its object onto the focal plane. Therefore, Fraunhofer diffraction determines the limiting performance of physical systems. More generally, at any conjugate ratio, far-field angles are transformed into displacements in the image plane. Fraunhofer diffraction at a circular aperture dictates the fundamental limits of performance of circular lenses. In monochromatic light with a wavelength of λ , the spot size of a circular lens that caused by diffraction is

$$d = 2.44\lambda(f/\#), \quad (2.41)$$

where d is a diameter of the focused spot produced from plane-wave illumination and $f/\#$, called f-number, is the ratio of the focal length of the lens to its clear aperture (effective diameter). The central spot is known as the Airy disc. The formation of Airy disc can be described by considering transverse wave nature. When waves from the secondary source, at the surface of the lens, have the same vibration, their amplitudes are additive. Therefore, we can see as a bright spot. The dark area around the disc occurs because the luminous amplitudes cancel each other out and add up to zero. Basically, the Airy disc is surrounded by a number of much bright rings. Each ring is separated by a circle of zero intensity. This means that the amplitude of vibrations is once again additive. In THz pulses composed of many wavelengths, the pattern of the Airy disc surrounded by rings is difficult to observe. However, decomposition of the pulse might reveal the pattern. To observe the diffraction effect owing to the TPX lens, the electric field images were taken at various delay times and transformed into the frequency domain. In the experiment, one set of the time-dependent data was composed of 200 images with a temporal resolution of 33 fs. The images of single-frequency wave represent a bright disc at higher frequency components. The change of disc size obeys the theoretical prediction, eq.(2.41), namely the disc is smaller when the frequency increases. Experimentally obtained spot sizes on the focal plane could not be compared with the theoretical ones because the optical setup was not proper enough to get a uniform disc, resulting distribution of the THz beam was not uniform as well. However, the evolution of the disc at a fixed frequency along the propagation axis was first observed. Figure 2.28 dictates the propagation dependence of the Airy disc at a frequency of 0.75 THz. In addition, rings surrounding the Airy dish have been clearly observed, particularly near the focal plane. Fourier amplitude images taken at a distance of 10 mm behind the focus are displayed in figure 2.29.

2.8 Conclusions

Broadband property of the THz pulse give rise the significantly difference in focal length and spot size of each frequency component when the pulse is focus. It is similar to the spherical aberration typically encountered by a monochromatic wave in single lenses. It leads to the question how to find the actual focal point of the THz beams. From experimental observations, there are two methods to figure out where the focal position is. One is measuring a focused waveform on the propagation axis. The studies of THz pulse propagation, in section 2.3, show that the waveform at the focus has a highest peak field and a symmetry shape. The other method is observing the formation of the ring. It can be performed by the fixing the observation plane and varying the time delay to peer the formation. It must be symmetry in space and time at the focal plane. In other words, with the same period of time delay from the peak time, the size of ring before the peak time is larger than that observed after the peak time at that a position between the lens and it focal point. Similar to the position far forward from the focal plane, the ring size of the time delay later than the peak time is larger. Practically, the first method is more convenient because we can compare from the numerical peak value. While the second method take more time to find the actual size of the ring. However, it is more suitable for the measurement that requires two-dimensional data, not only the on-axis data. Fortunately, there is an instrument that can detect the intensity of waves in the THz region directly called a bolometer. It is much more convenient method

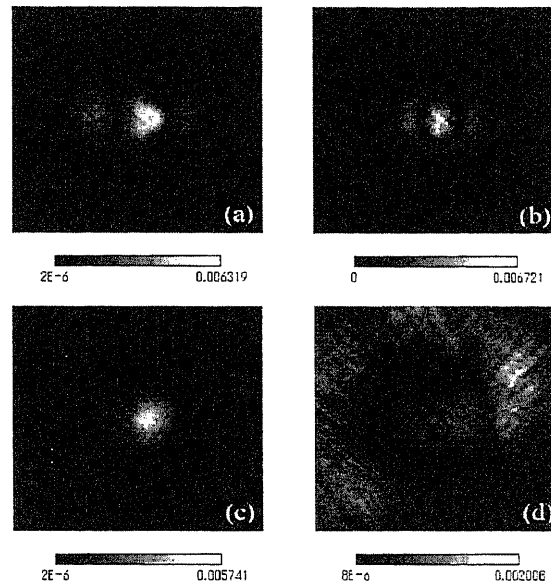


Figure 2.28: Propagation distance dependence of Airy disc at : (a) $z = -10$ mm, (b) $z = 0$ mm (focus), (c) $z = 10$ mm and (d) $z = 30$ mm. The images are taken at a frequency of 0.75 THz.

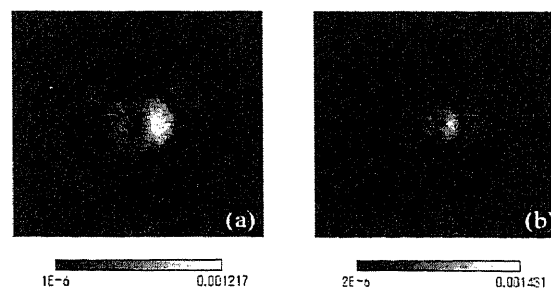


Figure 2.29: Airy disc surrounded by rings of the focus of frequency 1.44 THz (a) and 1.74 THz (b) at distance $z = 10$ mm from the focus.

for finding the focus.

The image of single wavelength, obtained by Fourier transformation of the series of time-dependent imaged, represents well known diffraction limit called Airy disc as well as rings surrounding it. This limits the size of interesting object when the image is analyzed in the frequency domain. The greater detail has been described in section 4.4.

The time-domain spectroscopy of TPX has been performed in the low-frequency region, yielding the frequency dependence of absorption and a constant refractive index. The results of this experiment are necessary factors for designing a TPX lens in the imaging system of a large THz beam. The performance of the TPX lens used in the imaging was described. The diffraction limit of each frequency is different. Therefore, the vision in frequency domain relies on the dimension of the object of interest.

Chapter 3

Terahertz Electric Field Detection

This chapter describes how to measure THz electric field. We have used the electro-optic sampling method to detect a THz waveform. This method is the only one that can be applied to observe the spatial profile of the THz beam. The electro-optic effect of nonlinear crystal, especially ZnTe crystal is explained. The THz waveforms were observed using the electro-optic balance detection method as explained in section 3.2. The last section explains two-dimensional field detection which was used for THz imaging.

3.1 Introduction

A few methods have been proposed for detecting THz radiation. The detector that measures THz intensity directly is a bolometer. There are two methods to measure the THz electric field. One is the reverse process of photoconductive antenna, which called photoconductive sensor. When a THz beam radiates on a semiconductor surface, it drives free carriers generated by an optical probe beam. The THz field is provided by detecting the change of current. This technique is usually operated with a photoconductive antenna. The optical configuration of the system, using the photoconductive switching for emission and radiation, is typically symmetrical. In other words, the position of detector is equivalent to that of the emitter. It is therefore suitable for studying the generation mechanism. The disadvantage of the photoconductive sensor is that it typically requires micro-fabrication techniques to make small-gap electrodes on semiconductors. The other method is electro-optic detection. We used this method to measure the THz field in experiments. The outstanding advantage of this method is that can be modified to conduct two-dimensional THz imaging. The detection mechanism is described in detail as follows.

Electro-optic detection is a second-order nonlinear optical process in which an applied electric field induces a refractive-index change in an electro-optic material. The refractive-index change is proportional to the applied field (Pockels effect). It affects the ellipticity of a circularly polarized probe pulse that is co-propagating through the same material. The change of ellipticity is measured with a polarizing beam splitter that separates the two orthogonal polarizations of the probe beam. A balance photodetector measures the intensity difference between the two components and gives a signal that is directly proportional to the electric field. By varying the delay between the THz pulse and the probe pulse, one obtains the complete time-dependent electric field. The EO detection is emerging as the most popular choice for THz detection. There are two reasons for this: First, the signal to noise ratio is high. Second, electro-optic detection is suitable for signals with a large bandwidth (up to 70 THz [48]). For the EO detection, zinc-blend crystals such as ZnTe and GaP are often used. ZnTe is very suitable because its refractive index in the far-IR is comparable to the near-IR refractive index, resulting in relatively efficient THz detection. The other kind of EO crystal such as LiTaO₃ and LiNbO₃ can also be used for THz detection, but there is a severe the group velocity mismatch

between the THz pulse and the probe pulse in these crystals. This problem is reduced to a small amount in ZnTe, resulting in a significantly improved time resolution [49].

We describe the measurement of THz electric field using the EO balance detection. In this research, ZnTe is used as electro-optic crystal that expresses the linear electro-optic effect while a THz pulse is passing. The effect of the electric field on the propagation is most conveniently given by the changes in the constants $1/n_x^2$, $1/n_y^2$, $1/n_z^2$ of the index ellipsoid,

$$\frac{x^2}{n_x^2} + \frac{y^2}{n_y^2} + \frac{z^2}{n_z^2} = 1, \quad (3.1)$$

where the direction x , y , and z are the major axes of ellipsoid. The equation of the index ellipsoid in the presence of electric field can be expressed as follows,

$$\left(\frac{1}{n^2}\right)_1 x^2 + \left(\frac{1}{n^2}\right)_2 y^2 + \left(\frac{1}{n^2}\right)_3 z^2 + 2\left(\frac{1}{n^2}\right)_4 yz + 2\left(\frac{1}{n^2}\right)_5 xz + 2\left(\frac{1}{n^2}\right)_6 xy = 1, \quad (3.2)$$

where $\left(\frac{1}{n^2}\right)_1 = \frac{1}{n_x^2}$, $\left(\frac{1}{n^2}\right)_2 = \frac{1}{n_y^2}$, and $\left(\frac{1}{n^2}\right)_3 = \frac{1}{n_z^2}$ in the case of no applied field. The linear change in the coefficients $\left(\frac{1}{n^2}\right)_i$, $i = 1, \dots, 6$ due to an arbitrary electric field $\mathbf{E}(E_x, E_y, E_z)$ is defined by

$$\Delta\left(\frac{1}{n^2}\right)_i = \sum_{j=1}^3 r_{ij} E_j. \quad (3.3)$$

For the crystals of the zinc blend class as ZnTe (point group symmetry of $\bar{4}3m$), the change of coefficients $\left(\frac{1}{n^2}\right)_i$ can be written as [35],

$$\begin{bmatrix} \Delta\left(\frac{1}{n^2}\right)_1 \\ \Delta\left(\frac{1}{n^2}\right)_2 \\ \Delta\left(\frac{1}{n^2}\right)_3 \\ \Delta\left(\frac{1}{n^2}\right)_4 \\ \Delta\left(\frac{1}{n^2}\right)_5 \\ \Delta\left(\frac{1}{n^2}\right)_6 \end{bmatrix} = \begin{bmatrix} 0 & 0 & 0 \\ 0 & 0 & 0 \\ 0 & 0 & 0 \\ r_{41} & 0 & 0 \\ 0 & r_{41} & 0 \\ 0 & 0 & r_{41} \end{bmatrix} \begin{bmatrix} E_x \\ E_y \\ E_z \end{bmatrix}, \quad (3.4)$$

where r_{41} is the element of electro-optic tensor. Using eq. (3.2), we obtain the equation of the index ellipsoid in the presence of the field $\mathbf{E}(E_x, E_y, E_z)$ as

$$\left(\frac{1}{n_o^2}\right)_1 x^2 + \left(\frac{1}{n_o^2}\right)_2 y^2 + \left(\frac{1}{n_o^2}\right)_3 z^2 + 2r_{41} E_x yz + 2r_{41} E_y xz + 2r_{41} E_z xy = 1. \quad (3.5)$$

Since the ZnTe is an isotropic crystal, the constants involved in the first three terms do not depend on the field. They are taken as $n_x = n_y = n_z = n_o$. The remainders are mixed terms, i.e., yz , xz and xy . This means that the major axes of the ellipsoid, with the applied field, are no longer parallel to the x , y , and z axes of the

crystal. It becomes, then, necessary to find the directions of the new axes in which we can determine the effect of electromagnetic field on the propagation of the probe pulse. We now consider the problem of finding a new coordinate system $-x', y', z'$ in which the equation of ellipsoid (3.5) contains no mixed terms. That is

$$\frac{x'^2}{n_{x'}^2} + \frac{y'^2}{n_{y'}^2} + \frac{z'^2}{n_{z'}^2} = 1, \quad (3.6)$$

where x', y' and z' are the directions of the major axes of the ellipsoid in the presence of an external field. Equation 3.5 can be expressed in the quadratic form

$$S_{ij}x_i x_j = 1, \quad (3.7)$$

so that

$$S_{ij} = \begin{bmatrix} \left(\frac{1}{n^2}\right)_1 & \left(\frac{1}{n^2}\right)_6 & \left(\frac{1}{n^2}\right)_5 \\ \left(\frac{1}{n^2}\right)_6 & \left(\frac{1}{n^2}\right)_2 & \left(\frac{1}{n^2}\right)_4 \\ \left(\frac{1}{n^2}\right)_5 & \left(\frac{1}{n^2}\right)_4 & \left(\frac{1}{n^2}\right)_3 \end{bmatrix}. \quad (3.8)$$

If the vector from the origin to a point (x_1, x_2, x_3) on the ellipsoid (3.7) is denoted by $\mathbf{x}(x_1, x_2, x_3)$, then the vector \mathbf{N} with components

$$N_i = S_{ij}x_j \quad (3.9)$$

is normal to the ellipsoid at \mathbf{R} . We next apply the last result to determine the directions and magnitudes of the principle axes of the ellipsoid (3.7). Since the principle axes are normal to the surface, we can determine their points of intersection (x_1, x_2, x_3) with the ellipsoid by requiring that at such points the radius vector be parallel to the normal, that is,

$$S_{ij}x_j = Sx_i, \quad (3.10)$$

where S is a constant independent of i . Writing out eq.(3.10) in component form for $i = 1, 2, 3$ gives

$$\begin{aligned} (S_{11} - S)x_1 + S_{12}x_2 + S_{13}x_3 &= 0 \\ S_{21}x_1 + (S_{22} - S)x_2 + S_{23}x_3 &= 0 \\ S_{31}x_1 + S_{32}x_2 + (S_{33} - S)x_3 &= 0. \end{aligned} \quad (3.11)$$

These are homogeneous equations for the unknowns x_1, x_2 , and x_3 . A nontrivial solution exists when the determinant of the coefficients vanish, that is,

$$\det[S_{ij} - S\delta_{ij}] = 0. \quad (3.12)$$

The set of $S', S'',$ and S''' is the eigenvalue of the matrix \mathbf{S} , while the vectors $\mathbf{X}', \mathbf{X}''$ and \mathbf{X}''' are their eigenvectors. If we express the equation of the index ellipsoid in the new coordinate system whose axes are parallel to $\mathbf{X}', \mathbf{X}''$, and \mathbf{X}''' , it becomes

$$S'x'^2 + S''y'^2 + S'''z'^2 = 1, \quad (3.13)$$

where the unit vectors \mathbf{x}', \mathbf{y}' , and \mathbf{z}' are taken as parallel to $\mathbf{X}', \mathbf{X}''$, and \mathbf{X}''' , respectively.

3.2 Electro-optic balance detection

3.2.1 Electro-optic crystal

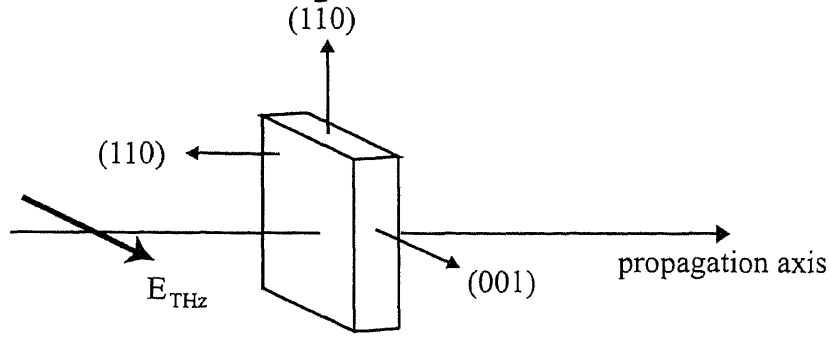


Figure 3.1: Orientation of the ZnTe crystal used for waveform detection.

We used the electro-optic balance method for detecting a THz waveform on the propagation axis. The probe beam was focused with a glass lens with a focal length of 300 mm into the center of the THz beam on the EO crystal. Therefore, only a small portion of the THz beam, which is comparable to the size of focused probe beam, was detected. The THz electric field was applied in the (001) direction as shown in figure 3.1, the Jones vector of the field is

$$\mathbf{E}_{\text{THz}} = \begin{bmatrix} 0 \\ 0 \\ 1 \end{bmatrix} E_{\text{THz}}. \quad (3.14)$$

Equation (3.5) becomes thus

$$\frac{x^2 + y^2 + x^2}{n_o^2} + 2r_{41}E_{\text{THz}}xy = 1. \quad (3.15)$$

Consequently, S_{ij} can be written as

$$S_{ij} = \begin{bmatrix} \frac{1}{n_o^2} & r_{41}E_{\text{THz}} & 0 \\ r_{41}E_{\text{THz}} & \frac{1}{n_o^2} & 0 \\ 0 & 0 & \frac{1}{n_o^2} \end{bmatrix}. \quad (3.16)$$

According to eq. (3.12), the eigenvalues can be calculated from

$$\begin{vmatrix} \frac{1}{n_o^2} - S & r_{41}E_{\text{THz}} & 0 \\ r_{41}E_{\text{THz}} & \frac{1}{n_o^2} - S & 0 \\ 0 & 0 & \frac{1}{n_o^2} - S \end{vmatrix} = 0. \quad (3.17)$$

It gives

$$\begin{aligned} S' &= \frac{1}{n_o^2} \\ S'' &= \frac{1}{n_o^2} + r_{41}E_{\text{THz}} \end{aligned}$$

$$S''' = \frac{1}{n_o^2} - r_{41}E_{\text{THz}}. \quad (3.18)$$

Their eigenvectors are given in terms of crystal axes as

$$\begin{aligned} \mathbf{X}' &= \mathbf{z} \\ \mathbf{X}'' &= \mathbf{x} + \mathbf{y} \\ \mathbf{X}''' &= \mathbf{x} - \mathbf{y}. \end{aligned} \quad (3.19)$$

It is clear from eq.(3.19) that in order to put the equation in a diagonal form we need to choose a coordinate system x' , y' , z' where z' is parallel to z . The other axes are related to the x and y axis by a 45° rotation. The index of refraction for the new coordinate are then written as

$$\begin{aligned} \frac{1}{n_{x'}^2} &= \frac{1}{n_o^2} - r_{41}E_{\text{THz}}, \\ \frac{1}{n_{y'}^2} &= \frac{1}{n_o^2} + r_{41}E_{\text{THz}}, \\ \frac{1}{n_{z'}^2} &= \frac{1}{n_o^2}. \end{aligned} \quad (3.20)$$

Equation (3.15) in the new coordinate is

$$\left(\frac{1}{n_o^2} - r_{41}E_{\text{THz}} \right) x'^2 + \left(\frac{1}{n_o^2} + r_{41}E_{\text{THz}} \right) y'^2 + \frac{1}{n_o^2} z'^2 = 1 \quad (3.21)$$

The length of x' -axis is $2n_{x'}$. By assuming $r_{41}E \ll n_o^2$, we obtain

$$\begin{aligned} n_{x'} &= n_o \sqrt{1 - n_o^2 r_{41} E_{\text{THz}}} \\ &= n_o + \frac{n_o^3}{2} r_{41} E_{\text{THz}}, \end{aligned} \quad (3.22)$$

and, similarly,

$$\begin{aligned} n_{y'} &= n_o - \frac{n_o^3}{2} r_{41} E_{\text{THz}}, \\ n_{z'} &= n_o. \end{aligned} \quad (3.23)$$

According to eq.(3.19), the horizontal and vertical directions in the laboratory frame are z' and x' , respectively. Figure 3.2(c) depicts the direction of these components. We now consider that the horizontal and vertical directions in the laboratory frame are x - and y -axes as shown in figure 3.2(c). When the probe light of the linear polarization at 45° to either principle axes propagates in the ZnTe crystal applied by the z' -polarized THz field, the components of the light along the horizontal gains the phase retardation, θ , over the distance L compared to the vertical by

$$\begin{aligned} \theta &= \theta_{z'} - \theta_{x'} \\ &= \frac{\omega}{c} \Delta n L \\ &= \frac{\omega}{c} |n_{z'} - n_{x'}| L \end{aligned}$$

$$\begin{aligned}
 &= \frac{\omega}{c} \frac{n_o^3}{2} r_{41} E_{\text{THz}} \\
 &= \left(\frac{\pi n_o^3 r_{41} L}{\lambda} \right) E_{\text{THz}}.
 \end{aligned}
 \tag{3.24}$$

Therefore, we can measure the THz field, E_{THz} , by detecting the phase retardation between the two components of the probe pulse having a wavelength λ . The detector part was composed of a linear polarizer, a ZnTe crystal, a quarter-wave plate, a Wollaston prism, and balance photodiodes as shown in figure 3.2. The quarter-wave plate was adjusted so that the optic axis aligns along the principle axes of the laboratory frame. Hence, circularly polarized light is produced by passing linearly polarized light through the quarter-wave plate at an angle of 45° to the optic axis of the plate as shown in figure 3.2(a). In fact, when the polarized light passes through the ZnTe crystal, it is slightly modulated by the intrinsic birefringence in the crystal. However, by re-adjusting the optic axis of the quarter-wave plate, the polarization state on the probe light before going through the Wollaston prism is completely circular. The Wollaston prism, which is actually a polarizing beam-splitter, separates the beam into orthogonal polarization components. At the end, the difference in intensity ΔI between two components, i.e. x'' and y'' in figure 3.2(c), was detected by a differential photodiodes. The signal from the diodes was sent to a lock-in amplifier that was synchronized with an optical chopper placed in the pump beam path. The amplified signal was recorded by a PC. The signal is zero in the absence of the THz field because the intensity of the x' and y' components are the same shown in figure 3.2(b). When THz electric field perturbs the crystal simultaneously with the probe pulse, the refractive index of the crystal is altered via the electro-optic effect. Consequently, the linearly polarized optical probe will be modulated by the THz field. The polarization of the transmitted beam is then changed to be elliptic as illustrated in figure 3.2(b). When this light passes through the Wollaston prism, the intensity of x'' and y'' components are different. Varying the time delay between the probe pulse and the THz pulse, it allows scanning the whole THz pulse.

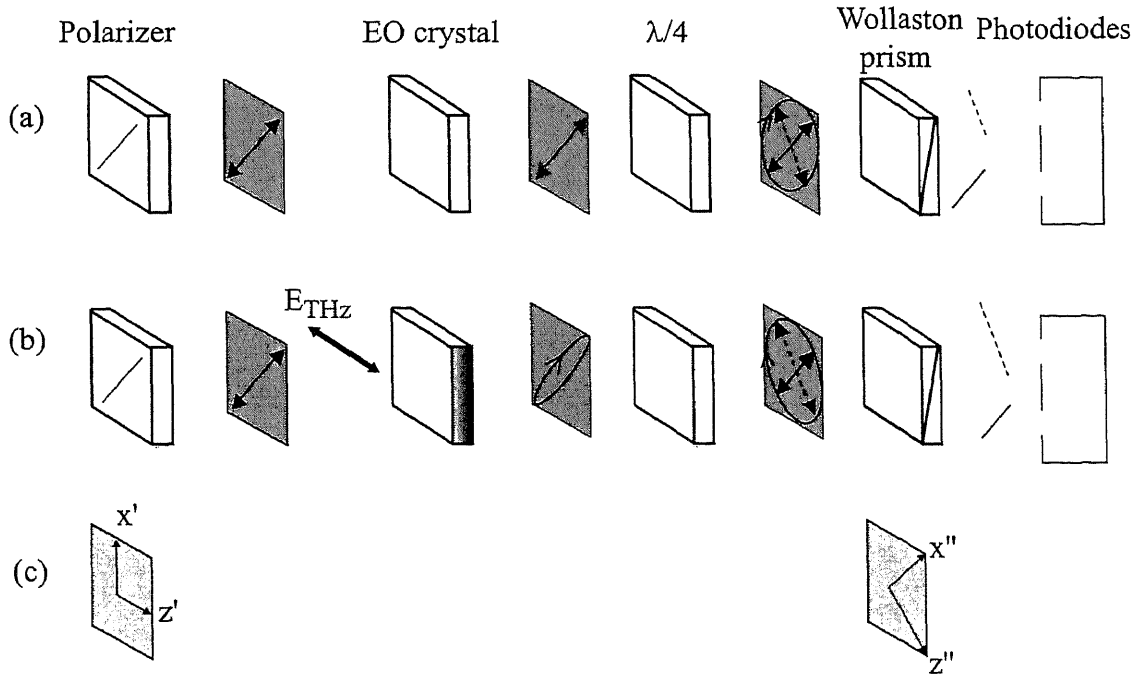


Figure 3.2: Optical components of electro-optic balance detection in the absence (a) and the presence of THz field (b). The principle axes of the polarization frame depicts in (c).

3.2.2 Polarization state of probe pulses

We describe how the THz field is expressed in term of signal detected by the differential photodiodes using Jones vectors and matrices as follows.

1. The horizontal polarized probe beam is represented by

$$\mathbf{E}_{\text{in}} = \begin{bmatrix} 1 \\ 0 \end{bmatrix} E_0. \quad (3.25)$$

2. The light was then passed through a linear polarizer which oriented at 45° to the x'' and y'' axes, as shown in figure 3.2(a) and (b). The transmission matrix of the polarizer is

$$\mathbf{T}_p = \begin{bmatrix} \cos \frac{\pi}{4} & \sin \frac{\pi}{4} \\ -\sin \frac{\pi}{4} & \cos \frac{\pi}{4} \end{bmatrix}. \quad (3.26)$$

3. The transmission matrix of the EO crystal which has the phase retardation θ between the x'' and z'' axes is

$$\mathbf{T}_{\text{eo}} = \begin{bmatrix} e^{i\theta/2} & 0 \\ 0 & e^{-i\theta/2} \end{bmatrix}. \quad (3.27)$$

4. The quarter-wave plated which the major axes are parallel to the x'' and z'' direction is represented by the

$$\mathbf{T}_{\lambda/4} = \begin{bmatrix} e^{i\pi/4} & 0 \\ 0 & e^{-i\pi/4} \end{bmatrix}. \quad (3.28)$$

5. The probe light was passed through a linear analyzer that crossed to the polarizer. The matrix represent the analyzer is thus

$$\mathbf{T}_a = \begin{bmatrix} \cos \frac{\pi}{4} & -\sin \frac{\pi}{4} \\ \sin \frac{\pi}{4} & \cos \frac{\pi}{4} \end{bmatrix}. \quad (3.29)$$

The electric field along the x'' and z'' axes is given by

$$\mathbf{E}_{\text{out}} = \mathbf{T}_a \mathbf{T}_{\text{eo}} \mathbf{T}_p \mathbf{E}_{\text{in}}. \quad (3.30)$$

The intensities of the prime components are

$$\begin{bmatrix} I_{x''} \\ I_{z''} \end{bmatrix} = \begin{bmatrix} \cos^2 \frac{1}{2}(\theta + \frac{\pi}{2}) \\ \sin^2 \frac{1}{2}(\theta + \frac{\pi}{2}) \end{bmatrix} E_0^2. \quad (3.31)$$

The difference of intensity that the photodiodes detect is

$$\Delta I = I_{x''} - I_{z''} = I_0 \sin \theta, \quad (3.32)$$

where $I_0 = E_0^2$. From the section 3.1, THz field can be calculated from eq. (3.24) as

$$E_{\text{THz}} = \frac{\lambda}{\pi n_o^3 r_{41} L} \theta. \quad (3.33)$$

Substituting θ in eq. (3.32) to eq. (3.33), the magnitude of THz electric field is expressed in term of the probe intensity I_0 and the different intensity ΔI as

$$E_{\text{THz}} = \frac{\lambda}{\pi n_o^3 r_{41} L} \sin^{-1} \left(\frac{\Delta I}{I_0} \right). \quad (3.34)$$

In our experiments, for example, the wavelength of probe light is 800 nm, the refractive index of ZnTe is 2.83, r_{41} [35] is 3.9×10^{-12} m/V, the length of ZnTe is 1 mm, the magnitude of THz is simply as

$$E_{\text{THz}} = 27.5 \sin^{-1} \left(\frac{\Delta I}{I_0} \right). \quad (3.35)$$

It should be note that, in the experiment, the probe intensity is measured $I_{0,\text{mea}}$ by using one of the diodes. Therefore, the field is given

$$E_{\text{THz}} = 27.5 \sin^{-1} \left(\frac{\Delta I}{2I_{0,\text{mea}}} \right). \quad (3.36)$$

3.3 Two-dimensional electric field detection

3.3.1 Electro-optic crystal

In previous section, the detection of an axial THz field was described. We now consider the measurement of THz field distribution on a plane which is perpendicular to the propagation direction. The principle of detection is similar to the previous method, namely, the electro-optic effect. The differences are: (1) the probe beam was expanded so that it covers the THz beam that radiates on the EO crystal, (2) the THz field was applied in the $(1\bar{1}0)$ direction and (3) the signal was collected by a CCD camera instead of the differential photodiodes. The

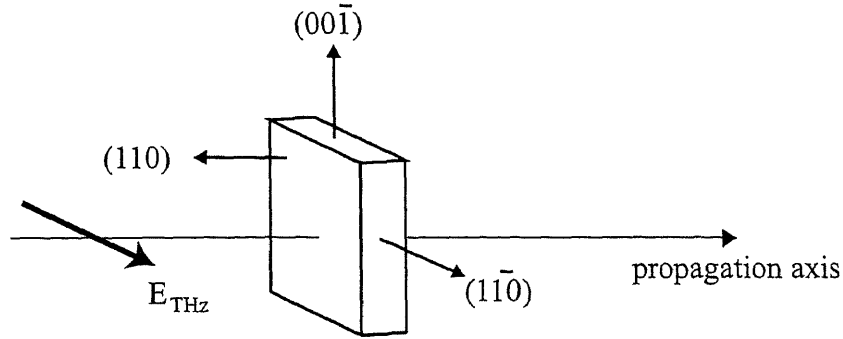


Figure 3.3: Orientation of the ZnTe crystal used for two-dimensional electric field detection.

THz field is written in a vector form as

$$\mathbf{E}_{\text{THz}} = \frac{1}{\sqrt{2}} \begin{bmatrix} 1 \\ -1 \\ 0 \end{bmatrix} E_{\text{THz}} \quad (3.37)$$

Substituting E_{THz} into eq. (3.5) yields

$$\left(\frac{1}{n_o^2}\right)x^2 + \left(\frac{1}{n_o^2}\right)y^2 + \left(\frac{1}{n_o^2}\right)z^2 + \sqrt{2}r_{41}E_{\text{THz}}yz - \sqrt{2}r_{41}E_{\text{THz}}xz = 1. \quad (3.38)$$

The matrix S_{ij} becomes

$$S_{ij} = \begin{bmatrix} \frac{1}{n_o^2} & 0 & -\frac{1}{\sqrt{2}}r_{41}E_{\text{THz}} \\ 0 & \frac{1}{n_o^2} & \frac{1}{\sqrt{2}}r_{41}E_{\text{THz}} \\ -\frac{1}{\sqrt{2}}r_{41}E & \frac{1}{\sqrt{2}}r_{41}E_{\text{THz}} & \frac{1}{n_o^2} \end{bmatrix} \quad (3.39)$$

The eigenfunctions and the eigenvalues of S_{ij} can be calculated from $\det[S_{ij} - S\delta_{ij}] = 0$:

$$\det \begin{vmatrix} \frac{1}{n_o^2} - S & 0 & -\frac{1}{\sqrt{2}}r_{41}E_{\text{THz}} \\ 0 & \frac{1}{n_o^2} - S & \frac{1}{\sqrt{2}}r_{41}E_{\text{THz}} \\ -\frac{1}{\sqrt{2}}r_{41}E_{\text{THz}} & \frac{1}{\sqrt{2}}r_{41}E & \frac{1}{n_o^2} - S \end{vmatrix} = 0 \quad (3.40)$$

This gives the eigenvalues as follows:

$$\begin{aligned} S' &= \frac{1}{n_o^2} \\ S'' &= \frac{1}{n_o^2} + r_{41}E_{\text{THz}} \\ S''' &= \frac{1}{n_o^2} - r_{41}E_{\text{THz}} \end{aligned} \quad (3.41)$$

The corresponding eigenvectors are

$$\begin{aligned} \mathbf{X}' &= \mathbf{x} + \mathbf{y} \\ \mathbf{X}'' &= -\frac{1}{\sqrt{2}}\mathbf{x} + \frac{1}{\sqrt{2}}\mathbf{y} + \mathbf{z} \\ \mathbf{X}''' &= \frac{1}{\sqrt{2}}\mathbf{x} - \frac{1}{\sqrt{2}}\mathbf{y} + \mathbf{z}, \end{aligned} \quad (3.42)$$

where (x, y, z) is the old coordinate system. The indexes of refractive in the new coordinate system are

$$\begin{aligned} \frac{1}{n_{x'}^2} &= \frac{1}{n_o^2} - r_{41}E_{\text{THz}} \\ \frac{1}{n_{y'}^2} &= \frac{1}{n_o^2} + r_{41}E_{\text{THz}} \\ \frac{1}{n_{z'}^2} &= \frac{1}{n_o^2} \end{aligned} \quad (3.43)$$

The ellipsoid equation becomes

$$\left(\frac{1}{n_o^2} - r_{41}E_{\text{THz}}\right)x'^2 + \left(\frac{1}{n_o^2} + r_{41}E_{\text{THz}}\right)y'^2 + \frac{1}{n_o^2}z'^2 = 1. \quad (3.44)$$

The following method describes how to measure the electric field in two dimensions. Usually when

obtaining a two-dimensional image, a CCD has been used for real time imaging. Up to now, there is no literature presenting a multi-channel lock-in amplifier for CCD signal. The S/N ratio should be considered when using a CCD camera. According to the change of polarization when THz field is applied to an EO crystal, THz intensity profile can be measured using a polarizer and an analyzer with an EO crystal placed between them. But phase information cannot be obtained by this method. We applied the field-linear detection method of nonlinear optical signal using the polarization change of the probe light. This method is called an optical heterodyne detection method (OHD). It was introduced by Eesley and Levenson [50,51]. They used the method for measurements of the Raman-induced Kerr effect. Jiang *et al.* introduced this technique to THz field detection using the EO sampling method and derived the optimal bias point under the existence of background light [38]. However, the technique had not been applied to detect the THz field in two dimensions. Two-dimensional field detection is described as follows.

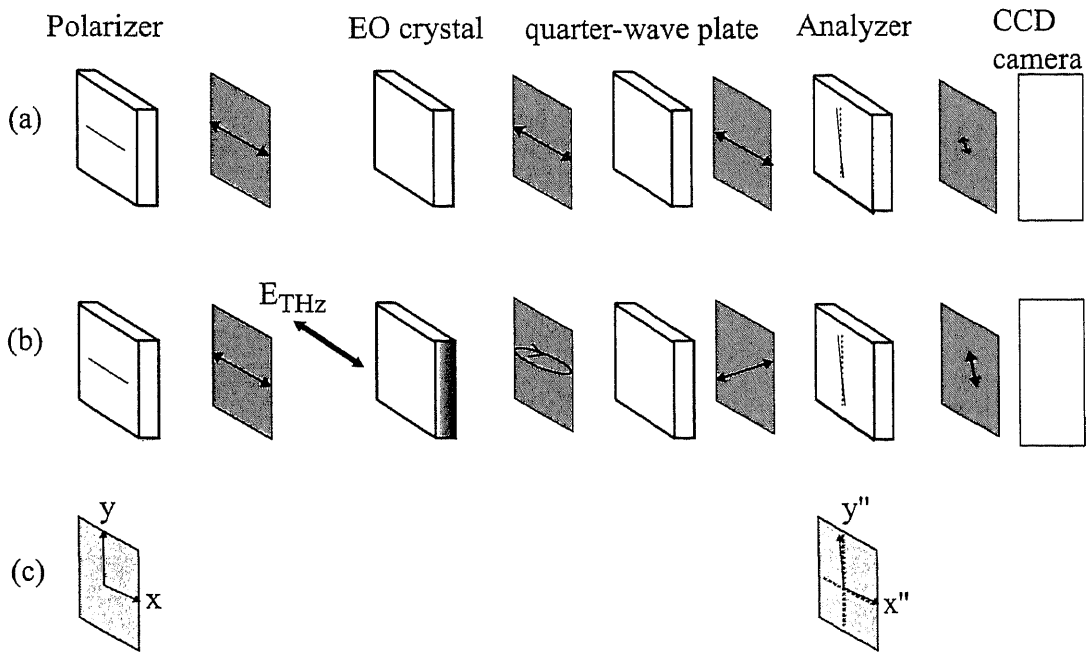


Figure 3.4: Optical components of two-dimensional field detection in the absence (a) and the presence of THz field (b). The principle axes of the polarization frame depicts in (c).

The schematic of optical components for detecting the THz field distribution is shown in figure (3.4). The input laser beam was linearly polarized in horizontal direction. It was reflected at a pellicle beam splitter and sent to collinear with the THz beam. We adopted a quarter-wave plate as a compensator. It was placed between the EO crystal and an analyzer. Without using a quarter-wave plate, the field-linear THz wave detection has been reported [5]. However, the local oscillation originates from the polarization rotation of the probe light due to the small birefringence in the EO crystal cannot be optimized in a controlled manner. Using the quarter-wave plate, the local oscillation can be controlled in that the modulation in the EO is optimized. We adjusted the fast axis of the quarter-wave plate to be parallel to the incident light polarization.

3.3.2 Polarization state of probe pulses

The optical configuration of the phase-sensitive electro-optic detection will be describing. The principle coordinate is chosen to be collinear with the laboratory frame so that the x , y and z axes align along the horizontal, vertical and propagation directions, respectively. Jones vectors and matrices represent the polarization state of the probe light as follows.

1. The input probe beam is linearly polarized along the x axis; namely, the polarization is in the $(\bar{1}\bar{1}0)$ direction of the EO crystal. We represent the input field by a column vector

$$\mathbf{E}_{\text{in}} = \begin{bmatrix} 1 \\ 0 \end{bmatrix} E_0. \quad (3.45)$$

2. When the probe light passes through the EO crystal, the electric field components along the $(\bar{1}\bar{1}0)$ and $(\bar{1}\bar{1}0)$ directions are modulated with phase retardation 2θ due to the presence of a THz field along the x axis. Assuming $\mathbf{R}(\psi)$ is the rotation matrix, which rotates the coordinates x, y to the new coordinates x', y' by an angle ψ about the z axis, the transmission matrix of the crystal is

$$\begin{aligned} \mathbf{T}_{\text{eo}} &= \mathbf{R}^{-1}\left(-\frac{\pi}{4}\right) \mathbf{T}_{\text{eo}}^{(0)} \mathbf{R}\left(-\frac{\pi}{4}\right) \\ &= \begin{bmatrix} \cos \frac{\pi}{4} & \sin \frac{\pi}{4} \\ -\sin \frac{\pi}{4} & \cos \frac{\pi}{4} \end{bmatrix} \begin{bmatrix} e^{i\theta} & 0 \\ 0 & e^{-i\theta} \end{bmatrix} \begin{bmatrix} \cos \frac{\pi}{4} & -\sin \frac{\pi}{4} \\ \sin \frac{\pi}{4} & \cos \frac{\pi}{4} \end{bmatrix} \\ &= \begin{bmatrix} \cos \theta & -i \sin \theta \\ -i \sin \theta & \cos \theta \end{bmatrix}. \end{aligned} \quad (3.46)$$

Here, $\mathbf{T}_{\text{eo}}^{(0)}$ is the Jones matrix of the EO crystal in the frame along its optical axes.

3. The transmitted beam passes through a quarter-wave plate whose fast axis is adjusted to be parallel to the x axis. Therefore, its transmission matrix is

$$\mathbf{T}_{\lambda/4} = \begin{bmatrix} e^{i\pi/4} & 0 \\ 0 & e^{-i\pi/4} \end{bmatrix}. \quad (3.47)$$

4. The probe light is then transmitted through a linear analyzer that is rotated by the angle δ from the y axis. The Jones matrix of the analyzer becomes

$$\begin{aligned} \mathbf{T}_{\text{a}} &= \mathbf{R}^{-1}(\delta) \mathbf{T}_{\text{a}}^{(0)} \mathbf{R}(\delta) \\ &= \begin{bmatrix} \cos \delta & -\sin \delta \\ \sin \delta & \cos \delta \end{bmatrix} \begin{bmatrix} 0 & 0 \\ 0 & 1 \end{bmatrix} \begin{bmatrix} \cos \delta & \sin \delta \\ -\sin \delta & \cos \delta \end{bmatrix} \\ &= \begin{bmatrix} \sin^2 \delta & -\sin \delta \cos \delta \\ -\sin \delta \cos \delta & \cos^2 \delta \end{bmatrix}. \end{aligned} \quad (3.48)$$

Therefore, the output probe field is described by

$$\begin{aligned} \mathbf{E} &= \begin{bmatrix} E_x \\ E_y \end{bmatrix} \\ &= \mathbf{T}_{\text{a}} \mathbf{T}_{\lambda/4} \mathbf{T}_{\text{eo}} \mathbf{E}_{\text{in}}. \end{aligned} \quad (3.49)$$

The CCD camera detects the output intensity

$$I = |E_x|^2 + |E_y|^2. \quad (3.50)$$

By substituting the transmission matrices and the vector into eq. (3.49), we obtain

$$I = I_0 \sin^2(\delta + \theta), \quad (3.51)$$

where $I_0 = E_0^2$. If we consider the scattered light in the EO crystal, ηI_0 , and assume that $|\delta|$ and $|\theta|$ are small, eq. (3.51) becomes

$$I = I_0[\eta + (\delta + \theta)^2]. \quad (3.52)$$

Substituting $I_b = I_0(\eta + \delta^2)$ in eq. (3.52), we get

$$I - I_b = I_0(2\delta\theta + \theta^2). \quad (3.53)$$

Therefore, the phase retardation θ in the crystal is

$$\theta = -\delta \pm \sqrt{\delta^2 + \frac{I - I_b}{I_0}}. \quad (3.54)$$

Since θ should be small when $I - I_b$ is small, we have to pick up only the positive sign in eq. (3.54). The THz field, E_{THz} , is related to the phase retardation, θ , by

$$E_{\text{THz}} = \frac{\lambda}{\pi n_o^3 r_{41} L} \theta. \quad (3.55)$$

The magnitude of the small angle δ that optimizes the modulation in the EO crystal was determined by the modulation depth as [38]

$$\gamma = \frac{I_{\theta \neq 0} - I_{\theta = 0}}{I_{\theta \neq 0} + I_{\theta = 0}}. \quad (3.56)$$

In our system, the angle δ was found to be 0.02 degree [52].

3.4 Conclusions

The electro-optic detection was used to measure the THz field. The electro-optic media was a ZnTe crystal. THz field detection was conducted in two modes; (1) one dimensional THz field on the propagation axis or the axial THz field waveform and (2) two-dimensional THz field or the spatial field distribution on the plane that is perpendicular to the propagation axis. The axial field was measured by focusing the probe beam to the center of the THz beam and using the balance detection technique. The spatial distribution of THz field was mapped by the expanded probe beam at the EO surface and captured by a CCD camera. The direction of THz field applied to the crystal was not the same in the two detection modes. However, by varying the delay time between the THz pulse and the probe pulse, the temporal waveform can be obtained independently from the detection mode.

Chapter 4

Electric Field Imaging

4.1 Introduction

THz radiation from the large-aperture photoconductive antenna was used to image objects by detecting electric field distribution. From section 2.4 we know that the distribution of the THz beam varies over by time and space. When the THz beam is used to image an object in question, it is necessary to know the effect on the image of the object. There is one previous study that uses the same THz source even through the size of the emitter are different [34]. They imaged objects by detecting the intensity profile. In their experiments, the time delay between the THz pulse and the probe was fixed. Optimization of the time delay to obtain the best image quality however, has not been investigated. The optimized timing is the important factor in a fixed-time delay mode. The advantage of this mode is that enables *in situ* studies of dynamic processes or high-speed single-time events at a high frame rate [53]. In the present imaging, the distribution of THz electric field, not the intensity, was detected. Therefore, it is able to be analyzed in the frequency domain. Frequency-resolved images can in general yield better resolution although their acquisition time should be much longer than that for the fixed-time image. By scanning the delay time and Fourier transforming the temporal waveforms of the THz field at each position, frequency-resolved images can be obtained.

This chapter shows the results of two experiments concerning the use of intense half-cycle THz pulses from a large-aperture antenna in imaging; delay-time optimization and frequency-resolved imaging. Phase-sensitive detection technique [36, 38] was used to detect the electric field image of a metal object in a transmission mode. Digital processing was introduced to eliminate the artifacts from a non-uniform THz beam profile. This chapter introduces how to improve the resolution of the THz image by considering the extinguishing of low-frequency components. Two experiments were performed; (1) replacing the photoconductive material by a low-temperature grown GaAs wafer in steady of a semi-insulation GaAs wafer and (2) using filtering low-frequency components by hexagonal closed pack circular hole array.

4.2 Imaging system

Figure 4.1 illustrates the experimental setup. The optical source was a regeneratively amplified Ti:sapphire laser with a 150 fs pulse width, 800 nm central wavelength, and a 1 kHz repetition rate. The laser beam was divided into a major intensity portion for the pump beam and a minor portion for the probe beam. The pump beam was spatially expanded and illuminated a large-aperture photoconductive antenna, composed of a semi-insulating GaAs wafer and two aluminum electrodes with a 3-cm intergap spacing. A pulsed high bias voltage was applied to the wafer through the electrodes. The pump pulses created carriers in the intergap area, leading to the generation of THz radiation. In this study, the pump pulse energy and the bias voltage were

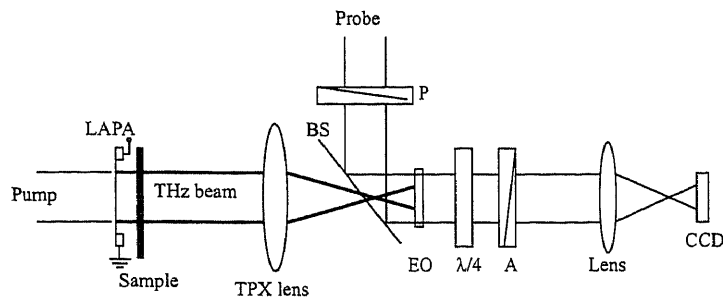


Figure 4.1: Schematic of experimental setup for two-dimensional electric field detection. LAPA: large-aperture photoconductive antenna, EO: electro-optic crystal (ZnTe), $\lambda/4$: quarter-wave plate, P: polarizer, A: polarization analyzer.

500 μJ and 5 kV, respectively. The THz beam emitted from the photoconductive antenna passed through a sample object and a lens made of TPX polymer. The TPX lens and an EO crystal were placed so that the 3 : 2 image of the object was formed on the EO crystal. The focal length of the lens was $f=98.3$ mm and its diameter was 80 mm. The object and its image position were set at $z = -5f/2$ and $z = 5f/3$, when the lens was placed at $z = 0$.

The spatial distribution of the refractive index modulation in the EO crystal, which is proportional to the THz electric field, was mapped by the probe optical pulses onto a CCD camera. By generating a local oscillator field using a quarter-wave plate, we detected the 2D field image with high sensitivity. The probe beam went through a delay line and was linearly polarized in the horizontal direction. The beam was then expanded and led to the EO crystal by a pellicle beam splitter. A 1-mm-thick $\langle 110 \rangle$ ZnTe crystal with an area of 18×20 mm² was used as the EO crystal. The optical component placed immediately after the EO crystal was different from that used in the conventional THz intensity detection method [54]. In the conventional method, the EO crystal is followed by a polarization analyzer that is oriented perpendicularly to the polarizer orientation. In this study, a quarter-wave plate was additionally inserted between the EO crystal and the crossed analyzer for the electric field detection. The axis of the quarter-wave plate was adjusted to be parallel to the axis of the polarizer. The analyzer was then rotated with a small angle, δ , in order to induce a local oscillator field, which is a phase-shifted fraction of the probe light. This method is described in section 3.3. The phase retardation angle of the probe light due to the EO effect, θ , which is proportional to the THz electric field, has been expressed in eq.(3.54). From the equation, we see that both positive and negative electric fields can be detected depending on the relation between I and I_b . The sensitivity of this detection method is better than that of the conventional intensity detection method. The largest magnitude of the negative value of θ detectable with this method is $-\delta$ as can be seen from eq. (3.54). If larger phase modulation is expected, the orientation angle, δ , must be set at a larger value or a negative value. The spatial distribution of the probe light intensity on the EO crystal was imaged onto the CCD device using an optical lens by reducing the image size by a factor of 5. The exposure time of the camera was set to 30 ms, which corresponds to the accumulation of 30 shots of THz pulses for a single image.

4.3 Time-resolved images

Spatial and temporal profiles of THz pulses depend very much on the propagating and observing conditions because the bulk of their energy portion is composed of low-frequency components [36]. To obtain good image quality in THz real-time imaging with a fixed time delay, the dependence of the image quality on the delay time must be understood. This section describes the relationship between the image quality and the on-axis THz waveform.

Chapter 2 described how the waveform of half-cycle THz pulses changes during its propagation in free space and during focusing [36]. In this experimental setup, the THz wave emitted from the large-aperture antenna behaves like a plane wave and is focused at the focal point of the TPX lens in the absence of the sample. The temporal waveform of the THz pulse at the focal point is expected to be approximately a half-cycle. Since the observation plane is far from the focal point, a waveform similar to the time integral of the half-cycle shape is expected to be observed resulting from the diffraction of high-frequency components. We measured the on-axis temporal THz waveforms at $z = f$ and $z = 5f/3$ without sample objects using the conventional balanced detection method. The distance between the antenna and the TPX lens was retained as in the imaging experiment, i.e., 300 mm. Figure 4.2 shows the waveforms obtained. Since the measurements were performed separately from the imaging experiments, the values of the delay times do not correspond to those of the image data. The waveform at the focal point was found to be approximately half-cycle having a tail with a small negative value. The existence of the negative tail shows that low-frequency components are diffracted out from the beam path before being focused while high-frequency components are not. By placing the lens closer to the THz source, a cleaner half-cycle waveform was observed at the focal point. The waveform observed on the image plane is composed of a slow (about 6 ps) rise, a fast decrease, and a negative tail which is almost constant in the observation time window. Imaging measurements were carried out in the delay time region between 2 and 10 ps, which roughly corresponded to the delay time region from 0 to 8 ps in the image data, where a significant temporal change in THz field is observed. The waveforms allowed us to understand the characteristics of THz radiation in this imaging system and under the temporal range of observation.

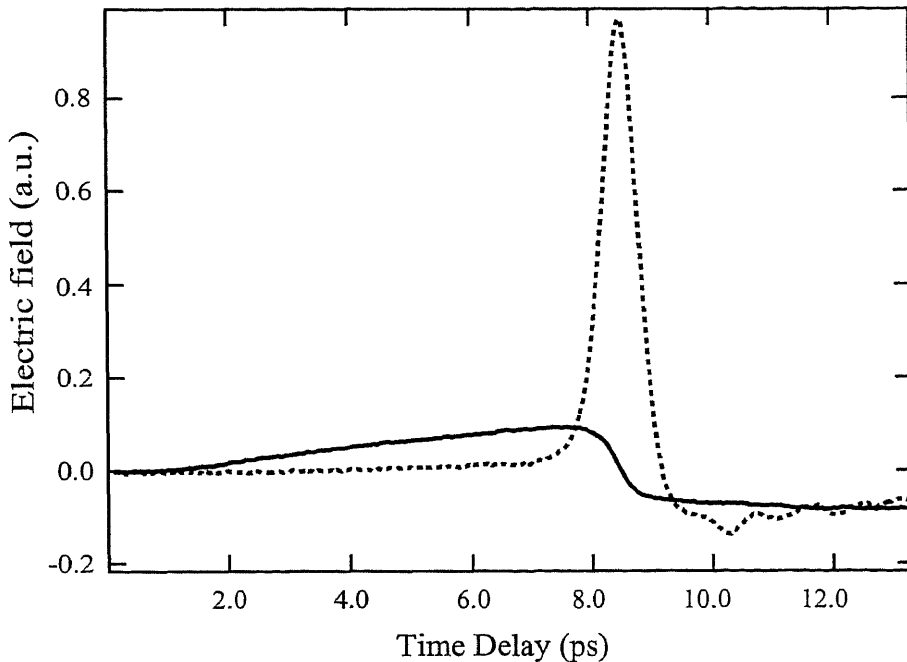


Figure 4.2: Axial waveforms on the focal plane, $z = f$, (dotted line) and on the image plane, $z = 5/3f$, (solid line) measured using the conventional balanced detection method.

Using this THz pulse, we obtained time-resolved field images of an object. The sample object used was a metal rod concealed in a paper box. The diameter of the rod was 2 mm. The box had a dimensions of 6.8 (width) \times 2.0 (thickness) \times 10.0 (height) cm, and the thickness of the paper was about 500 μm . This box was placed at 10 mm from the THz emitter with the largest face parallel to the emitter surface. The metal rod was attached in the diagonal direction to the inside of the face of the box that is nearest to the THz antenna. Without the rod, the THz pulse waveform observed on the image plane using an EO sampling method

underwent little change. Its shape or amplitude was not altered by the insertion of the paper box, and only a 1.17 ps delay in the peak arrival time was observed. We detected the 2D distribution in the intensity of the probe beam I_0 , the background intensity I_b and the time-dependent signal intensity I . By substituting them into eq. (3.54), the THz field images were obtained. Figure 4.3 illustrates gray scale mappings of the electric field images obtained at several delay times without (reference images: left column) and with (sample images: right column) the metal rod in the box. When the sample object was removed, the delay time dependence of the

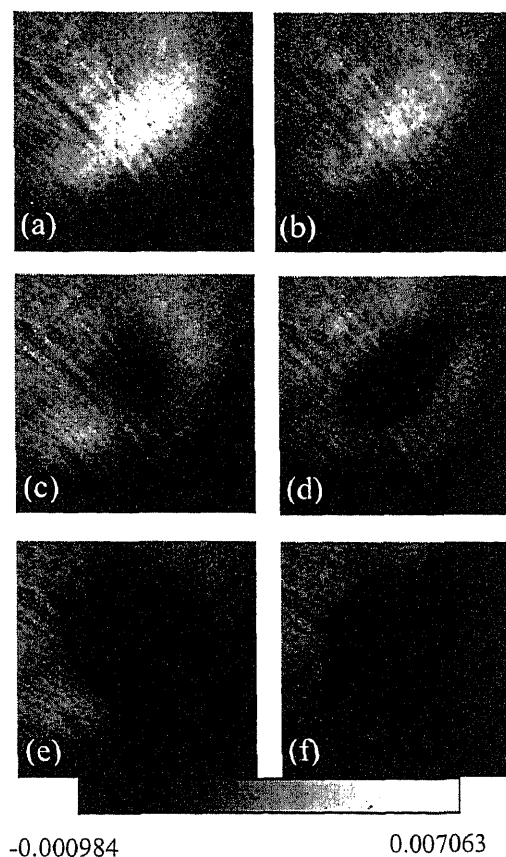


Figure 4.3: Left column: reference images; electric field distributions obtained with an empty paper box as an object. Right column: sample images; field distributions obtained using a metal rod in the paper box. Images in (a) and (b) were obtained at a delay time of 5.0 ps, the (c) and (d) at 5.7 ps, and (e) and (f) at 6.0 ps. These delay times correspond to those in figure 4.4. The color coding indicates the value of THz-field-induced phase modulation, θ , in equation (3.54). Each image corresponds to an area of 27×27 mm on the object plane.

spatial distribution of the THz field was to behaved similarly to that reported in a previous work [54], as shown in the left column in figure 4.3. The image shown in figure 4.3(a) corresponds to the peak time of the THz pulse waveform at the center of the beam. In the time window shown here, a hole, the black area at the center of THz beam, appeared, as in figure 4.3(c), and became larger as the delay time increased, as in figure 4.3(e). The existence of a dark area at the right bottom corner in all images is attributed to an inhomogeneity of the pellicle beam splitter. The reflectivity of the beam splitter had a smaller value in this area. The ambiguous images may be caused by a low signal-to-noise ratio of approximately 16 dB and by the quality of the EO crystal. In figure 4.3(b), which is the image of the sample object obtained at the same delay time as that of figure 4.3(a), the shape of the rod is not observed clearly. At times later than the peak, as shown in figures 4.3(d) and 4.3(f), we can ascertain the rod as a dark area in the sample images, although its width in image (f) is much larger and the length is shorter than those of the actual object. These artifacts can be explained by the ring phenomena, i.e., focused half-cycle THz pulses form like an annual ring because of frequency-dependent focal beam size

described in section 2.4 and a major portion of long-wavelength components.

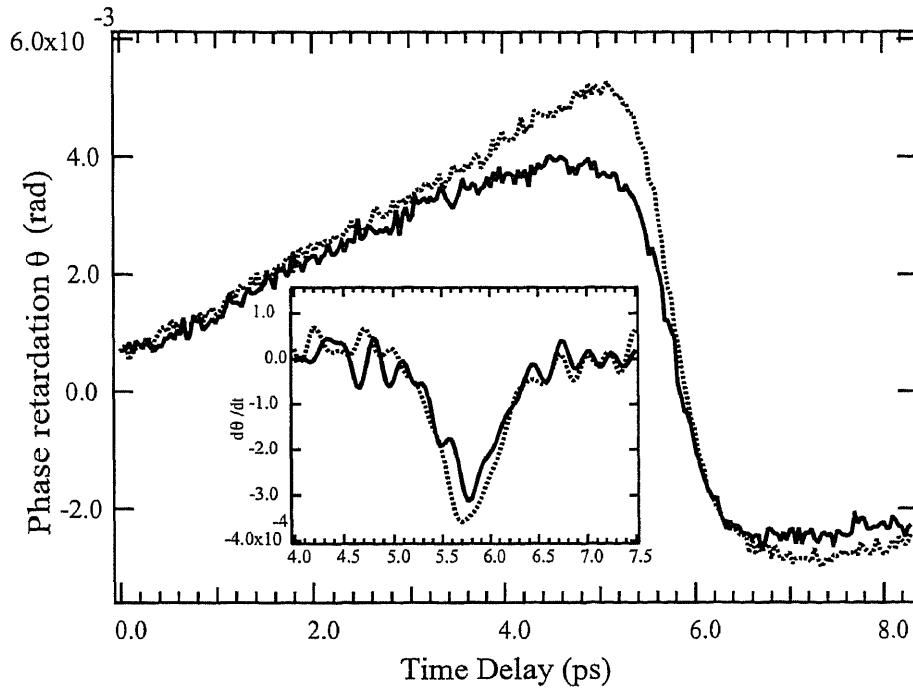


Figure 4.4: Temporal waveforms extracted from the central pixels of images in figure 4.3: reference (dotted line), sample (solid line). The dotted line shows the waveform observed with an empty paper box as an object, and the solid line shows that observed using a metal rod in the box. The inset shows the time-derivative of the phase modulation.

This experiment indicates that an appropriate time period exists for observing a clear image of an object. We extracted the temporal waveforms of the THz field at the center of the image from a series of images taken at every 33 fs of delay time. Figure 4.4 shows the waveforms observed with and without the metal rod in the paper box. The inset shows the time-derivative of the phase modulation. To obtain the time-derivative curves, the original waveforms were smoothed by low-pass filtering below 4 THz in the Fourier domain. Waveforms were also extracted at several off-axis points, although they are not shown here. The off-axis waveforms were similar to those observed on-axis with differences in arrival time and duration of the decrease. The appropriate time of 5.7-5.8 ps, which was used to observe the image in figure 4.3(d), corresponds to the time window where the temporal change in the THz field was largest (see peaks in the time-derivative of the phase modulation in the inset of figure 4.4). Interestingly, it was not the period where the difference between the two waveforms is largest, i.e., around 5 ps. This observation can be explained by considering the spectrum of the half-cycle pulse. Since the amplitude of low-frequency components is relatively high, this contributes to the strength of the THz field, particularly at the peak in the THz pulse. For this reason, we cannot observe the object at the peak time because the low-frequency components deteriorate the spatial resolution. In other words, the amplitude of the high-frequency components is largest at the delay time with the steepest transients in the THz field.

We introduced digital processing to eliminate the artifacts which are the result from the characteristics of the focused THz beam itself. This was accomplished by considering the difference and the ratio of sample images obtained by passing the THz beam through the rod inside the box with respect to the reference images without the rod at the same time delay. In the left column of figure 4.5, the differences between the images are shown. These were obtained by subtracting the reference image data from the sample image data at the corresponding time delay. Division images, which were obtained by dividing the sample image data by the reference image data, are shown in the right column of figure 4.5. With a time delay of 5.0 ps, which

corresponds to peaks in the THz waveforms, the metal rod appears as a round dark area in the difference image shown in figure 4.5(a), while the rod in the division image at the same delay time, figure 4.5(b), is not clear. At this delay time, the difference in the field with and without the rod is large but the ratio is not, which can be verified by figure 4.4. Around the peak time, the temporal change in THz field is relatively small. The THz field around the peak time is contributed to mainly by low-frequency components. This can explain the low spatial resolution observed in figure 4.3(d). The shape of the rod was best reproduced at 5.7 ps, both for the difference and division images, as shown in figures 4.5(c) and (d). The division image produced an object shadow closer to the actual sample shape than did the difference images. The smudge at the central area of images at 6.0 ps, as shown in figures 4.5(e) and 4.5(f), is attributed to the characteristic of the focused THz beam itself as mentioned previously.

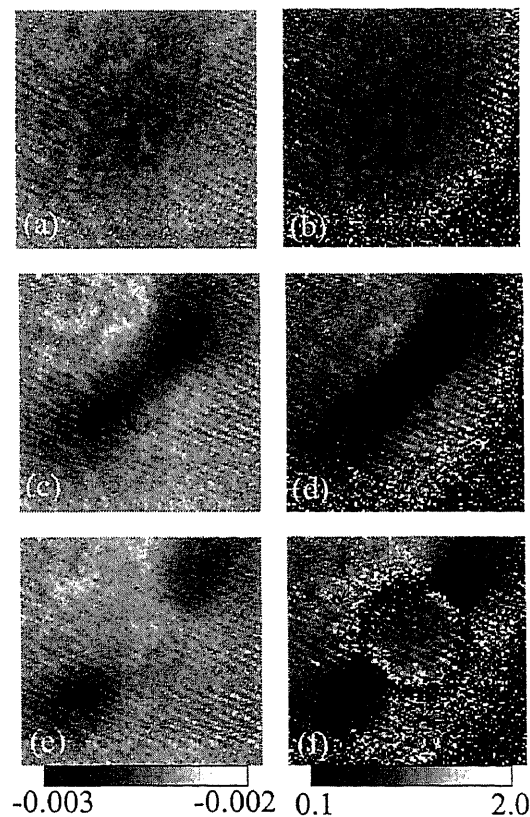


Figure 4.5: Left column: difference images, obtained by subtracting from the sample image data in figure 4.3 the reference image data at respective delay times. Right column: division images, obtained by dividing the sample image data by the reference image data. Delay times at each line are the same as used in figure 4.3.

In conclusion, the dominance of low-frequency components of a half-cycle THz pulse does not allow the object to be visualized over all delay times. For a real-time imaging system, the time delay should be fixed at a time when the THz field changes rapidly with time. Image processing by dividing the sample image by the reference image gave the best result because of the absence of a THz beam profile effect, as seen in figure. 4.5(d). However, this method limits some applications in which envelopes cannot be separated for recording the reference image. This problem can be solved if one knows the difference in delay times, Δt , when the THz pulse goes through the envelope and air. Assuming the envelope is homogeneous and that the THz beam profile is not changed after passage, the reference image corresponds to the air-passing THz image taken at a delay time advanced by Δt with respect to the delay time of taking the sample image.

4.4 Frequency-resolved images

Besides enabling weak THz signal detection, the OHD method has the advantage that field amplitude and relative phase at specific frequencies can be obtained by Fourier transformation. By scanning the optical delay between the pump and probe pulses, we obtained the THz field waveform at each position in the image simultaneously. All the waveforms were Fourier transformed to yield frequency-resolved THz images. The calculation of the Fourier transformation dealing with 200 frames of time-resolved data takes only a few minutes. Each frame was resolved to 123×123 pixels. In the calculation, the electric field images were first calculated from the observed data. Then the temporal waveform was extracted at each spatial point from a series of time-resolved images and padded with zeros to a length of 1024 before calculating one-dimensional Fourier transformation. The Fourier amplitude image at 0.35 THz for the empty box used as the object and that of the metal rod in the box are shown in figures 4.6(a) and 4.6(b), respectively. When the frequency was scanned from low to high frequencies, the sample object first faintly appeared around 0.2 THz, which corresponds to the central frequency of the system bandwidth. Although the spectral image (b) shows the object's shape more clearly than the time-resolved image shown in figure 4.3(e), the whole rod is not revealed. This is attributed to the non-uniform spatial distribution of the THz field. We corrected for this effect by dividing image (b) by the reference image (a). The result is shown in figure 4.6(c). It can be seen clearly that the division image uncovered the entire shape of the sample in the observed area. Figure 4.6(d) is the division image of the same sample at 0.53 THz. Interestingly, the dark area in this image corresponds to the boundary of the object. This can be attributed to the complex structure of a high-frequency amplitude profile of the THz pulse when the THz pulse passes through the lens, as observed by Matthew *et al.* [55].

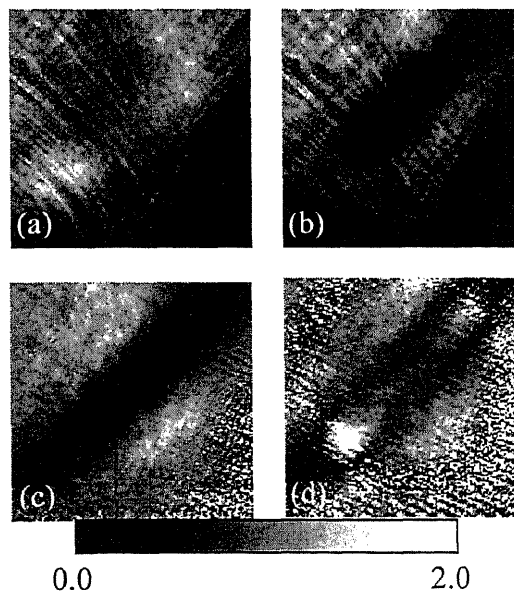


Figure 4.6: Fourier amplitude images and division images. (a) is the Fourier amplitude image at 0.35 THz calculated from the image series obtained using an empty box as the object and (b) is that obtained using a metal rod in the box. (c) is the division image at 0.35 THz, i.e., image (b) divided by image (a) and (d) is the division image at 0.53 THz.

Figure 4.7 shows the shadow of a 4-mm aluminum slab attached on paper as amplitude and phase images of some frequency components. It indicates that both amplitude and phase information express the existence of the slab. Interestingly, at a frequency of 0.261 THz the amplitude image in figure 4.7(a) shows pale area indicating aluminum slab, while the phase image figure 4.7(b) appears as bright area. This means that the phase image would reveal some information that is absent in the amplitude image.

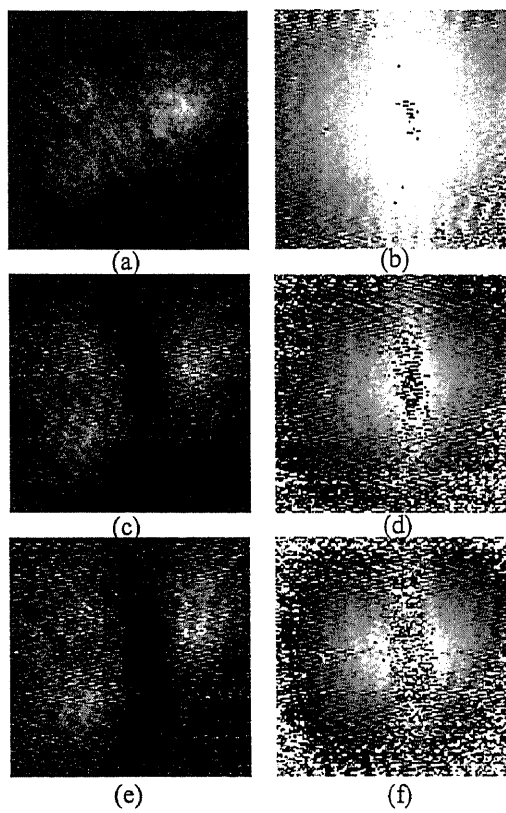


Figure 4.7: Amplitude (left column) and phase (right column) images of aluminum slab attached on paper at frequency 0.26 THz (a) and (b) , 0.49 THz (c) and (d), 0.64 THz (e) and (f).

The following experiment was performed to observe other shapes in the frequency domain and to confirm the edge images at high frequencies that were found in the previous experiment. The samples were the aluminum plates that were cut into triangular and circular shapes and attached to stiff paper. Each side of the triangle was 10 mm long and the diameter of the circle was 10 mm. Figure 4.8 shows spectral images of the reference (paper), triangle and circle at several frequencies. The reference image at frequency 0.7 in figure 4.8(c), we can clearly see the first-order diffraction called an Airy disc. In other words, the waves at any secondary point source on the lens according to, Huygens's principle are in phase at the bright area and out of phase in the dark area. Basically, the radius of the disk is inversely proportional to the frequency, as explained in section 2.7.2. The images at 0.38 THz shown in figures 4.8(d) and (g) and those at 0.5 THz shown in figures. 4.8(e) and 4.8(h) reproduce the sample shapes as dark regions. However the images at 0.7 THz in figures 4.8(f) and 4.8(i) show the objects' boundaries as dark traces. In the reference image figure. 4.8(c), the electric field in the central part is low, as shown by the dark area. It can be presumed that the spatial field distribution of the THz beam is not Gaussian-like at some frequencies because of the spherical aberration of the thick TPX lens used in these experiments. This caused difficulties in identifying circular objects shown in figure. 4.8(i). The image quality was improved by dividing the sample image by the reference image, although the result is not shown here.

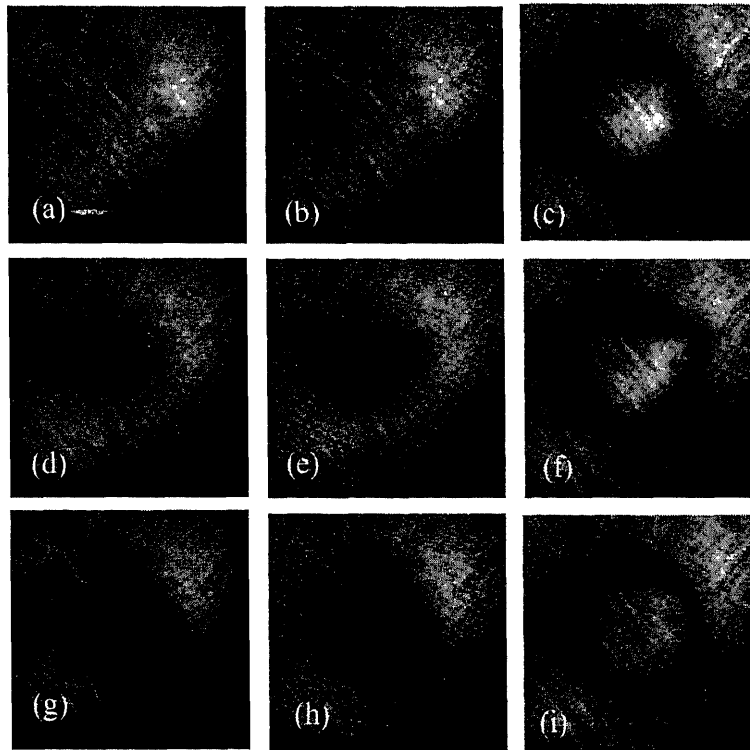


Figure 4.8: Top row: reference images; Fourier amplitude distributions obtained using stiff paper alone. Middle and bottom rows: sample images; Fourier amplitude distributions obtained using triangular and circular aluminum sheets attached to the stiff paper, respectively. The left, middle and right columns show frequency-resolved images at 0.38, 0.50 and 0.70 THz, respectively. Since difference in the signal amplitude among these frequency components is large, the same grey scale level is used only in the same column.

In conclusion, the two-dimensional electric field detection permits spectral images. This leads to the possibility of analyzing position-dependent properties. We experimentally performed the imaging of metal objects by detecting transmitted electric field on the image plane. Therefore, the detected images represent the shadow of interesting objects. From the experiments, we found that spectral images gave high contrast. However, frequency-resolved images of the THz beam which is focused by a lens are not uniform due to different diffraction limits of each frequency component. This affects the shadow image of the object in question. As a

result, the normalization with the reference image is necessary for this imaging configuration, particularly for a circular object.

4.5 Spatial resolution improvement

4.5.1 LT-GaAs antenna

When a GaAs wafer is used as a photoconductive material for a large-aperture antenna, it gives a half-cycle electromagnetic pulse. The temporal shape of THz pulse depends on the mobility of carriers in the substrate. The fluent of optical pulse and the type of substrate, therefore, determine the waveform of THz pulse [6]. The central frequency of THz pulse from the GaAs substrate is very close to dc, namely about 0.3 mm. In view of long wavelength components, it provides low spatial resolution if the pulse is used for imaging, see Chapter 3. We changed the substrate in order to move to a higher central frequency. Low-temperature grown GaAs (LT-GaAs) was chosen for this purpose. The lifetime of photogenerated carriers of LT-GaAs is estimated to be 1 ps, and the typical value for GaAs is over 100 ps [56]. Theoretically, higher frequency components can be enhanced using LT-GaAs substrate [57]. This is the effect of temporal change in mobility twice, rising and decaying, in the timescale of interest, i.e., 1 ps. Since the THz waveform in the far field is proportional to the time derivative of mobility, the pulse shape emitted from a LT-GaAs antenna becomes one cycle at the far field. This gives the central frequency shift to be higher in frequency domain.

A LT-GaAs is produced using molecular beam epitaxy of GaAs at low temperature substrate temperature (180-300°C) during growing in an excess As flux. It is, then, followed by a high temperature anneal (400-800°C) for short period time [58]. Control of the mobility and carrier lifetime is accomplished by varying the anneal temperature and time. Longer anneal time leads to higher mobility and longer carrier lifetime because of longer As cluster separation. In addition, photoexcited carrier lifetimes also increases with increasing anneal temperature [59].

We used a fast photoconductive layer epitaxially grown on GaAs as a photoconductive media and detected temporal THz waveforms at the focal point of a TPX lens. The 1- μm thick LT-GaAs layer was epitaxied on a GaAs wafer which has a thickness of 500 μm . The LT-wafer was fabricated with anneal time is 10 minutes. The carrier lifetime is, therefore, short. The diameter of the wafer was 50 mm. It was purchased from E&M cooperation. The measured waveforms were shown and compared with those obtained from GaAs emitter in figure 4.9. Pump fluent was varied from 7.52 to 255.73 $\mu\text{J}/\text{cm}^2$. The plots were vertical shifted, except the lowest pump energy. The pulse shapes at the same pump energy are a bit different. The waveforms of two emitters became more closer when the optical energy was increased. That means the optical light can penetrate deeper inside with high energy and generate photocarriers at the second layer, i.e., GaAs. Fourier transformation of the pulses pumped at 7.52 $\mu\text{J}/\text{cm}^2$ was plotted in figure 4.10 There is no significantly change in central frequency.

In the next experiment, we kept the pump fluent as a constant and observed the effect of the bias voltage on the waveform. The GaAs and LT-GaAs antennas were excited with the fluent of 0.94 $\mu\text{J}/\text{cm}^2$. The emitted THz pulses of 2-kV biased and 8-kV biased voltages are shown in figure 4.11. The graph shows that the strength of bias voltage does not affect to electron behavior in the LT-GaAs. As the results, the central frequency of THz pulse cannot be shifted to higher frequency by fabricating 1 μm LT-GaAs layer on a GaAs wafer.

Carrier lifetime of LT-GaAs was measured and compared with that of GaAs using a pump-probe experiment. The optical pump and optical probe pulses were brought from a mode-lock amplified Ti:Sapphire laser and focused on the surface of a sample in reflective configuration. The spot size of the pump pulse was 49.64 μm measured using a knife edge experiment. The probe pulses passed through an optical delay line. The pump pulses were guided to an optical chopper that its timing was synchronized with the laser clock at a frequency

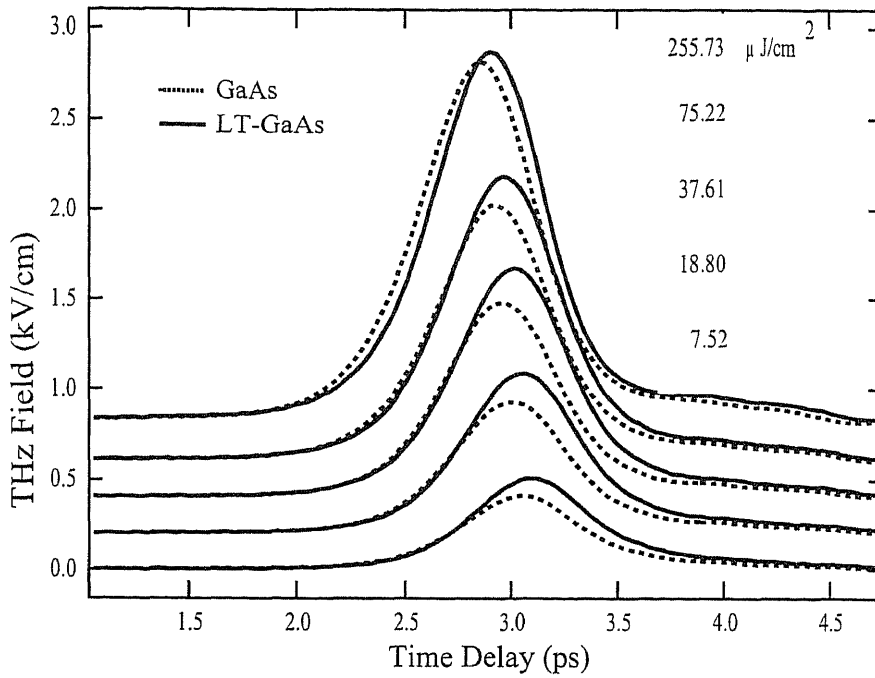


Figure 4.9: Pump fluent-dependent waveforms of GaAs (dotted line) and LT-GaAs (solid line) photoconductive emitters.

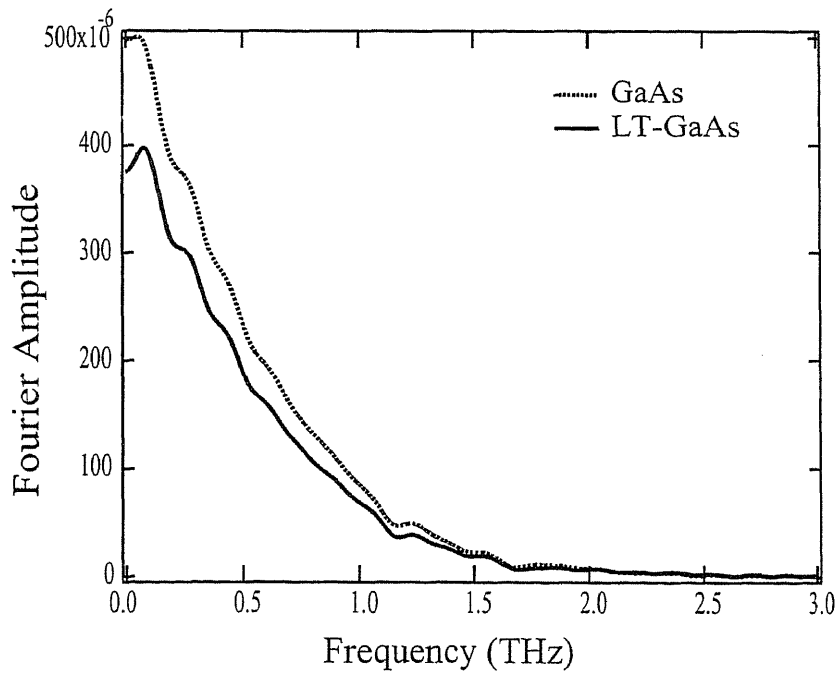


Figure 4.10: Fourier amplitudes of the waveforms in figure 4.9 at a pump fluent of 7.52 $\mu\text{J}/\text{cm}^2$.

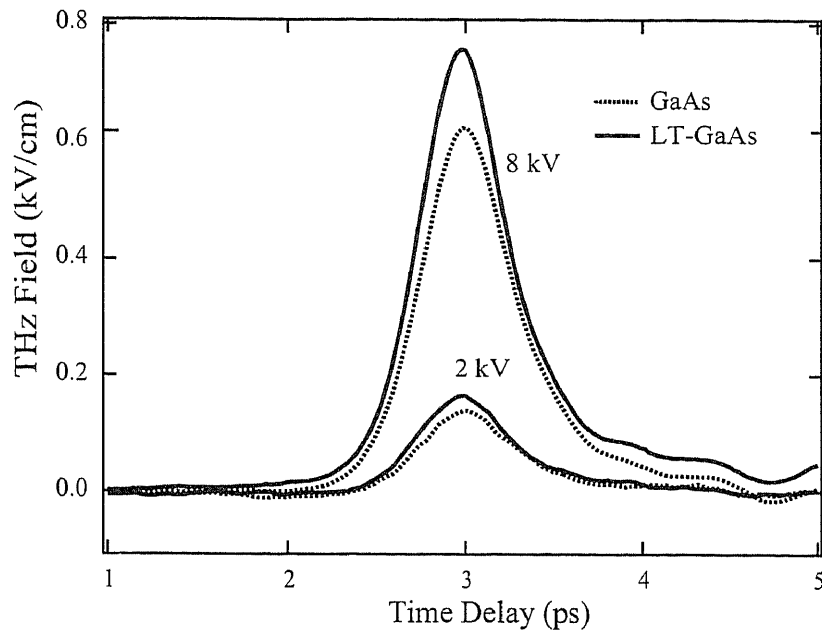


Figure 4.11: Waveforms of GaAs (dotted lines) and LT-GaAs (solid lines) emitters at bias voltages of 2 and 8 kV.

of 500 Hz. The pump and probe fluents were 117.60 and $112.38 \mu\text{J}/\text{cm}^2$, respectively. Carrier density, n , can be calculated as

$$n = A \times \frac{F}{d} / \left(\frac{hc}{\lambda} \right). \quad (4.1)$$

Here, A is the absorption coefficient of sample, F is fluent, d is skin depth, h is Planck's constant, c is the velocity of light in vacuum, and λ is the wavelength of excitation. The absorption coefficients of GaAs and LT-GaAs are both 0.7 [60]. But the skin depth of GaAs is $1 \mu\text{m}$ while that of LT-GaAs is $0.7 \mu\text{m}$ [61]. The carrier densities of GaAs and LT-GaAs with 800-nm pumping were 3.316×10^3 and 4.737×10^3 , respectively. The optical setup of pump-probe experiment is depicted in figure 4.12. The photoexcited responds of carriers

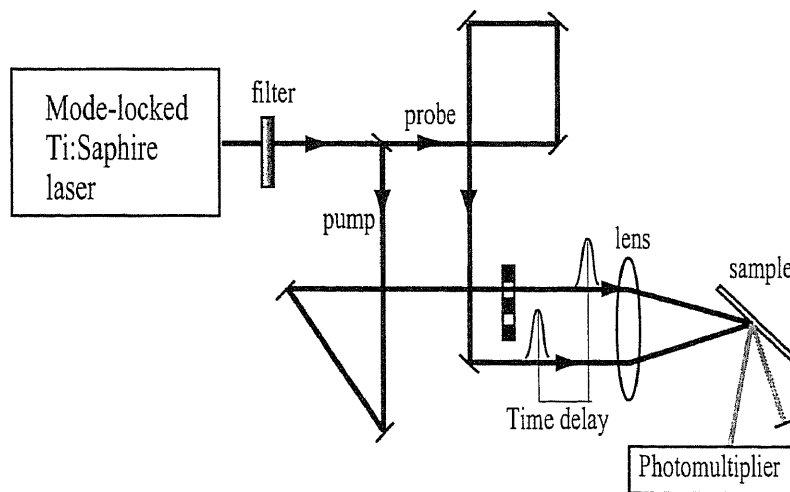


Figure 4.12: Optical setup for the pump-probe experiment.

on GaAs and LT-GaAs were plotted in figures 4.13 and 4.14, respectively. The decay was curve fitted with the function

$$f(t) = c_1 + c_2 \exp(-t/c_3). \quad (4.2)$$

The decay coefficient, c_3 , of GaAs is faster than that of LT-GaAs, i.e., 14.5 for GaAs and 18.3 for LT-GaAs, but the carrier lifetimes of both materials were about 100 ps. Figure 4.15 shows fine scale of time delay at the rising period between 0 to 840 fs. Sharp coherence spikes were observed in both response signals due to the short coherent time. Besides the phenomena, the signals are similar. As a result, it seems that the excitation pulse penetrates into the substrate, very low decaying electron and hole populations are generated, and the performance of the emitter is degraded. For a GaAs epitaxial layer, the absorption coefficient at 800-nm wavelength is about $1/\mu\text{m}$ [62]. Therefore, if the thickness of the epitaxial layer is $1\mu\text{m}$, about 30% of the light is absorbed into the substrate. In order to reduce substrate absorption below 5%, at least $3\mu\text{m}$ of the epitaxial thickness is required.

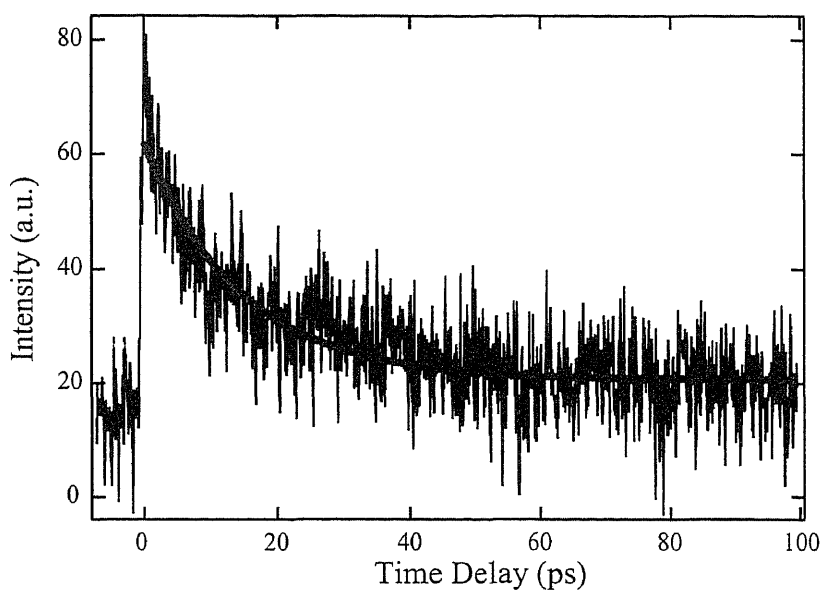


Figure 4.13: Respond of photoexcited carriers on GaAs surface with optical pump and optical probe. The fluent of the pump and probe pulses are 117.6 and $112.38 \mu\text{J}/\text{cm}^2$, respectively. The gray thick line shows curve fitting of the decay with a coefficient of 14.5 ps.

4.5.2 High-pass filtering

In THz imaging by scanning method, a two-dimensional image is constructed from characteristics of THz waveform that passed through a sample, which is translated on the focal plane, the spatial resolution of the image is determined by the spot size of the THz beam at the sample position. To achieve high resolution by using a large NA lens, a long time is required to complete a whole sample. In the case of two-dimensional imaging mode, the spatial resolution is determined by the peak wavelength of the spectrum. Using a half-cycle THz pulse from a biased large-aperture photoconductive antenna, the resolution is of the order of a millimeter. In our experiment, the peak frequency is about 0.2 THz corresponding to a wavelength of 1.5 mm. As it has a large resolution, it overcomes the obstacle of detecting a small object. In objective in this section was to investigate one way for improving the spatial resolution of the two-dimensional imaging by using a high-pass filter. Theoretically, the low frequency components that blur the image of an object will be compressed. The simple way to cut undesired longer wavelength out is to pass the pulse through a metallic hole. Adjusting the size of the hole, a cut off wavelength can be selected [63]. However, the overall field strength will be decreased greatly. To overcome this disadvantage, metallic hole arrays have been adopted for filtering electromagnetic waves in THz regime [64,65]. Transmission and phase-shift characteristics of the filter were studied with THz time-domain spectrometer [66]. However, the spatial distribution of transmitted beam had no longer been

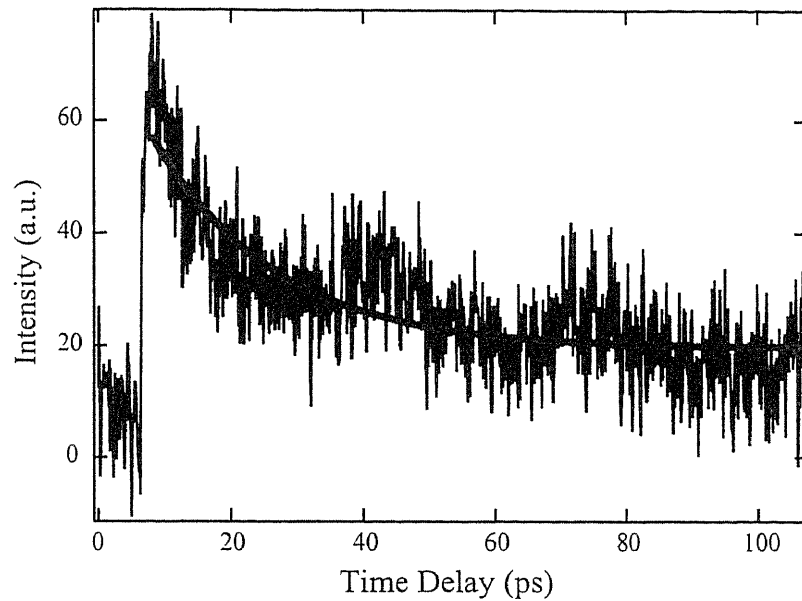


Figure 4.14: Respond of photoexcited carriers on LT-GaAs surface with optical pump and optical probe. The fluent of the pump and probe pulses are 117.6 and $112.38 \mu\text{J}/\text{cm}^2$, respectively. The gray thick line shows curve fitting of the decay with a coefficient of 18.3 ps.

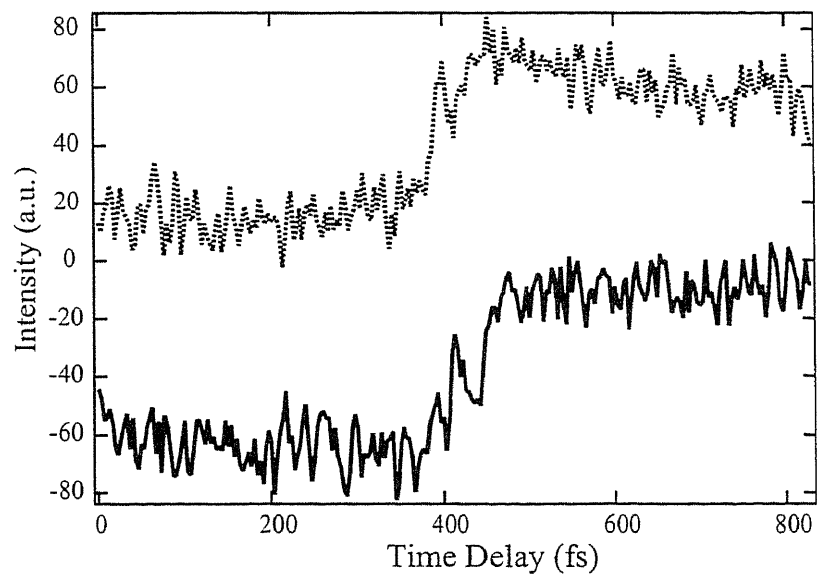


Figure 4.15: Responds of photoexcited carriers on GaAs (dotted line) and LT-GaAs (solid line) surface at rising in fine scale of figures 4.13 and 4.14.

studied. In this section, the studies of two-dimensional profile of filtered THz radiation will be illustrated. The filtered THz field was also used for imaging an object. Trade-off of using the filter in a imaging system will be stated. The theoretical approach of a hole array filter will be described as follows. The frequency dependence

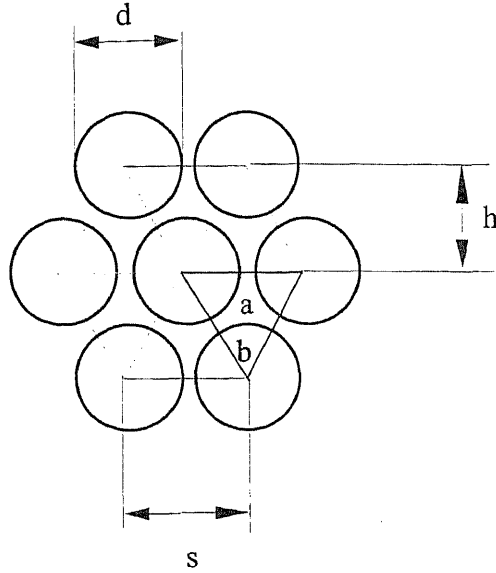


Figure 4.16: Schematic of hexagonally close packed filter. d represents diameter of circular holes, s is the vertical spacing, h is the horizontal spacing, a represents the unit cell area, and b represents circular opening area per unit cell.

of the transmission for a circular hole is determined by the hole diameter d , the hole spacing distance s , and plate thickness l . For frequency below the cutoff frequency ν_c the filter acts as a plane mirror with a very low leak rate, which is depends on l . A larger l gives a lower leak rate. To calculate the cutoff frequency for a circular hole arrays plate, we used the boundary conditions of a hollow waveguide in Maxwell's equations. Assuming, electromagnetic wave $E(z, t) = E_0 \exp(i\omega t - \gamma z)$ propagating inside a single hole oriented along the z -direction, the wave satisfies the boundary conditions: $E_z|_{\text{surface}} = 0$ for TM-modes and $\frac{\partial B_z(x, y)}{\partial n}|_{\text{surface}} = 0$ for TE-modes, where n is normal to the surface of the waveguide [67]. The complex propagation factor is defined in term of frequency as

$$\gamma = \frac{2\pi}{c} \sqrt{\nu_c^2 - \nu^2}. \quad (4.3)$$

Below the cutoff frequency, $\nu < \nu_c$, the propagation factor γ is real, the wave is, then, $E(z, \nu) = E_0 \exp(-\frac{2\pi z}{c} \sqrt{\nu_c^2 - \nu^2})$. That means it is attenuated or evanescent. Above the cutoff frequency, $\nu > \nu_c$, the propagation factor becomes imaginary. The wave obeys $E(z, \nu) = E_0 \exp(-i\frac{2\pi z}{c} \sqrt{\nu^2 - \nu_c^2})$. In this case, the wave can propagate in the waveguide without loss but the phase changes. The cutoff frequency is simple to solve in cylindrical coordinate yielding a Bessel function. The dominant propagation mode in circular waveguide is TE_{11} with the cutoff frequency,

$$\nu_c = 1.841 \frac{c}{2d}, \quad (4.4)$$

where d is the diameter of the hole. The value 1.841 is the zero pole of first derivative of Weber function (the Bessel function of the second kind). For example, the cutoff frequency of 1-mm-diameter hole is 175 GHz. Typically, an hexagonally close packed pattern is used for producing a regular two-dimensional grid structure, shown in figure 4.16. Because of this cutoff behavior, the hole array acts as high-pass filter, which reflects below the cutoff frequency. However, the transmitted frequency bandwidth is limited because the hexagonal hole array represents a two-dimensional grating that forces electromagnetic waves with frequencies greater than

the diffraction frequency ν_{diff} to be diffracted into the first grating lobe [68]. At normal incidence diffraction into the first lobe appears at

$$\begin{aligned}\nu_{\text{diff}} &= \frac{c}{\hbar} \\ &= \frac{2c}{s\sqrt{3}}.\end{aligned}\tag{4.5}$$

For optimum design it is necessary to calculate the diffraction limit, namely maximum frequency of transmitted band, of the filter. In general, the spacing s should be small enough to prevent significant power radiation to the first grating lobe. Another parameter that we should pay attention for filter design is the power transmission. It can be approximated by considering the geometry of the filter or by solving Maxwell's equations [67]. From the triangle area in figure 4.16, the power transmission is given by

$$\begin{aligned}T &= \frac{b}{a} \\ &= \frac{1}{2} \left(\frac{\pi d^2}{4} \right) / \left(\frac{s^2 \sqrt{3}}{4} \right) \\ &= \frac{\pi}{2\sqrt{3}} \left(\frac{d}{s} \right)^2.\end{aligned}\tag{4.6}$$

In the experiment, we used two filters, with different hole diameters, spacing distances and the thicknesses, as shown in figure 4.17. One was a mesh of a speaker, with $d = 1$ mm, $s = 1.5$ mm and cutoff frequency $\nu_c = 176$ GHz, called a speaker filter. The other was designed for wider bandwidth and in that the diameter was bigger while the spacing distance was shorter. The diameter and the cutoff frequency were 1.4 mm and 126 GHz, called a grill filter. The filters were placed at a distance of 5 mm from the emitter. Filtered THz field was focused by the TPX lens. The waveforms that passed through the filters were measured at the focal point $z = f$ and at $z = 3/2f$ (the position of imaging plane when do two-dimensional imaging of an object). In figures 4.18 and 4.19 the waveforms of reference pulses are represented as the dotted lines. The solid lines and the dashed lines show the sample pulses, which were obtained by placing the different filters in the THz beam path. By taking the Fourier transform of these time domain data. One obtains the complex amplitude spectrum $E_{\text{THz}}(\nu)$ in form of both magnitude $|E_{\text{THz}}|$ and phase $\phi(\nu)$. The magnitudes $|E_{\text{THz}}|$ are displayed on the right hand side of figures 4.18 and 4.19. At the focal point, the main peaks were reduced to 40% and 35 % of the reference peak when the sample pulses passed through the grill filter and speaker filter, respectively. The negative portions of them were deeper. Moreover, the tails vibrated with long period. The cutoff frequencies, measured from the experimental results, were 165 GHz for the grill filter and 180 GHz for the speaker filter. The cutoff frequency of the grill filter was higher than theoretical value by 39 GHz while that of the speaker filter give the nearer one. Since the grill filter area was designed to exactly fit to the THz emitter size, i.e. $30 \times 30 \text{ mm}^2$, the portion of low-frequency beams that diffracts to be larger than the filter area were blocked. Therefore the cutoff frequency ν_g is higher than the theoretical approach. At the center of imaging plane, as can be seen in figure 4.19, we can observe the significant changes to the sample waveforms, namely the peaks have inverse phase respected to the reference pulse (dotted line) and the vibration of their tails. It seems that the frequency components that are higher than 250 GHz were suppressed.

The ratio of these Fourier transformed sample and reference data represents the magnitude transmittance of the filters, $T = |E_{\text{sample}}(\nu)|/|E_{\text{reference}}(\nu)|$. The transmittance of different filters measured at $z = f$ (top) and at $z = 3/2f$ (bottom) are shown in figure 4.20. Below the cutoff frequencies, the transmittances were reduced rapidly. However, a frequency below 50 GHz seems not to have been filtered. This is caused by including time-domain data with long period, in which the vibration effect of the filter was added. The depression of the

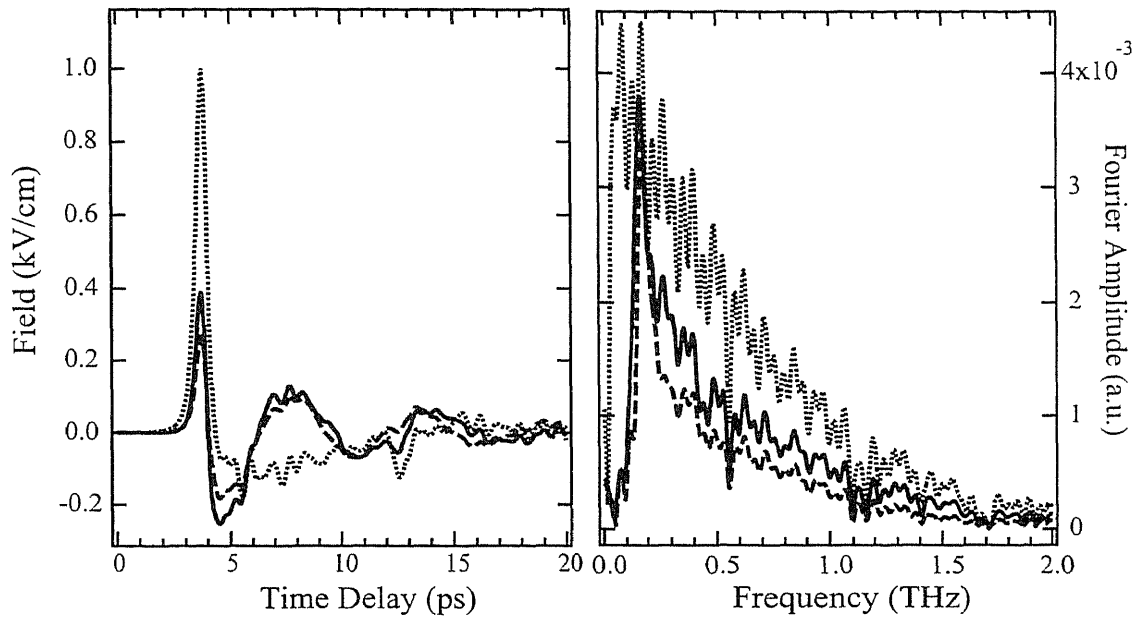


Figure 4.18: Temporal waveforms (left) and their Fourier amplitudes (right) of the reference pulse (dotted line) and the filtered pulse by the grill filter (solid line) and by the speaker filter (dashed line). The data were measured at the focal point of the lens using EO sampling detection.

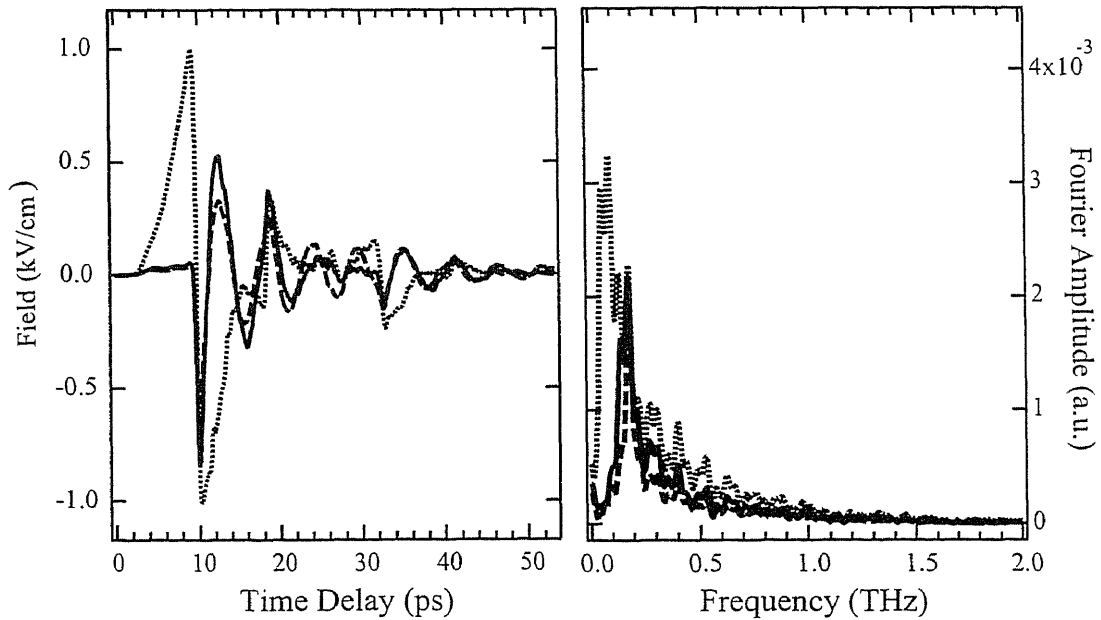


Figure 4.19: Temporal waveforms (left) and their Fourier amplitudes (right) of the reference pulse (dotted line) and the filtered pulse by the grill filter (solid line) and by the speaker filter (dashed line). The data was measured at a distance $3/2f$ from the lens.

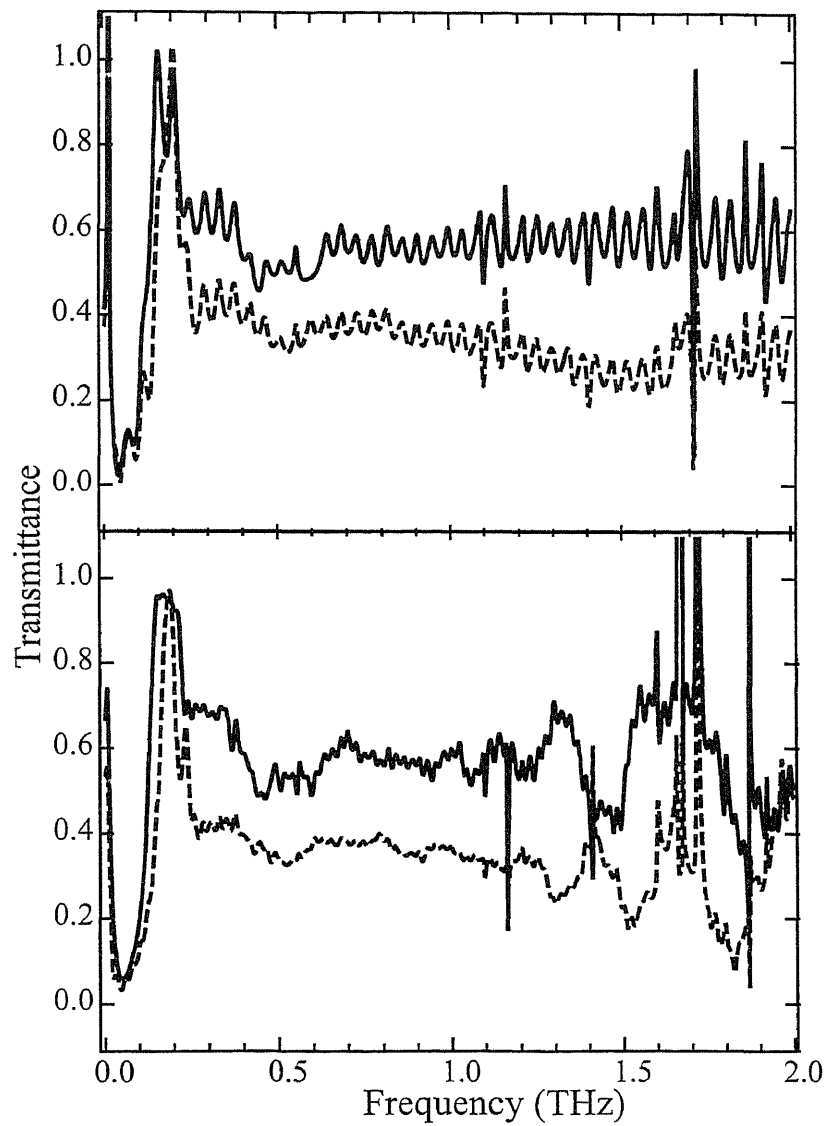


Figure 4.20: Power transmittance of different filters: grill filter (solid line) and speaker filter (dashed line). The spikes found above 1.5 THz were affected by water vapor absorption, which did not involve in passed band.

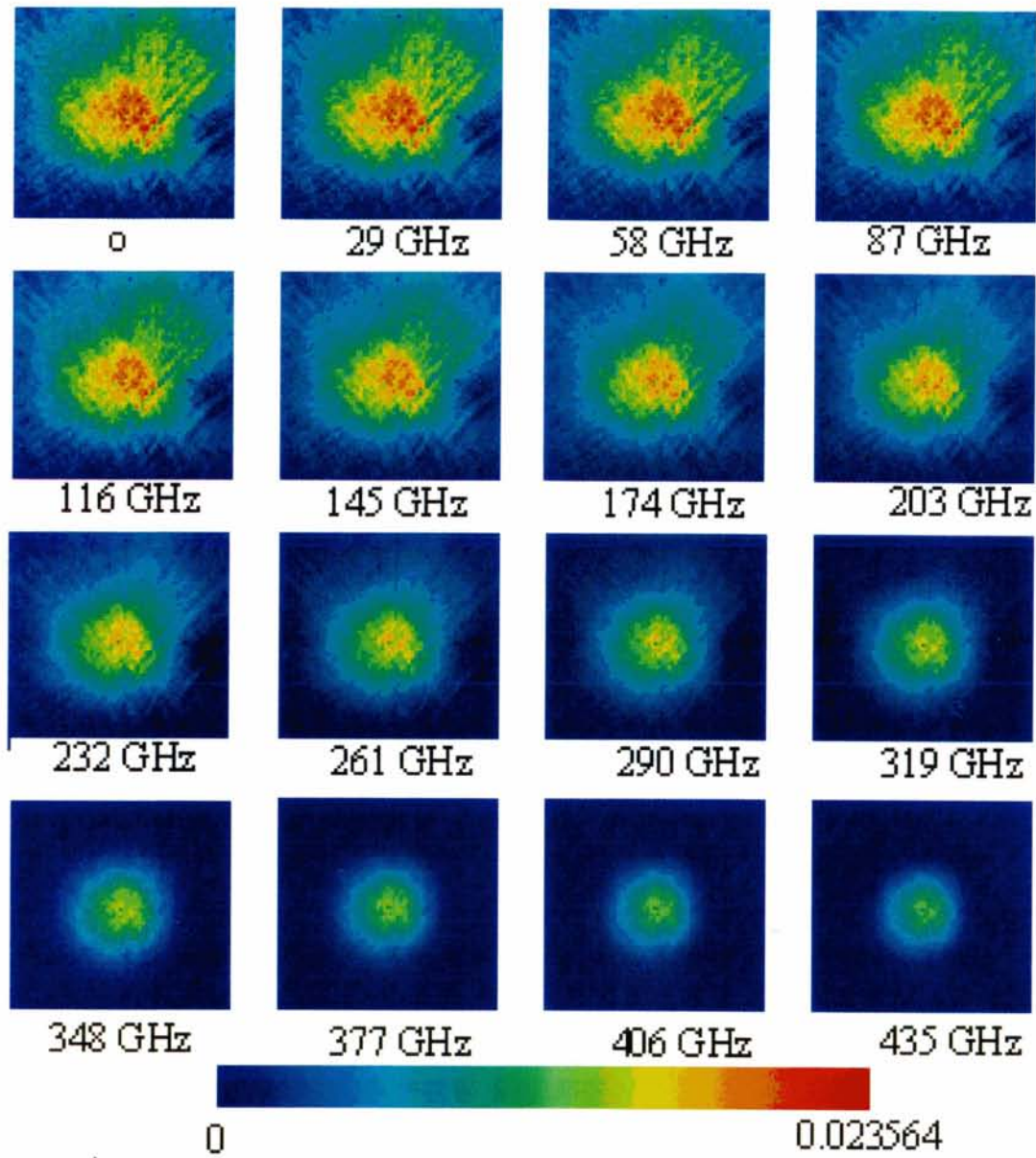


Figure 4.21: Frequency amplitude images of the reference THz beam. They were transformed from the series of 200 time-dependent frames. The exposure time of the CCD camera was set to be 30 ms.

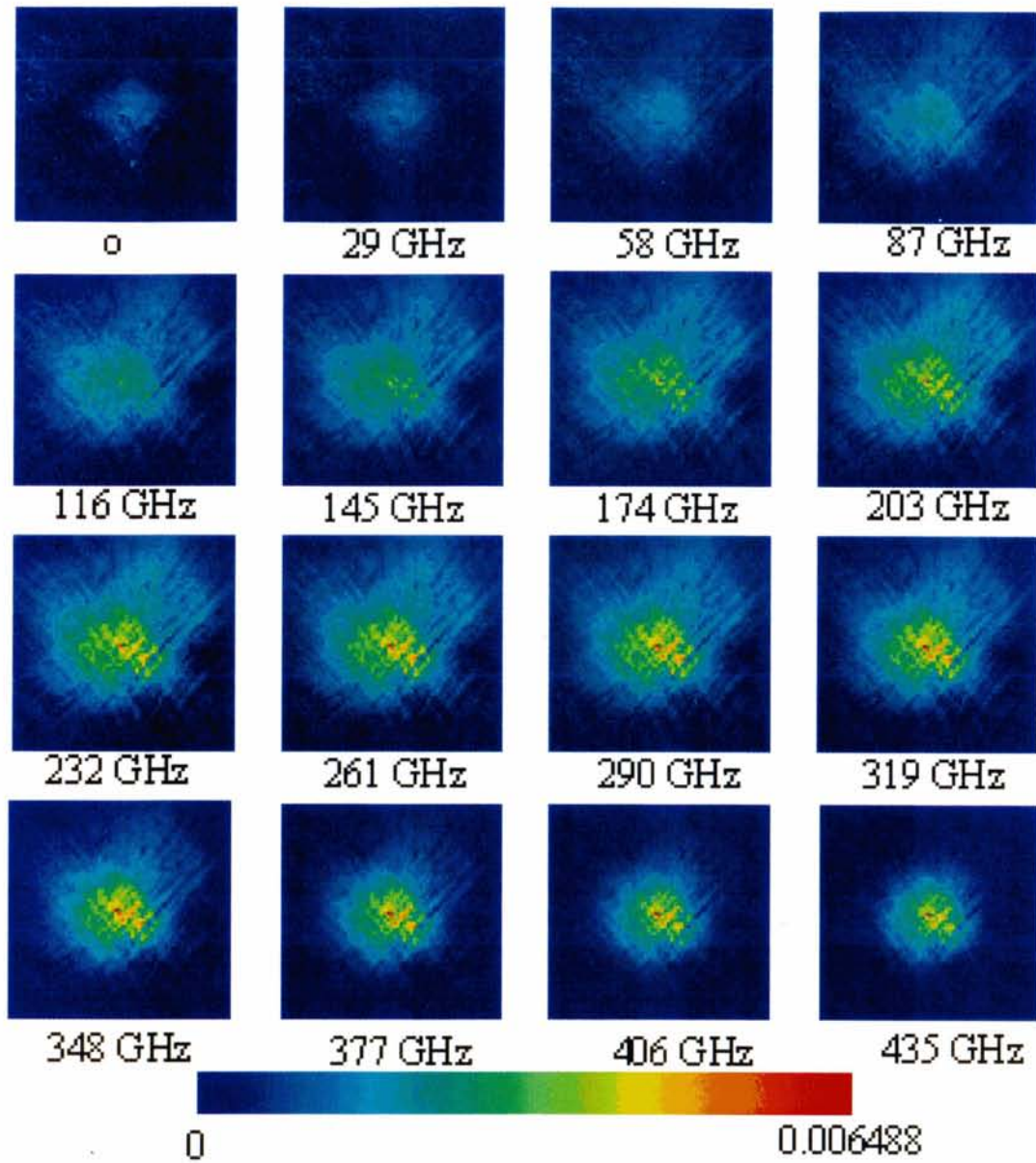


Figure 4.22: Frequency amplitude images of the filtered THz beam using the grill filter.

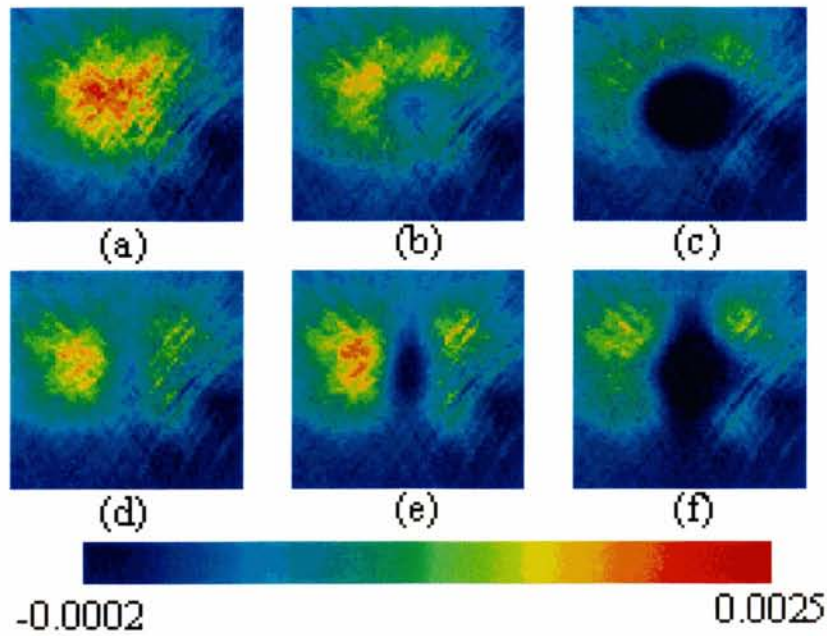


Figure 4.23: Time-dependent images of the reference THz field (a)-(c) and that of the THz field which the sample, i.e. the metal rod with 2-mm in diameter, was placed between its beam path (d)-(f). The time step of different column was 240 fs. The images in the same column were detected at the same delay time. The image size was $27 \times 27 \text{ cm}^2$ corresponding to area on the object plane.

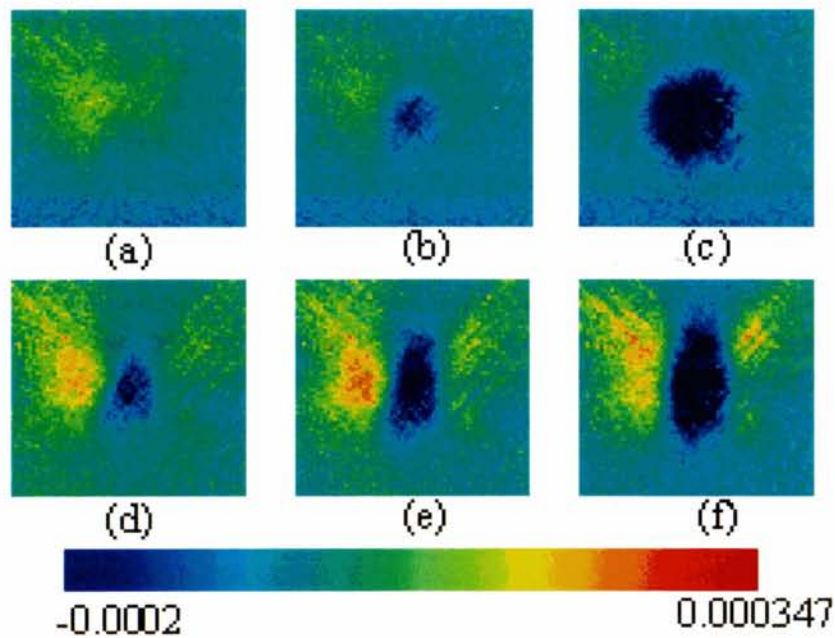


Figure 4.24: Time-dependent images of the filtered THz field (a)-(c) and that of the filtered THz field when the sample was placed between its beam path (d)-(f). The grill filter, as shown in figure 4.17 was inserted between the THz emitter and the sample. The time delay were the same as using when detected the images in figure 4.23.

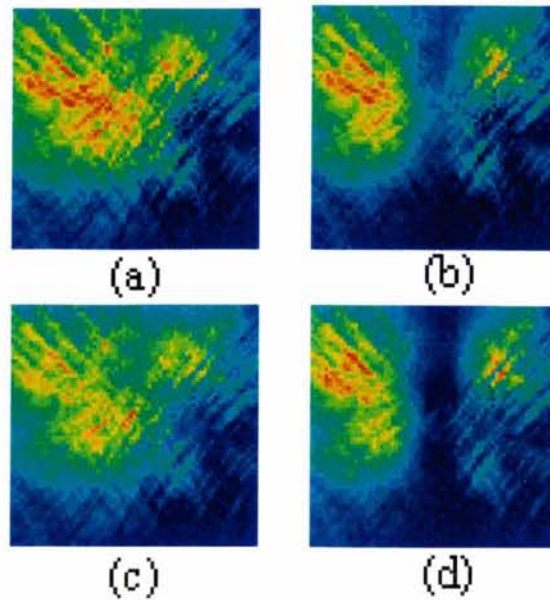


Figure 4.25: The Fourier amplitude images at 288 GHz of the reference THz beam (a), the metal rod (b), the filtered THz beam (c), and the metal rod using filtered THz field (d).

4.6 Conclusions

Two-dimensional THz imaging using half-cycle electromagnetic pulses from a large-aperture biased photoconductive antenna was performed. It was found that the best images of an object were obtained at the delay time with steep transients in the THz field. This feature provides a possibility of real-time imaging by fixing the time delay at the time when a rapid change in THz field occurs in which it is necessary for observing a moving object. The frequency-resolved images show the presence of an object at low frequency components while the images of their edges were found at comparatively high frequencies.

We did the experiment for improving the spatial resolution using the LT-GaAs wafer as a photoconductive material instead of a GaAs wafer and using the high-pass filters. The first attempt did not achieve the aim because the LT-GaAs layer on the normal GaAs wafer that provides short carrier lifetime is not thick enough. Therefore the bulk carrier behavior does not change as the hypothesis that supposes that short carrier lifetime would cause broader spectrum and shift the peak frequency to be higher. However the carrier lifetime of the alternative wafer was confirmed by the pump-probe experiments that there is no significant difference from the normal type GaAs wafer. For the other method, we found that the filter acts as a band-pass filter. Practically, the performance of filter in frequency domain is similar to dividing the sample image with the reference image. Furthermore, the filter is applicable for the precisely band for two-dimensional spectroscopy.

Chapter 5

Real-Time High-Speed Terahertz Imaging

5.1 Introduction

With the long history of optical imaging, high-speed detection, i.e., up to a few thousand frames per second (fps), has been successfully and widely applied to basic research and everyday occurrences. For instance, it has been used to examine the splash of a water drop or stop such events such as the impact of tennis ball with a racket and the burst of a balloon. In THz region, increasing the frame rate is one of imaging challenges because it allows the monitoring of single-time events occurring at a high speed such as explosion and laser ablation. In this chapter, we describe how to improve the capturing rate up to 1000 fps. Since the laser system was operated at a repetition rate of 1 kHz, the image is then a single-shot of the THz pulse. The significance of the single-shot imaging is explained in the second section. A movie of a moving object was obtained using a single THz pulse per frame. The one problem of high-speed imaging is that noise level is as high as the signal. We applied some digital imaging processes to enhance the image quality, explained in section 5.4.

5.1.1 1-kHz imaging

Real-time or two-dimensional THz imaging was first demonstrated by Wu *et al.* [5]. They obtained a two-dimensional intensity distribution of a focused THz beam using an electro-optic sampling technique and a thermoelectrically cooled CCD camera at a frame rate of 38 fps, which is comparable to that of a standard television (30 fps). The electric field detection technique and a capturing rate up to 69 fps were used to perform spatio-temporal detection of few-cycle THz pulses in 1999 by Jiang and Zhang [70]. However, a report about imaging an object with the two-dimensional system had not been reported until 2002. THz images of stationary and moving samples were observed at a frame rate of 30 fps and 10 fps, respectively [34]. Obviously, the accumulation of a larger number of THz pulses per frame and a lower frame rate provide higher image quality. However, it is meaningful to achieve THz imaging at a high frame rate, which is comparable to an optical frame rate for investigating ultrafast phenomena. However, the data acquisition is not limited only by the speed of the image detector, but also by the intensity of the THz radiation, detection technique, and timing. Recently, Miyamaru *et al.* reported a high-frame-rate measurement of a THz beam profile at 1000 fps using a complementary metal-oxide semiconductor (CMOS) camera [53]. However, in their report, half of the image data were used as referenced for a subtraction detection mode yielding high signal-to-noise ratio achievement and a sample has not been imaged at a high frame rate.

1-kHz imaging system requires a high THz radiation source, a sensitive detection technique and a high-

speed camera. The large-aperture biased photoconductive antenna provides a high enough electric field strength to do the imaging. We used the phase-sensitive electro-optic sampling to map the THz field on an observation plane to an optical signal as described in chapter 3. The output signal was then captured by the high-speed CCD camera. The capture timing of the camera needs to be properly synchronized with the optical probe pulse.

5.1.2 Single-shot imaging

The acquisition of two-dimensional images can be achieved in real time using electro-optic sampling method and a CCD camera. The response time of an EO crystal is negligible because an index of refraction changes along the propagation of THz pulse. It allows the observation on the order of probe pulse width, i.e., 150 fs in our experiment, if the image is taken in one shot. The imaging of a single-image THz pulse was ideal because the power of a single THz pulse was not enough to induce detectable phase change in the probe pulse. The requirement of a clean signal and good image quality is another reason that THz images were taken with a long integration time [34]. In this research, with the help of high bias voltage in the THz generation process and high sensitivity of the phase-sensitive electro-optic sampling, the single-shot THz imaging has been achieved.

5.2 Imaging system

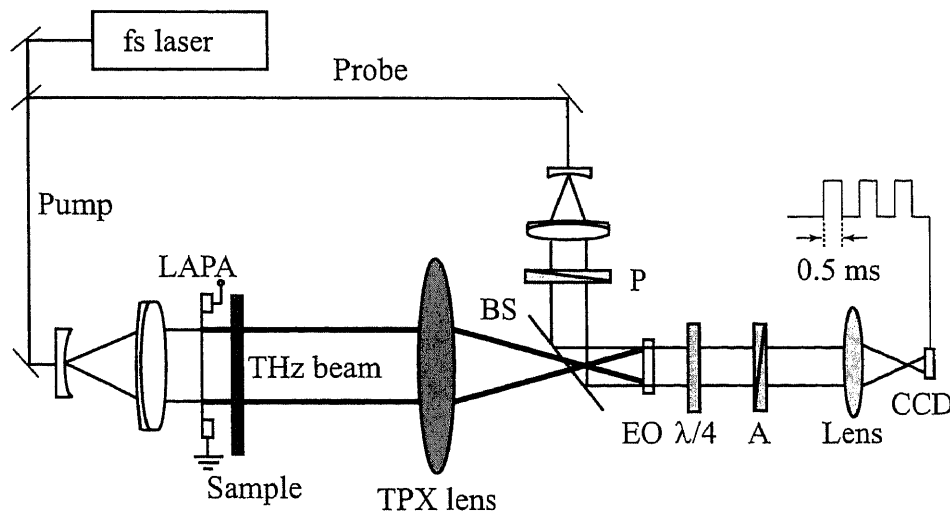


Figure 5.1: Schematic of the experimental setup. LAPA: large-aperture photoconductive antenna, BS: pellicle beam splitter, EO: electrooptic crystal (ZnTe), $\lambda/4$: quarter-wave plate, P: polarizer, A: polarization analyzer. The exposure time of the CCD camera is 0.5 ms.

The schematic of the experimental setup is shown in figure 5.1. It is similar to that used for the two-dimensional imaging described in previous chapter, except the CCD camera and synchronized timing. The high-speed CCD camera (Photron, FASTCAM-PCI 2K) allows a latency from the trigger pulse to start of exposure of 0.5 ms when a laser probe pulse illuminates. An external trigger was constructed to have 3 output signals to control the timing of Ti:sapphire laser, the high-voltage generator and the CCD camera. Each port has own delay controller. Figure 5.2 shows the time chart of detection. The input signal and optical signal are synchronous by the external trigger. The internal signal is released by the CCD component. The output that indicates the exposure time is read out as for normal operation. The full size of the CCD chip is 512×480 pixels ($3.79 \times 3.50 \text{ mm}^2$), with a pixel well size of $7.4 \times 7.4 \mu\text{m}^2$.

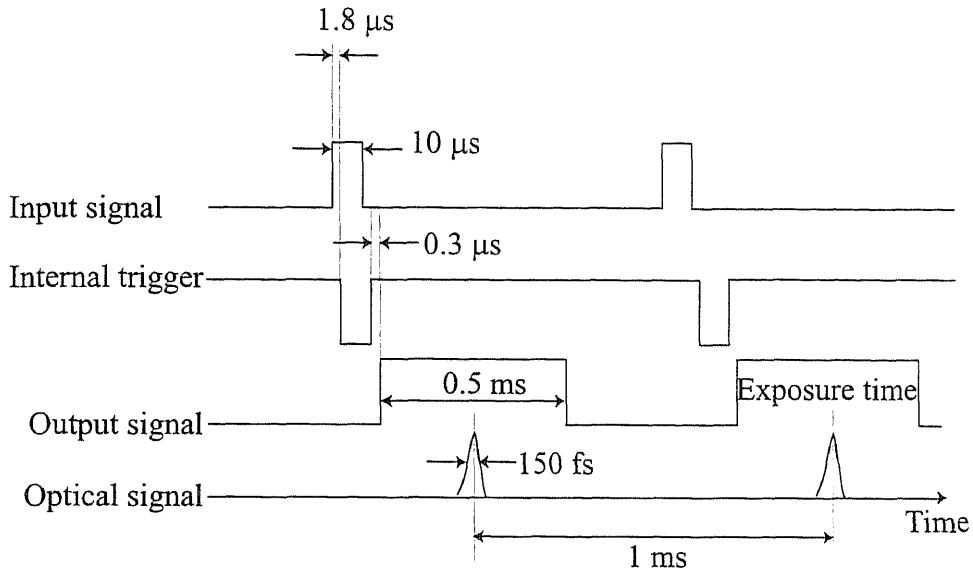


Figure 5.2: Time chart of the imaging operation. The input signal and the optical signal are controller by an external trigger which the time delay between them is adjustable. The internal signal is generated from the CCD component. The output signal is used for adjusting the timing of probe pulse to be in the exposure period.

5.3 Snapshots of moving samples

Images of a sample object were obtained at the delay time when the temporal change rate in the THz field was highest as described in chapter 4. The THz wave distribution on the object plane was imaged onto the EO crystal. The probe pulses mapped the feature on the crystal to CCD camera according to the phase modulation induced by the THz field.

A large-aperture photoconductive antenna enables a large beam size and a high electric field when biased with a high dc voltage. When a GaAs wafer is used as a photoconductor, it gives almost half-cycle electric pulses [6,36]. This makes their spectra have a peak near dc. Figure 5.3 depicts the generated waveform (dashed line) measured at the focus of the TPX lens, $z = 0$, using an EO sampling method. The inset shows its Fourier amplitude (dashed line). As can be seen from the graph, the spatial resolution of the imaging using this THz pulse, determined by a half of the central wavelength, is limited at about 1 mm. The axial waveform on the image plane of the imaging configuration, at $z = 49.2$ mm, was measured using the same method, as shown in the same figure (solid line). Apparently, it deviates from that measured at the focal plane in which it has a long rise and a fast decay. This is the result of large diffraction in high-frequency components, as can be seen in the inset of figure 5.3. Images of a sample object could be ascertained at the time when the temporal change rate in the THz field was high, namely 0.2–0.8 ps in the graph because of the dominance of high-frequency components in this time region [71]. The field distribution on the object plane was imaged onto the EO crystal. The probe pulses mapped the feature on the crystal to the CCD camera according to the phase modulation induced by the THz field. The spatial intensity distribution of the modulated pulses, I , was obtained by the CCD camera. The THz electric field was then calculated by substituting the probe intensity I_0 , optical background intensity I_b , and I into eq. (3.54).

We captured images of a moving object at a frame rate as high as 1000 fps. The sample object was a metal rod of 2.6 mm in diameter. The rod was hung by a string and, when at rest, placed vertically at the center of the THz beam at a distance of $3f$ from the TPX lens. Real-time images of the rod, while swinging, were obtained. The CCD camera captured an image for each probe pulse that mapped THz field on the EO

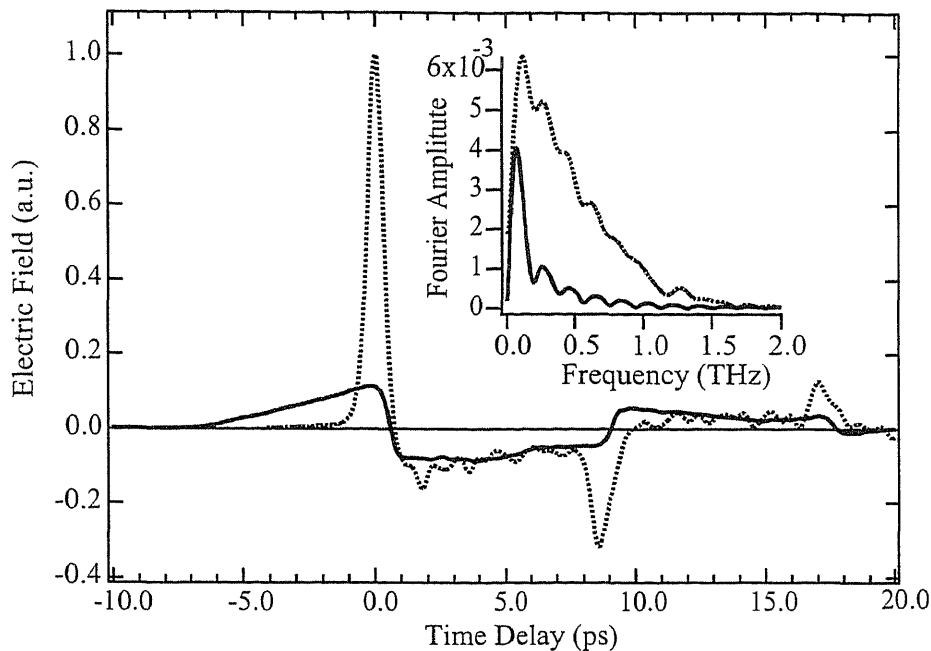


Figure 5.3: Normalized THz waveforms measured at the focus, $z = 0$, (dashed line) and at $z = 49.2$ mm (solid line) using an EO sampling detection. The second and third peaks are the reflection of the main THz pulse inside the GaAs wafer and inside the EO crystal, respectively. The inset shows their Fourier amplitudes.

crystal. The THz image shows the shadow of the metal rod, as the dark area, where THz waves could not pass through.

The resulting images were contaminated by a variety of noise sources, particularly significant among them was that from the CCD camera. In this experiment, photon noise and thermal noise were dominant because the probe pulse was weak and the images were taken at a high frame rate. This photon noise occurred because of incorrect counting of the same number of photons for consecutive frames. In addition, thermal noise was from a stochastic source of electrons in a CCD well. Other noise came from laser instability. These noises can be reduced by image processing.

When the image quality is low, a level-detecting method cannot find the object reliably. Therefore, image processing was designed according to the following steps: (a) correct for non-uniformity in the THz beam and (b) suppress noise. The effect of the dark hole at the center of the images, which was attributed to the focusing characteristics of half-cycle THz pulses [54], was reduced by dividing the image data by the reference field image, namely the image of the THz field when the sample object was removed. The resultant images are shown in figures 5.4(a) and 5.4(b). Image (b) was obtained 20 ms after image (a). They have been cropped, into 120×100 pixels, to show the area surrounding the subject of the interest, corresponding to dimension of 8.8×7.4 mm² on the object plane. This process revealed the real shape of the rod as a dark area.

The use of the Gaussian kernel for noise filtering has become popular. This has been applied to several areas such as edge finding and scale space analysis. Since commercially available image processing software typically affects only one image at a time, we implemented a computer program that can manipulate the whole set of the images at one time. This provides an efficient conceptual framework for image processing tasks. The action of the Gaussian filter to a single-shot image has been explained in great detail in following section. The results of applying the Gaussian filter operator with the variance of 1 are shown in figures 5.4(c) and 5.4(d). Obviously, Gaussian filtering produced clearer images. It should be noted that a larger value of variance in

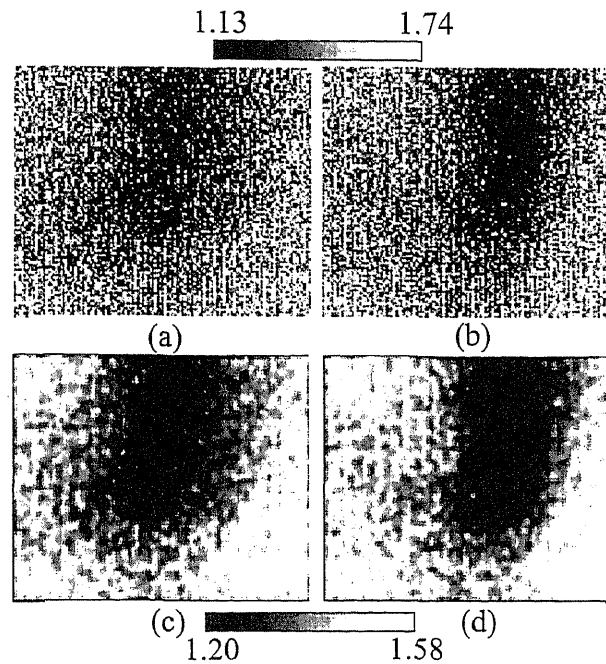


Figure 5.4: Division images (a) and (b); obtained by dividing the sample image by the reference image. Image (b) was obtained 20 ms after image (a). Images (c) and (d) are the results of applying a Gaussian filter operator to images (a) and (b), respectively. The upper and lower bars indicate the gray scale for the upper and lower images. The values of each image are mapped to percentile range 10%–90%.

filtering makes the image more clearer but sharp edges and specular highlights may be softened. The calculation processes took 0.5 second per frame on a PC. Figure 5.5 shows more snapshots of the Gaussian filtered data representing the movement of the rod from left to right in 56 ms. The time interval between two adjacent images was selected to be 7 ms for observing the change. Frequency components that can resolve the object were only found in the central area of the image. The part of the rod that was out of the THz beam or in at the nonactive area of the EO crystal (the right bottom corner) appeared bright. This effect can be seen in the photographs at 49 and 56 ms.

5.4 Image enhancement

Any image acquired by optical, electro-optical or electronic waves is likely to be degraded by the sensing environment. The degradations may be in the form of sensor noise, blur due to camera misfocus, relative object-camera motion, random atmosphere turbulence, and so on. Image enhancement refers to sharpen images features such as edges, boundaries, or contrast to make a graphic display more useful for display and analysis. The enhancement process should not increase the inherent information content in the data. But it should increase the range of chosen features so that can be detected easily. The image enhancement includes gray level and contrast manipulation, noise reduction, edge crispening and sharpening, filtering, interpolation and magnification, pseudocoloring, and so on [72]. Among these methods, we chose the filtering to reduce noises.

5.4.1 Normalization

The spatial distribution of THz beam depends on that of its laser pump beam which is assumed to be a Gaussian shape. It leads to the fact that the observing beam is not spatially uniform. Therefore projection of

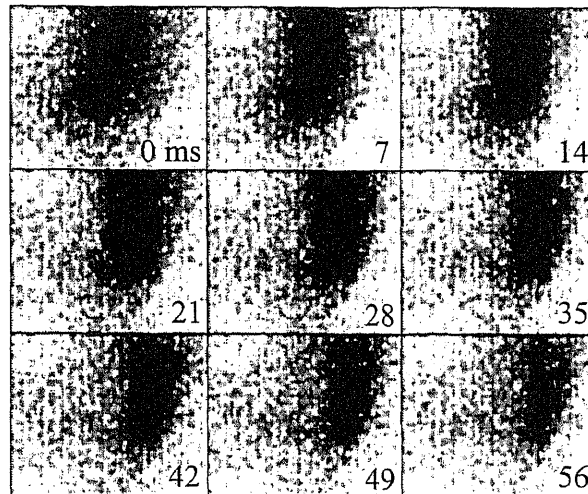


Figure 5.5: Snapshots of the movie showing the translation of the metal rod from left to right with a time interval of 7 ms. The plot parameters were the same as using in figure. 5.4.

an object does not owe to the object shape alone but is also contaminated by the configuration of the focused THz beam. The THz image of the object can be improved by dividing by the THz image without the object. The figure 5.6 shows the improvement of this action. The black region on figure 5.6(a) indicates the hole from the focusing of THz pulse and the present of the object, i.e., the rod. It is not clear where the rod is. But we can see obviously in normalized image, figure 5.6(b), that the rod was hanged vertically.

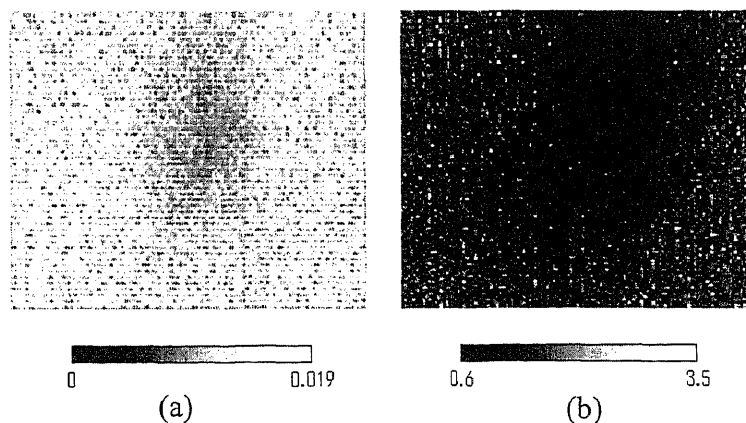


Figure 5.6: Single-shot images of the metal rod : (a) electric field image (b) the ratio of the electric field image of the rod and the THz image without sample.

5.4.2 Noises from a CCD camera

Images acquired through modern sensors may be contaminated by a variety of noise sources, particularly the use of modern CCD cameras where photons produce electrons that are commonly referred to as photoelectrons. Noises from a CCD camera can be classified into 6 types, i.e., photon noise, thermal noise, one chip electronic noise, KTC noise, amplifier noise, and quantization noise [73]. In our experiment, photon noise and thermal noise are dominant because the intensity of one light pulse is very low and images are taken with fast speed. We cannot assume that in a given pixel for two consecutive frames, the same number of photons will be counted.

The photon noise is then the produced. An additional, stochastic source of electrons in a CCD well is thermal energy. Electrons can be freed from the CCD material itself through thermal vibration and then, trapped in the CCD well, be indistinguishable from “true” photoelectrons. By cooling the CCD chip it is possible to reduce significantly the number of “thermal electrons”.

The CCD camera model FASTCAM-PCI of Photron Ltd has been used to capture laser light pulse by pulse or about 1000 frames per second (fps). The CCD chip size is 512 x 480 pixels. For the high speed capturing, i.e., 1000 fps, only one portion of the CCD, namely, 256 (horizontal) x 120 (vertical) pixels is active. The timing of the camera is synchronized with the laser system and the bias voltage generator by an external trigger. Figure 5.7 displays the intensity of probe pulse. Obviously, we can see the horizontal ladder lines, i.e., black, white, black, and so on, in the image. This error maybe caused by the manner of data are read from the CCD chip to the recording media. The average exceed valve of white lines is 25. We can get rid of the error by subtracting the exceed value while transforming from a BMP file to a TEXT file.

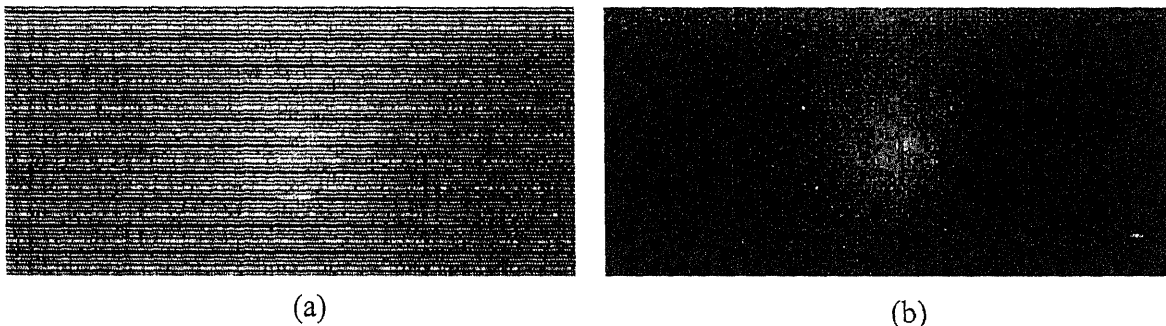


Figure 5.7: Intensity of a single probe pulse (a) raw image; (b) enhanced image by subtracting the exceed value.

In figure 5.7, we can see the noises on the top zone of the images. The noise arises at the upper 20 lines of every image. The images in this document were cut the upper noise contained lines, except figure 5.7. Another noise occurs all pixels in some images, called additive noise. The intensity of the images are significantly higher than their neighbors, see figure 5.8(a). The bright images happen at around the 20th frame and every 200 frames afterward. One can clean this noise but subtracting exceed value in the strange frame at all pixels but the exceed values of each image are not the same value. So we cannot program to clean this kind of noise out automatically. If the sequence data are taken into consideration, the strange image may be replaced by its neighbor image or by the averaged image of two neighbors. The other uncontrollable noises can be reduced by filter-based operations as follows.

5.4.3 Filtering

Filtering can be operated both in spatial and frequency domains. Frequency filtering is more appropriate if no straightforward kernel can be found in the spatial domain, and may also be more efficient. The filter performance is described as follows. Figure 5.9 shows images that were applied by various filters. The Gaussian filter created smoothening result and noise enhancement. This can also be regarded as a low-pass result where the low special frequencies are preserved. Maximum and minimum filters can be used for elimination of salt (high value noise) and pepper noises (low value noise). The maximum filter works when the noise is low value or the pepper type and the minimum filter works best for high value noise (salt type). The result imaged of applying these filter to the image in figure 5.4(b) are shown in figures 5.9(b) and 5.9(c), respectively. Percentile filter relies on ranking the data, such as the minimum, maximum or median. The image shown in figure 5.9(d) is a median filter. Gaussian derivative filter combines derivative operator, which used for edge detection, and

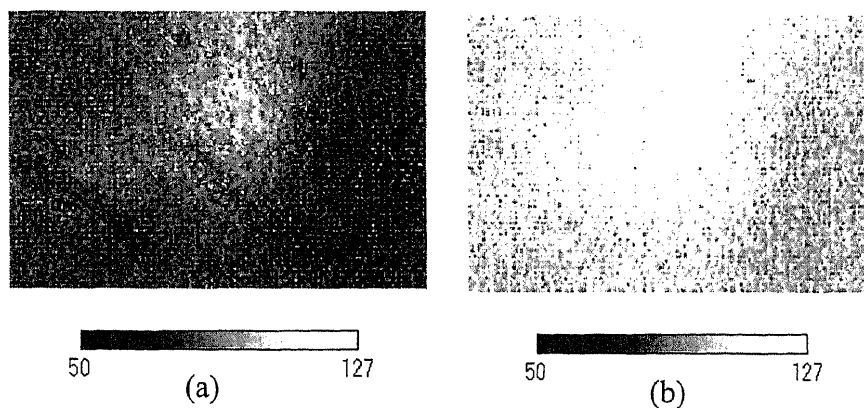


Figure 5.8: Additive noise (a) normal image (b) noisy image. The image size is 120×100 pixels.

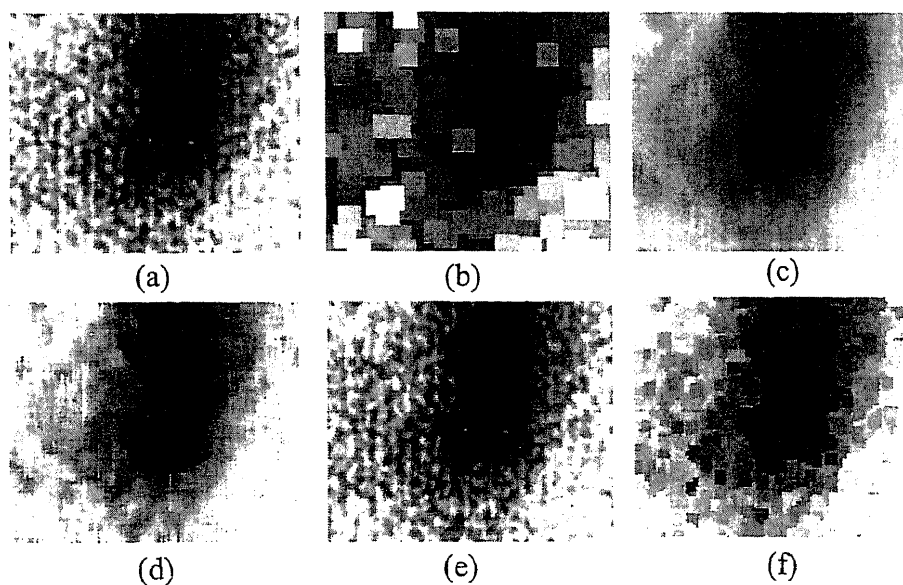


Figure 5.9: Images of the metal rod operated by various filters: (a) Gaussian, (b) Maximum, (c) Minimum, (d) Percentile, (e) Gaussian derivative and (f) Kuwahara. The filters operated on the image in figure 5.6(b) by using the image processing package in Matlab.

Gaussian smoothing shown in figure 5.9(e). Kuwahara filter is an edge-preserving filter, which smoothens an image without disturbing the sharpness and position of edges, as in figure 5.9(f).

Frequency domain of image

The frequency domain is a space in which each image value at image position (u, v) represents the amount that the intensity values in image vary over a specific distance related to (u, v) . In the frequency domain, changes in image position correspond to changes in the spatial frequency. For example, the frequency 0.1 (or 1 period every 10 pixels) means that in the corresponding the spatial domain image the intensity values vary from dark to light and back to dark over a distance of 10 pixels. One would refer to the number of pixels over which a pattern repeats (its periodicity) in the spatial domain. The spatial frequency domain is interesting because: 1) it may make explicit periodic relationships in the spatial domain, and 2) some image processing operators are more efficient or indeed only practical when applied in the frequency domain. In most cases, the Fourier transform is used to convert images from the spatial domain into the frequency domain and vice-versa.

Frequency Filter

Frequency filtering is based on the Fourier Transform. The operator usually takes an image and a filter function in the Fourier domain. This image is then multiplied with the filter function in a pixel-by-pixel fashion:

$$B(u, v) = A(u, v)H(u, v) \quad (5.1)$$

where $A(u, v)$ is the input image in the Fourier domain, $H(u, v)$ the filter function and $B(u, v)$ is the filtered image. To obtain the resulting image in the spatial domain, $B(u, v)$ has to be re-transformed using the inverse Fourier Transform. Since the multiplication in the Fourier space is identical to convolution in the spatial domain, all frequency filters can in theory be implemented as a spatial filter.

The form of the filter function determines the effects of the operator. There are basically three different kinds of filters: low-pass, high-pass and band-pass filters.

1. Low-pass filter attenuates high frequencies and retains low frequencies unchanged. The result in the spatial domain is equivalent to that of a smoothing filter; as the blocked high frequencies correspond to sharp intensity changes, i.e., to the fine-scale details and noise in the spatial domain image.
2. High-pass filter yields edge enhancement or edge detection in the spatial domain, because edges contain many high frequencies. Areas of rather constant gray-level consist of mainly low frequencies and are therefore suppressed.
3. Band-pass attenuates very low and very high frequencies, but retains a middle range band of frequencies. Band-pass filtering can be used to enhance edges (suppressing low frequencies) while reducing the noise at the same time (attenuating high frequencies).

Better results can be achieved with a Gaussian shaped filter function. A Gaussian filter smoothes an image by calculating weighted averages in a filter box. The advantage is that the Gaussian has the same shape in the spatial and Fourier domains and therefore does not incur the ringing effect in the spatial domain of the filtered image.

Gaussian filter

The use of the Gaussian kernel for smoothing has become extremely popular. This has to do with certain properties of the Gaussian (e.g. the central limit theorem, minimum space-bandwidth product) as well as

several application areas such as edge finding and scale space analysis. The Gaussian filter in spatial domain is

$$h(x, y) = \left(\frac{1}{\sqrt{2\pi}\sigma} \exp\left(-\frac{x^2}{2\sigma^2}\right) \right) \cdot \left(\frac{1}{\sqrt{2\pi}\sigma} \exp\left(-\frac{y^2}{2\sigma^2}\right) \right), \quad (5.2)$$

where σ is variance. We can operate Gaussian filter both in spatial and frequency domains as follows.

- Convolution in spatial domain

Convolution provides a way of ‘multiplying together’ two arrays of numbers, generally of different sizes, but of the same dimensionality, to produce a third array of numbers of the same dimensionality. The convolution is performed by sliding the kernel over the image, generally starting at the top left corner, so as to move the kernel through all the positions where the kernel fits entirely within the boundaries of the image. Each kernel position corresponds to a single output pixel, the value of which is calculated by multiplying together the kernel value and the underlying image pixel value for each of the cells in the kernel, and then adding all these numbers together.

- Multiplication in frequency domain

Based on eq. 5.1 it appears possible to achieve the result as following

i) compute $A(u, v) = F \{a(x, y)\}$

ii) multiply $A(u, v)$ by the precomputed $H(u, v) = F \{h(x, y)\}$

iii) compute the result $b(x, y) = F^{-1} \{A(u, v)H(u, v)\}$,

where $F \{ \}$ is Fourier transform operator.

Gaussian filtering

The following procedure uses the image shown in figure 5.6. In order to perform FFT (Fast Fourier Transform) instead of the much slower DFT (Discrete Fourier Transfer) the image must be transformed so that the width and height are an integer power of 2. This can be achieved in one of two ways; scaling the image up to the nearest integer power of 2 or zero padding to the nearest integer power of 2. The second option was chosen here to facilitate comparisons with the original. The resulting image is 256 x 256 pixels, shown in figure 5.10.

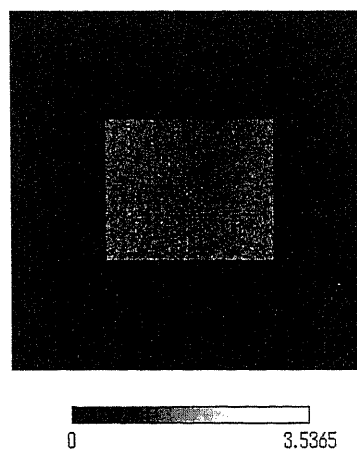


Figure 5.10: Division image with zero padding.

The following briefly describes how to perform spatial Fourier transform. The most common application is for image processing where each value in the array represents to a pixel, therefore the real value is the pixel value and the imaginary value is 0. Two dimensional Fourier transforms simply involve a number of 1 dimensional Fourier transforms. More precisely, a 2 dimensional transform is achieved by first transforming

each row, replacing each row with its transform and then transforming each column, replacing each column with its transform. The default organization of the quadrants from FFT (spatial frequency domain) routines is as figure 5.11. Here T is the pixel size in spatial domain, M and N are the number of pixels in horizontal and

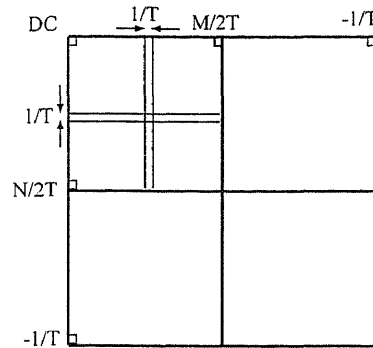


Figure 5.11: The default organization of the quadrants from FFT.

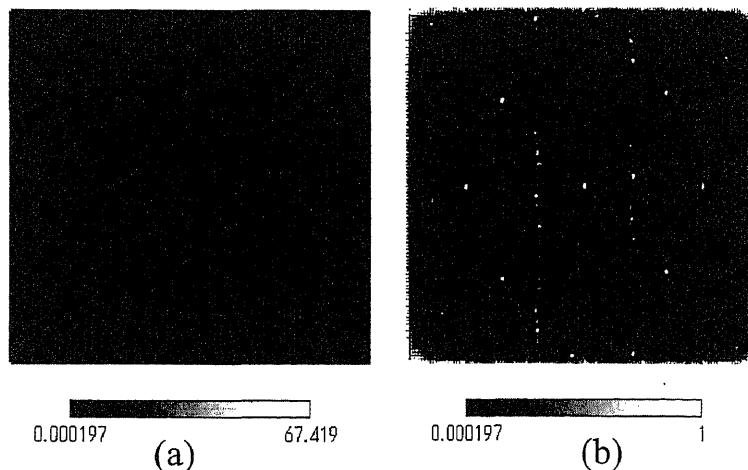


Figure 5.12: Fourier transformed image of figure 5.10 in default organization (a) all values, $A[u, v]$ (b) the maximum value of the image is set to be 1.

vertical directions. The dc (frequency = 0) is in the corners of the image. The magnitude of the 2 dimension FFT of figure 5.10 is displayed in figure 5.12(a). We can see that the dc-value is by far the largest component of the image. However, the dynamic range of the Fourier coefficients, i.e., the intensity values in the Fourier image, is too large compared with the minimum value, see color bar below the picture, therefore all other values appear as black. If we set the maximum value to be 1, we obtain figure 5.12(b). Figure 5.13 has had the quadrants reorganized so as to place dc in the center of the image.

Given a Gaussian filter $h[x, y]$ of dimension $M \times N$ in spatial domain, we will consider the coordinate $[x = 0, y = 0]$ to be in the center of the filter matrix, h . The center is well-defined when M and N are odd; for the case where they are even, we use the approximation $[M/2 + 1, N/2 + 1]$ for the center of the matrix. The Gaussian kernel which has variance 1 is transformed and its magnitude in frequency domain is shown in figure 5.14. Next steps is multiplying the element of $A(u, v)$ and $H(u, v)$ pixel by pixel, not matrix multiplication production, and re-transforming to spatial domain. The final image is illustrated in figure 5.15(a). However the real image should be re-arranged and cut to same size with beginning image, or 120×100 pixels, as in figure 5.15(b). The low values at three edges of the image are probably the effect of sliding center of the Gaussian filter. Larger value of variance in filtering makes the image smoother. The filtered image shows

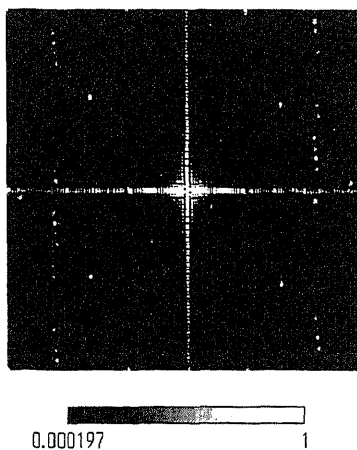


Figure 5.13: Reorganized quadrants of the Fourier transformed image of figure 5.12(b).

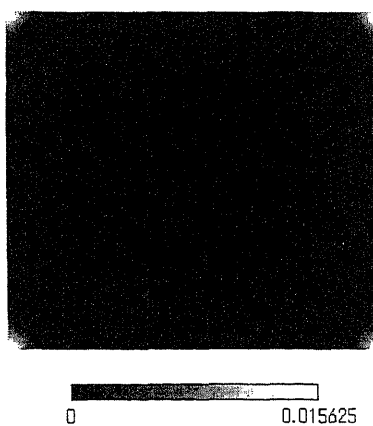


Figure 5.14: Magnitude of Gaussian filter, $H[u, v]$.

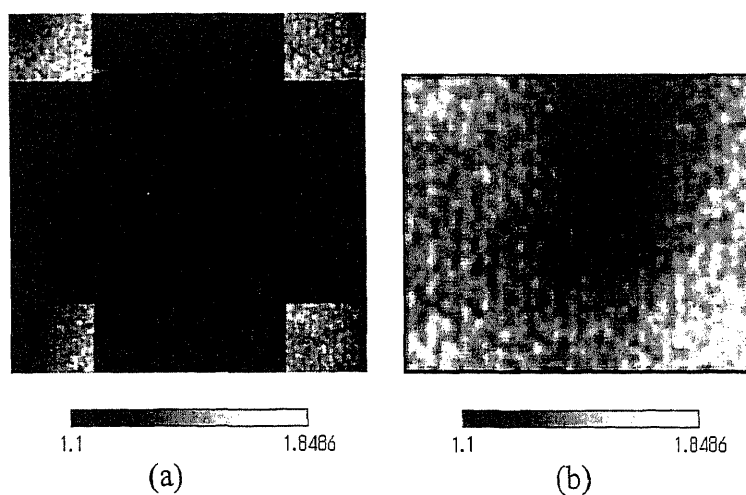


Figure 5.15: (a) Re-transformed image, (b) filtered image. The image (b) is resized, it is therefore larger than its compositions in the image(a).

improved contrast at the object region.

5.5 Conclusions

1-kHz THz field imaging was performed using a single optical pulse for probing. This study has expanded the vision of monitoring single-time events in THz frequency regime. A metal object that THz waves can not pass through was chosen to simulate a single-time event by vibrating on the object plane of the TPX lens. This experiment leads to the possibility in observing a moving object concealed in a THz-transparent container such as a paper or plastic box. Another possibility to apply the non-destructive imaging system is to see the movement of biological materials. Some experiments of biology need to observe a plant in dark condition. If the plant is covered by a THz-transparent material, THz waves can identify orientation and movement inside based on the fact that the interesting object absorbs THz waves.

Because the probe light is a single pulse, it is weak modulated by a THz pulse. Therefore, the signal is comparative to a noise level from the CCD camera and instability of the laser system, the image quality has to be enhanced. Firstly, the THz image was divided with the reference image to distinguish sample information from THz beam profile. Then, a Gaussian filter was applied to eliminate the noises. As a result, observation of high-speed events with THz radiation is realized at a temporal resolution of 1 ms for the first time.

Chapter 6

Conclusions

This thesis has discussed the potential performance of utilizing intense half-cycle THz radiation applied to two-dimensional imaging. The THz radiation was generated from a large-aperture biased photoconductive antenna. The main advantage of this source is that it provides high-power THz radiation. The propagation characteristics of the THz pulse were described in chapter 2. The temporal waveform at a given position can be numerically simulated by considering the Gaussian beam profile of each frequency component. Chapter 2 also mentions why the intensity distribution of the focused beam expresses an annular profile at a certain region of space and time. Therefore, the basic knowledge about half-cycle THz pulses that had been used for the imaging was well understood. Knife-edge experiment, a well known method for measuring an optical beam size, was applied to observe the frequency dependence of THz beam profile in front of the emitter. The beam size of the waves having frequency higher than 1 THz is comparative to a $1/e$ diameter of the optical pump beam, i.e., about 19 mm. Absorption coefficient of TPX was measured using time-domain spectroscopy in a frequency range of 0-2 THz.

The measurements of THz electric field at the center of focused THz beam and on the plane that is perpendicular to the propagation axis were described in chapter 3. They are based on electro-optic sampling technique. The change of polarization of probe light which modulated by the THz electric field and by optical components was described in detail. Using the technique, two-dimensional THz field images of an object have been detected by a CCD camera, mentioned in chapter 4. The unique time-dependent field distribution of the focused THz beam leads to the shape of the sample object depending on the time delay and limits the period of imaging of an object. We can find the optimal time for imaging with good image quality. This shows that the problem of time-dependent image shapes has been solved. Furthermore, Fourier transformation of the time-dependent image series permits frequency-resolved images. Image contrast in the frequency domain is better than that in the time domain. Interestingly, some frequency components represent the edge of the object. Since the THz pulse is composed of broadband frequencies and the peak frequency locates near DC, the spatial resolution is low as about 1 mm. Using the fact that the higher peak frequency the higher resolution is, 500- μm LT-GaAs substrate on a GaAs wafer was employed as a photoconductive conductor. Theoretically, it enhances the electric field at high frequency components because the carrier lifetime is shorter than the GaAs wafer about 100 times. However the LT-GaAs was not thick enough, the pump light penetrated to the GaAs layer and generated number of normal-lifetime electrons. As a result, the spectrum from the new emitter is not significantly different from the former one. Another attempt to improve the resolution is using metallic hole arrays. The frequency that is below the cutoff frequency of the hole attenuated but there is a highest transmission frequency. This is caused from the fact that the arrays behave as a grating. Therefore, metallic hole arrays can be used as band-pass filter.

Using to the optimized timing, dynamic processes or a moving object can be imaged at the fixed time delay as described in chapter 5. Single-shot THz imaging was achieved with intense THz pulses from a large-

aperture photoconductive antenna, the sensitive detection technique and a fast-speed CCD camera. It allows observing ultrafast dynamic processes occurring in a probe pulse width, namely on the order of femtosecond or picosecond. Image processing, i.e. Gaussian filtering, was applied to a single-shot THz image for the elimination of noises and edge enhancement. Computer codes in C that can manipulate the entire set of images at one time are added in appendix. Image THz movies of an object were first performed at a frame rate as high as 1000 frames per second. This opens the door of ultrafast imaging in THz regime. The future research should pay attention to improving the spatial resolution.

The perspective stepping toward the real-world application of this research is as follows.

1. The high-speed THz imaging allows observing ultrafast and single-time events that opaque in at other spectrum regions.
2. The high-power THz source requires a regenerative amplifier for the optical seed and high-bias voltage generator. The imaging system might be applied for the security checks if the size of the equipments can be reduced.
3. The imaging system will be more practically used if it can detect an object having the same size as a credit card.
4. More work needs to be done to improve the spatial resolution such as by reducing the power of low-frequency components and expanding the THz beam size.

Appendix A

Gaussian filtering

```
#include <stdio.h>
#include <math.h>
#include <string.h>
#include <stdlib.h>
#include <except.h>
#include <iostream.h>

#define PI 4.* atan (1.)
#define Nwidth 120 // original horizontal dimension
#define Nheight 100 // original vertical dimension
#define Fnumber 256 // dimension before transforming

double data[Nheight][Nwidth];
double re_r[Fnumber][Fnumber],im_r[Fnumber][Fnumber];

main(){
    double FFT2D(double **, double **,int, int , int);
    double gauss(double, double);

    int i, j, k, ud,lr, n_temp;

    char dir1[150],newdir1[150],file1[150],file2[150];
    char c;

    double temp, temp1,sigma,x,y;
    double **re,**im,***re_r,**im_r,*/ **ft_re,**ft_im;

    FILE *fp1, *fp2;

    // Input folder
    strcpy(dir1,"C:\\work\\thzdata\\Temp\\031106\\kumimove_divide_new\\");
    // Output folder
    strcpy(newdir1,"C:\\work\\thzdata\\Temp\\031106\\kuki_IP\\");

    ud=(Fnumber-Nheight)/2;
    lr=(Fnumber-Nwidth)/2;
    n_temp=Fnumber/2;
    temp1=Fnumber*1.0;

    re= new double*[Fnumber];
    im= new double*[Fnumber];
    ft_re= new double*[Fnumber];
    ft_im= new double*[Fnumber];
    for (i = 0; i < Fnumber; i++){
```

```

    re[i] = new double[Fnumber];
    im[i] = new double[Fnumber];
    ft_re[i] = new double[Fnumber];
    ft_im[i] = new double[Fnumber];
}
// Make Gaussian filter and transform it
sigma=1.0;
for(i=0; i<Fnumber; i++){
    for(j=0 ;j<Fnumber; j++){
x=i-(Fnumber/2.0);
        y=j-(Fnumber/2.0);

        ft_re[i][j]= gauss(x,sigma)*gauss(y,sigma);
        ft_im[i][j]=0.0;
}
}

FFT2D(ft_re, ft_im, Fnumber, Fnumber, 1);
for(i=0; i<Fnumber; i++){
    for(j=0 ;j<Fnumber; j++){
        ft_re[i][j]=ft_re[i][j]/temp1 ;
        ft_im[i][j]=ft_im[i][j]/temp1 ;
}
}
// Load data
for(k=1; k<1000; k++){
    sprintf(file1,"%skukidv%04d.txt",dir1,k);
    if ((fp1=fopen(file1,"r")) == NULL){
        printf("Cannot open file: %s\n",file1);
        c=getchar();
        exit(1);
    }
    for(i=0; i<Nheight; i++){
    for(j=0 ; j<Nwidth; j++){
        fscanf(fp1,"%lf," , &temp);
        data[i][j]=temp;
    }
}
fclose (fp1);

//extend pixels from 120x100 to 256x256
for(i=0; i<ud; i++){
    for(j=0 ; j<Fnumber; j++){
        re[i][j]=0.0;
        im[i][j]=0.0;
    }
}
// Top

for(i=ud; i<ud+Nheight; i++){
    for(j=0 ; j<Fnumber; j++){
        if (j<lr||j>(lr+Nwidth)){
            re[i][j]=0.0;
            im[i][j]=0.0;
        }
        else{
            re[i][j]=data[i-ud][j-lr];
            im[i][j]=0.0;
        }
    }
}
}
}

```

```

        for(i=ud+Nheight; i<Fnumber; i++){           // below
        for(j=0 ; j<Fnumber; j++){
            re[i][j]=0.0;
            im[i][j]=0.0;
        }
    }

// Forward Fourier transform

    FFT2D(re, im, Fnumber, Fnumber, 1);

// Multiply with Gaussian function

for(i=0; i<Fnumber; i++){
    for(j=0 ;j<Fnumber; j++){
        re[i][j]=ft_re[i][j]*re[i][j]-ft_im[i][j]*im[i][j];
        im[i][j]=ft_im[i][j]*re[i][j]+ft_re[i][j]*im[i][j];
    }
}

//Backward Fourier Transform
    FFT2D(re, im, Fnumber, Fnumber, -1);

// Arrange data

    for(i=0; i<n_temp; i++){
    for(j=0 ;j<n_temp; j++){
        re_r[i][j]=re[i+n_temp][j+n_temp];
        im_r[i][j]=im[i+n_temp][j+n_temp];

        re_r[i][j+n_temp]=re[i+n_temp][j];
        im_r[i][j+n_temp]=im[i+n_temp][j];

        re_r[i+n_temp][j]=re[i][j+n_temp];
        im_r[i+n_temp][j]=im[i][j+n_temp];

        re_r[i+n_temp][j+n_temp]=re[i][j];
        im_r[i+n_temp][j+n_temp]=im[i][j];
    }
}

//Cut extended parts and write into a file
    for(i=ud; i<=ud+Nheight; i++){
    for(j=lr ;j<=lr+Nwidth; j++){
        data[i-ud][j-lr]=re_r[i][j]/temp1;
    }
}
    sprintf(file2,"%srmf_\\%04d.txt",newdir1,k);

    if ((fp2=fopen(file2,"wt")) == NULL){
        printf("Cannot open file: %s\n",file2);
        c=getchar();
        exit(1);
    }

for(i=0; i<Nheight; i++){
    for(j=0 ;j<Nwidth; j++){
        fprintf(fp2,"%lf",data[i][j]);
    if(j!=Nwidth-1) fprintf(fp2,",");
        else fprintf(fp2,"\n");
    }
}
}

```

```

        fclose(fp2);
        printf("\%d ",k);
    }

return 0;
}
/*-----
Perform a 2D FFT inplace given a complex 2D array
The direction dir, 1 for forward, -1 for reverse
The size of the array (nx,ny)
*/
double FFT2D(double **re,double **im, int nx,int ny,int dir)
{
double FFT(double *, double *, int , int );
int i,j;
double *real,*imag;

/* Transform the rows */
real= new double[nx];
imag= new double[nx];
if (real == NULL || imag == NULL){
    printf("\n There is memory problem");
    exit(1);
}
for (i=0;i<ny;i++) {
    for (j=0;j<nx;j++) {
        real[j] = re[i][j];
        imag[j] = im[i][j];
    }
    FFT(real,imag,nx,dir);
    for (j=0;j<nx;j++) {
        re[i][j] = real[j];
        im[i][j] = imag[j];
    }
}
delete[] real;
delete[] imag;

/* Transform the columns */
real= new double[ny];
imag= new double[ny];
if (real == NULL || imag == NULL){
    printf("\n There is memory problem");
    exit(1);
}
for (j=0;j<nx;j++) {
    for (i=0;i<ny;i++) {
        real[i] = re[i][j];
        imag[i] = im[i][j];
    }
    FFT(real,imag,ny,dir);
    for (i=0;i<ny;i++) {
        re[i][j] = real[i];
        im[i][j] = imag[i];
    }
}
delete[] real;
delete[] imag;

return 0;
}

```

```

double FFT(double *dr, double *di, int NN, int sign){
  int i, j, m, mmax, step;
  double wr, wi, wpr, wpi, wtemp, theta, tempr, tempi, sn;
  j = 0;
  for(i=0;i<NN;i++){
    if(j>i){
      tempr = dr[j];
      tempi = di[j];
      dr[j] = dr[i];
      di[j] = di[i];
      dr[i] = tempr;
      di[i] = tempi;
    }
    m=NN/2;
    while((m>=1)&&(j>=m)){
      j -= m;
      m /= 2;
    }
    j += m;
  }
  mmax=1;
  while(NN>mmax){
    step=2*mmax;
    theta=PI/(sign*mmax);
    sn=sin(0.5*theta);
    wpr=-2*sn*sn;
    wpi=sin(theta);
    wr=1;
    wi=0;
    for(m=0;m<mmax;m++){
      for(i=m;i<NN;i+=step){
        j=i+mmax;
        tempr=wr*dr[j]-wi*di[j];
        tempi=wr*di[j]+wi*dr[j];
        dr[j]=dr[i]-tempr;
        di[j]=di[i]-tempi;
        dr[i]=dr[i]+tempr;
        di[i]=di[i]+tempi;
      }
      wtemp=wr;
      wr=wr*wpr-wi*wpi+wr;
      wi=wi*wpr+wtemp*wpi+wi;
    }
    mmax=step;
  }
  return 0;
}

double gauss(double x,double sig){
  double y;

  y= exp(-x*x/(2.0*sig*sig))/ (sig*sqrt(2*PI));

  return(y);
}

void de_allocate2f(double **data,int ny) { // delete pointer

  for (int i = 0; i < ny; i++)
    delete[] data[i]; // STEP 1: DELETE THE COLUMNS

  delete[] data; // STEP 2: DELETE THE ROWS
}

```

Bibliography

- [1] D. Grischkowsky, S. Keiding, M. van Exter, and CH. Fattinger. Far-infrared time-domain spectroscopy with terahertz beams of dielectrics and semiconductors. *J. Opt. Soc. Am. B*, Vol. 7, pp. 2006–2015, 1990.
- [2] M. Walther, B. Fischer, M. Schall, H. Helm, and P. Uhd Jepson. Far-infrared vibrational spectra of all 9-*cis* and 13-*cis* retinal measured by thz time-domain spectroscopy. *Chem. Phys. Lett.*, Vol. 332, pp. 389–395, 2000.
- [3] K. Okumura and Y. Tanimura. Two-dimensional thz spectroscopy of liquids: non-linear vibrational response to a series of thz pulses. *Chem. Phys. Lett.*, Vol. 295, pp. 298–304, 1998.
- [4] E. Pickwell, B. E. Cole, A. J. Fitzgerald, M. Pepper, and V. P. Wallace. In vivo study of human skin using pulsed terahertz radiation. *Phys. Med. Biol.*, Vol. 49, pp. 1595–1607, 2004.
- [5] Q. Wu, T. D. Hewitt, and X.-C. Zhang. Two-dimensional electro-optic imaging of thz beams. *Appl. Phys. Lett.*, Vol. 69, pp. 1026–1028, 1996.
- [6] P. Sang-Gyu, A. M. Weiner, M. R. Melloch, C. W. Sider, J. L. Sider, and A. J. Taylor. High-power narrow-band terahertz generation using large-aperture photoconductors. *IEEE J. Quantum Electron.*, Vol. 35, pp. 1257–1268, 1999.
- [7] H. Yaneda, K. Tokuyama, K. Ueda, H. Yamamoto, and K. Baba. High-power terahertz radiation emitter with a diamond photoconductive switch array. *Appl. Opt.*, Vol. 40, pp. 6733–6736, 2001.
- [8] K. Reimann, R. P. Smith, A. M. Weiner, T. Elsaesser, and M. Woerner. Direct field-resolved detection of terahertz transients with amplitudes of megavolts per centimeter. *Opt. Lett.*, Vol. 28, pp. 471–473, 2003.
- [9] G. L. Carr, M. C. Martin, W. R. McKinney, K. Jordan, G. R. Nell, and G. P. Williams. High-power terahertz radiation from relativistic electrons. *Nature*, Vol. 420, pp. 153–156, 2002.
- [10] C. Raman, C. W. S. Conover, C. I. Sukenik, and P. H. Bucksbaum. Ionization of rydberg wave packets by subpicosecond, half-cycle electromagnetic pulses. *Phys. Rev. Lett.*, Vol. 76, pp. 2436–2439, 1996.
- [11] G. Ramian. The new ucsb free-electron lasers. *Nucl. Instrum. Methods Phys. Res. A*, Vol. 318, pp. 225–229, 1992.
- [12] D. W. Porterfield, T. W. Crowe, R. F. Bradley, and N. R. Erickson. A high-power, fixed-tuned, millimeter-wave balanced frequency doubler. *IEEE Trans. Microwave Theory Techn.*, Vol. MTT-47, pp. 419–425, 1999.
- [13] Kodo Kawase, J. Shikata, and H. Ito. Terahertz wave parametric source. *J. Phys. D: Appl. Phys.*, Vol. 35, pp. R1–R14, 2002.
- [14] A. Gürtler, C. Winnewisser, H. Helm H, and P. U. Jopsen. Terahertz pulse propagation in the near field and the far field. *J. Opt. Soc. Am. A*, Vol. 17, pp. 74–83, 2000.

- [15] C. Rulliere. *Femtosecond laser pulses: Principles and experiments*. Springer, 1998. p 286.
- [16] D. H. Auston. Picosecond optoelectronic switching and gating in silicon. *Appl. Phys. Lett.*, Vol. 26, pp. 101–103, 1975.
- [17] C. Fattinger and D. Grischokowsky. Point source terahertz optics. *Appl. Phys. Lett.*, Vol. 53, pp. 1480–1482, 1988.
- [18] D. You, R. R. Jones, P. H. Bucksbaum, and D. R. Dykaar. Generation of high-power sub-single-cycle 500-fs electromagnetic pulses. *Opt. Lett.*, pp. 290–292, 1993.
- [19] Q. Wu and X.-C. Zhang. Free-space electro-optic sampling of terahertz beams. *Appl. Phys. Lett.*, Vol. 67, pp. 3523–3525, 1995.
- [20] J. T. Darrow, X.-C. Zhang, D. H. Auston, and J. D. Morse. Saturation properties of large-aperture photoconducting antennas. *IEEE J. Quantum Electron.*, Vol. 28, pp. 1619–1622, 1992.
- [21] T. Hattori, K. Tukumoto, and H. Nakatsuka. Time-resolved study of intense terahertz pulses generated by a large-aperture photoconductive antenna. *Jpn. J. Appl. Phys.*, Vol. 40, pp. 4907–4912, 2001.
- [22] X.-C. Zhang, B. B. Hu, J. T. Darrow, and D. H. Auston. Generation of femtosecond electromagnetic pulses from semiconductor surfaces. *Appl. Phys. Lett.*, Vol. 56, pp. 1011–1013, 1990.
- [23] X.-C. Zhang and D. H. Auston. Optoelectronic measurement of semiconductor surfaces and interfaces with femtosecond optics. *J. Appl. Phys.*, Vol. 69, pp. 326–338, 1992.
- [24] S. L. Chuang, S. Schmitt-Rink, B. I. Greene, P. N. Saeta, and A. F. J. Levi. Optical rectification at semiconductor surfaces. *Phys. Rev. Lett.*, Vol. 68, pp. 102–105, 1992.
- [25] X.-C. Zhang, Y. Jin, K. Yang, and L. J. Schowalter. Resonant nonlinear susceptibility near the gas band gap. *Phys. Rev. Lett.*, Vol. 69, pp. 2303–2306, 1992.
- [26] X.-C. Zhang, Y. Jin, and X. F. Ma. Coherent measurement of thz optical rectification from electro-optic crystals. *Appl. Phys. Lett.*, Vol. 61, pp. 2764–2766, 1992.
- [27] X.-C. Zhang, Y. Jin, T. D. Hewitt, and T. Sangsiri. Magnetic switching of THz beam. *Appl. Phys. Lett.*, Vol. 62, pp. 2003–2005, 1993.
- [28] N. Sarukura, H. Ohtake, S. Izumida, and Z. Liu. High average-power thz radiation from femtosecond laser-irradiated inas in a magnetic field and its elliptical polarization characteristics. *J. Appl. Phys.*, Vol. 84, pp. 654–656, 1998.
- [29] H. Ohtake, S. Ono, M. Sakai, Z. Liu, T. Tsukamoto, and N. Sarakura. Saturation of thz-radiation power from femtosecond-laser-irradiated inas in a high magnetic field. *Appl. Phys. Lett.*, Vol. 76, pp. 1398–1400, 2000.
- [30] T. Feurer, J. C. Vauhan, T. Hornung, and K. Nelson. Typesetting of terahertz waveforms. *Opt. Lett.*, Vol. 29, pp. 1802–1804, 2004.
- [31] A. Rice, Y. Jin, X. F. Ma, X.-C. Zhang, D. Bliss, J. Larkin, and M. Alexander. Terahertz optical rectification from zinc-blende crystals. *Appl. Phys. Lett.*, Vol. 64, pp. 1324–1326, 1994.
- [32] X.-C. Zhang, X. F. Ma, Y. Jin, T.-M. Lu, E. P. Boden, P. D. Phelps, K. R. Stewart, and C. P. Yakymyshyn. Terahertz optical rectification from a nonlinear organic crystal. *Appl. Phys. Lett.*, Vol. 61, pp. 3080–3082, 1992.

- [33] R. A. Kaindl, D. C. Smith, M. Joschko, M. P. Hasselbeck, M. Woerner, and T. Elsaesser. Femtosecond infrared pulses tunable from 9-18 μm at an 88-mhz repetition rate. *Opt. Lett.*, Vol. 23, pp. 861–863, 1998.
- [34] M. Usami, T. Iwamoto, R. Fukusawa, M. Tani, M. Watanabe, and K. Sakai. Development of a thz spectroscopic imaging system. *Phys. Med. Biol.*, pp. 3749–3753, 2002.
- [35] Amnon Yariv. *Quantum electronics, 3rd ed.* John Wiley and Sons, 1988. p 118.
- [36] T. Hattori, R. Rungsawang, K. Ohta, and K. Tukamoto. Gaussian beam analysis of temporal waveform of focused terahertz pulse. *Jpn. J. Appl. Phys.*, Vol. 41, pp. 5198–5204, 2002.
- [37] B. B. Hu and M. C. Nuss. Imaging with terahertz waves. *Opt. Lett.*, Vol. 20, pp. 1716–1719, 1995.
- [38] Z. Jiang, F. G. Sun, Q. Chen, and X.-C. Zhang. Electro-optic sampling near zero optical transmission point. *Appl. Phys. Lett.*, Vol. 74, pp. 1191–1193, 1999.
- [39] P. F. Goldsmith. *Quasioptical systems : Gaussian beam quasioptical propagation and applications.* IEEE Press: New York, 1998. p 26.
- [40] R. Rungsawang. Studies of temporal and spatial shape of terahertz pulses generated from a large-aperture photoconductive antenna. Master's thesis, University of Tsukuba, Tsukuba, Ibaraki 305-8573 Japan, March 2002.
- [41] K. Tukamoto, R. Rungsawang, T. Hattori, and H. Nakatsuka. Propagation and focusing characteristics of intense terahertz pulses generated from a large aperture photoconductive antenna. *Technical digest of CLEO/Pacific Rim 2001*, Vol. II, pp. 738–739, 2001.
- [42] G. J. Simonis. Characterization of near-millimeter wave materials by means of non dispersive fourier transform spectroscopy. *Int. J. Infrared and Millimeter Waves*, Vol. 5, pp. 57–73, 1984.
- [43] J. A. Clarke and R. J. Dewey. Millimeter wave imaging lens antenna. *Int. J. Infrared and Millimeter Waves*, Vol. 5, , 1984.
- [44] Born M. and Wolf E. Principles of optics. 7th edition, Cambridge university press, 1999.
- [45] R.W. Barber and S.C. Hill. Light scattering by particles: Computational methods. World Scientific, Singapore, 1990.
- [46] *Melles Griot catalog: The practical application of light.* 1999.
- [47] S. Wang, T. Yuan, E.D. Walsby, R. J. Blaikie, S. M. Durbin, D. R. S. Cumming, J. Xu, and X.-C. Zhang. Characterization of t-ray binary lenses. *Opt. Lett.*, Vol. 27, pp. 1183–1185, 2002.
- [48] A. Leitensdorfer, S. Hunsche, J. Shah, M. C. Nuss, and W. H. Knox. Femtosecond charge transport in polar semiconductors. *Phys. Rev. Lett.*, Vol. 82, pp. 5140–5143, 1999.
- [49] C. Winnewisser, P. Uhd Jepsen, M. Schall, V. Schyja, and H. Helm. Electro-optic detection of thz radiation in LiTaO_3 , LiNbO_3 and ZnTe . *Appl. Phys. Lett.*, Vol. 70, pp. 3069–3071, 1997.
- [50] G. L. Easley, M. D. Levenson, and W. M. Tolles. Optical heterodyned coherent raman spectroscopy. *IEEE J. of Quantum Electron*, Vol. 14, pp. 45–49, 1978.
- [51] M. D. Levenson and G. L. Easley. Polarization selective optical heterodyne detection for dramatically improved sensitivity in laser spectroscopy. *Appl. Phys.*, Vol. 19, pp. 1–17, 1979.

- [52] T. Hattori, K. Ohta, R. Rungsawang, and K. Tukamoto. Phase-sensitive high-speed thz imaging. *J. Phys. D: Appl. Phys.*, Vol. 37, pp. 1–4, 2004.
- [53] F. Miyamaru, T. Yonera, M. Tani, and M. Hangyo. Terahertz two-dimensional electrooptic sampling using high speed complementary metal-oxide semiconductor camera. *Jpn. J. of Appl. Phys.*, Vol. 43, pp. L489–L491, 2004.
- [54] R. Rungsawang, K. Ohta, K. Tukamoto, and T. Hattori. Ring formation of focused half-cycle terahertz pulses. *J. Phys. D: Appl. Phys.*, Vol. 36, pp. 229–235, 2003.
- [55] M. T. Reiten, S. A. Harmon, and R. A. Cheville. Terahertz beam propagation measured through three-dimensional amplitude profile determination. *J. Opt. Soc. Am. B*, Vol. 20, pp. 2215–2225, 2003.
- [56] H. Nemeč, A. Pashkin, P. Kuzel, M. Khazan, and S. Schnull and. Carrier dynamics in low-temperature grown gas studied by thz emission spectroscopy. *J. Appl. Phys.*, Vol. 90, pp. 1303–1317, 2001.
- [57] D. Liu and J. Qin. Carrier dynamics from low-temperature-grown gas. *Appl. Opt.*, Vol. 42, pp. 3678–3683, 2003.
- [58] M. C. Beard, G. M. Turner, and C. C. Schmuttenmaer. Subpicosecond carrier dynamics in low-temperature grown gas as measured by time-resolved terahertz spectroscopy. *J. Appl. Phys.*, Vol. 90, pp. 5915–5923, 2001.
- [59] E. S. Harmon, M. R. Melloch, J. M. Woodall, D. D. Nolte, N. Otsuka, and C. L. Chang. Carrier lifetime versus anneal in low temperature growth gas. *Appl. Phys. Lett.*, Vol. 63, pp. 2248–2250, 2003.
- [60] E. D. Palik. *Handbook of Optical Constants of Solids*. Academic Press, 1997.
- [61] D. E. Aspnes and A. A. Studna. Dielectric functions and optical parameters of si, ge, gap, gas, gasb, inp, inas, and insb from 1.5 to 6.0 eV. *Phys. Rev. B*, Vol. 27, pp. 985–1009, 1982.
- [62] S. M. Sze. *Physics of semiconductor devices*. New York Wiley, 2nd edition, 1981.
- [63] T. Hattori, R. Rungsawang, K. Ohta, and K. Tukamoto. Propagation of focused terahertz pulses through subcentimeter-size conductive apertures. *Jpn. J. Appl. Phys.*, Vol. 42, pp. 1609–1613, 2002.
- [64] T. Timusk and P. L. Richards. Near millimeter wave bandpass filters. *Appl. Opt.*, Vol. 20, pp. 1355–1360, 1981.
- [65] C. Winnewisser, F. Lewen, J. Weinzierl, and H. Helm. Transmission features of frequency-selective components in the far infrared determined by terahertz time-domain spectroscopy. *IEEE Trans. Microwave theory Tech.*, Vol. 48, pp. 744–749, 2000.
- [66] C. Winnewisser, F. Lewen, M. Schall, M. Walther, and H. Helm. Characterization and application of dichroic filters in the 0.1–3-thz region. *Appl. Opt.*, Vol. 38, pp. 3961–3967, 1999.
- [67] C.-C. Chen. Transmission of microwave through perforated flat plates of finite thickness. *IEEE trans. Microwave Theory Tech.*, Vol. 21, pp. 1–6, 1973.
- [68] J. W. Archer. A novel quasi-optical frequency multiplier design for millimeter and submillimeter wavelengths. *IEEE trans. Microwave Theory Tech.*, Vol. 32, pp. 421–427, 1984.
- [69] C. Winnewisser, F. Lewen, and H. Helm. Transmission characteristics of dichroic filters measured by thz time-domain spectroscopy. *Appl. Phys. A*, Vol. 66, pp. 593–598, 1998.

- [70] Z. Jiang and Xi-Cheng Zhang. 2D measurement and spatio-temporal coupling of few-cycle thz pulses. *Opt. Express*, Vol. 5, pp. 243–248, 1999.
- [71] R. Rungsawang, K. Tukamoto, and T. Hattori, 2004.
- [72] A. K. Jain. Fundamental of digital image processing. APrentice-Hall, 1989.
- [73] T. I. Young. Fundamental of image processing. The Netherlands at the Delft University of Technology, 1998.

ACKNOWLEDGEMENTS

The author would like to express her sincere gratitude to Associate Professor Toshiaki Hattori of the University of Tsukuba for his constant guidance, tolerant discussions and encouragement throughout this work. The author also wishes to greatly thank to Professor Hiroki Nakatsuka of the same University for kindness receiving the author to study in Japan and being her supervisor for the first year. The author is also grateful to her excellent colleagues, especially Mr. Keiji Tukumoto, Mr. Keitsuke Ohta, Miss Aya Mochiduki, and all members of Nakatsuka-Hattori laboratory and Hattori laboratory for their help in experiments and useful discussions. The author wishes to thank Mr. Marco Amati for correcting English in the thesis and publications. Finally, the author wishes to thank her parents, family and all her friends whose help and mental support have made the study possible and fruitful.

This work was financial supported by Ministry of Education, Culture, Sports, Science and Technology, Japan and the 21st Century Center of Excellence Program “Promotion of Creative Interdisciplinary Materials Science for Novel Functions”.